DOKUZ EYLÜL UNIVERSITY
GRADUATE SCHOOL OF NATURAL AND APPLIED SCIENCES

DETERMINATION OF HEAT TRANSFER AND FLOW CHARACTERISTICS OF SPLIT AIR CONDITIONERS BY INFRARED THERMOGRAPHY AND PARTICLE IMAGE VELOCIMETRY

by
Ziya Haktan KARADENİZ

October, 2011
İZMİR

DETERMINATION OF HEAT TRANSFER AND FLOW CHARACTERISTICS OF SPLIT AIR CONDITIONERS BY INFRARED THERMOGRAPHY AND PARTICLE IMAGE VELOCIMETRY

A Thesis Submitted to the
Graduate School of Natural and Applied Sciences of Dokuz Eylül University
In Partial Fulfillment of the Requirements for the Degree of Doctor of Philosophy in Mechanical Engineering, Energy Program

by
Ziya Haktan KARADENİZ

October, 2011
İZMİR

Ph.D. THESIS EXAMINATION RESULT FORM

We have read the thesis entitled **"DETERMINATION OF HEAT TRANSFER AND FLOW CHARACTERISTICS OF SPLIT AIR CONDITIONERS BY INFRARED THERMOGRAPHY AND PARTICLE IMAGE VELOCIMETRY"** completed by **ZİYA HAKTAN KARADENİZ** under supervision of **ASSOC. PROF. DR. DİLEK KUMLUTAŞ** and we certify that in our opinion it is fully adequate, in scope and in quality, as a thesis for the degree of Doctor of Philosophy.

Assoc. Prof. Dr. DİLEK KUMLUTAŞ

Supervisor

Prof. Dr. İsmail Hakkı TAVMAN	Prof. Dr. Yalçın ÇEBİ
Thesis Committee Member	Thesis Committee Member
Prof. Dr. Haşmet TÜRKOĞLU	Asst. Prof. Dr. Alpaslan TURGUT
Examining Committee Member	Examining Committee Member

Prof. Dr. Mustafa SABUNCU

Director

Graduate School of Natural and Applied Sciences

ACKNOWLEDGMENTS

First of all, I would like to express my sincere gratitude to my supervisor, Assoc. Prof. Dr. Dilek Kumlutaş, for her guidance, attention and support all through my graduate education and for being a milestone in my academic progress. Also I would like to thank to Prof. Dr. İsmail Hakkı Tavman and Prof. Dr. Yalçın Çebi for their valuable contributions at the periodical meetings of this research.

I would like to thank to the graduate students in the lab, especially Özgün Özer for his valuable knowledge about optics and imaging, and for his help about performing measurements, data acquisition and processing, and others Funda Kuru, Hasan Avcı, and Mete Özşen for their support. Also, I would like to express my sincere thanks to my colleagues, Dr. Alpaslan Turgut, Dr. Mehmet Akif Ezan, Dr. Levent Çetin, and Dr. Özgün Başer who broaden my view and knowledge of life and encouraged me in every stage of my academic research, and Alim Zorluol for his assistance.

Without the care, understanding, support and compassion of my mother, father and brother all through my life I would not be in a situation of writing a PhD thesis.

My heartiest thanks to my dearests; my son and my wife… Their presence is incomparable with any other thing in the world. Also, my special thanks to my wife for her understanding, consideration, and support.

I also would like to thank to the Graduate School of Natural and Applied Sciences and Department of Mechanical Engineering of Dokuz Eylül University for giving me the opportunity of my undergraduate and graduate education.

This thesis was financially supported by the National Scholarship Program for PhD Students (2211) from The Scientific and Technological Research Council of Turkey and by the SANTEZ program of the Republic of Turkey Ministry of Science, Industry and Technology (project grant no: 00343.STZ.2008-2). I gratefully acknowledge these supports.

Ziya Haktan KARADENİZ

DETERMINATION OF HEAT TRANSFER AND FLOW CHARACTERISTICS OF SPLIT AIR CONDITIONERS BY INFRARED THERMOGRAPHY AND PARTICLE IMAGE VELOCIMETRY

ABSTRACT

In this thesis, velocity pattern inside and outside a split type air conditioner (SAC) indoor unit is visualized experimentally by Stereo Particle Image Velocimetry (SPIV) method. Furthermore, a novel method called Meshed Infrared Thermography (MIT) for determining and visualizing the temperature profile in an air flow field was introduced and used to investigate the temperature distribution at the outflow of the SAC indoor unit.

The success of the MIT method was investigated by using it for the determination of the temperature distribution inside a cylindrical jet and it is shown that the MIT method is adequate for visualizing the temperature distribution at different flow sections. The outflow and some parts of the inner flow of the SAC indoor unit were experimentally investigated for the first time in the literature, and the complex flow structures and temperature distribution were visualized. The primary flow structure at the outflow of the device is a planar jet, and a transverse flow is shown under the planar jet which exists independently from the device type, Cross-flow fan (CFF) type, and CFF rotational speed; although the transverse flow's behavior may change with these parameters. In addition, the effects of the device edges on the planar jet are shown.

Keywords : meshed infrared thermography, stereo particle image velocimetry, split air conditioner

SPLİT KLİMALARIN ISI TRANSFERİ VE AKIŞ KARAKTERİSTİKLERİNİN KIZILÖTESİ TERMOGRAFİ VE PARÇACIK GÖRÜNTÜLEMELİ HIZ ÖLÇÜMÜ İLE BELİRLENMESİ

ÖZ

Bu çalışmada, split klima (SK) iç ünitesinin içindeki ve çıkışındaki akış Parçacık Görüntülemeli Hız Ölçümü (PGHÖ) yöntemi ile deneysel olarak görselleştirilmiştir. Ayrıca, bir hava akışının içerisindeki sıcaklık dağılımını belirlemek ve görselleştirmek için kullanılmak üzere Ağ Yapılı Kızılötesi Sıcaklık Ölçümü (AYKSÖ) isimli yeni bir yöntem geliştirilmiş ve SK iç ünitesinin çıkışındaki akış içerisindeki sıcaklık dağılımını belirlenmesinde kullanılmıştır.

AYKSÖ yönteminin başarısı, yöntemi silindirik bir jet akışının içerisindeki sıcaklık dağılımının belirlenmesinde kullanarak incelenmiş ve AYKSÖ yönteminin farklı akış alanlarındaki sıcaklık dağılımının belirlenmesi için uygun olduğu görülmüştür. SK iç ünitesinin çıkışındaki ve içindeki bazı bölgelerdeki akış literatürde ilk kez incelenmiş olup, karmaşık akış yapıları görselleştirilmiştir. Cihazın çıkışındaki birincil akış yapısı bir düzlemsel jet akışıdır ve bu jetin altında enlemesine bir akışın daha olduğu ve bu ikincil akışın cihaz tipi, teğetsel fan tipi ve teğetsel fanın dönme hızından bağımsız olarak var olduğu gösterilmiştir. Ancak, enlemesine akışın yapısı bu değişkenlerden etkilenmektedir. Bunun yanında, cihazın kenarlarının düzlemsel jet akışı üzerindeki etkileri de gösterilmiştir.

Anahtar sözcükler: ağ yapılı kızılötesi sıcaklık ölçümü, parçacık görüntülemeli hız ölçümü, split klima

CONTENTS

Page

CHAPTER ONE
INTRODUCTION

Recently, energy efficiency has become one of the most important design criteria for engineering applications. Governments and international organizations firmly control the energy demand of devices through regulations and international standards. Because household appliances involve a large market and constitute an important component of energy consumption, their production and sales are also strictly controlled by the standards; this means that producers pay more attention to the design and production processes. Another important point is that consumers require more-efficient and well-designed products for improving their quality of life.

Split air conditioners (SACs) as everyday household or office appliances have become more and more popular for small scale air conditioning demands. Although they are ordinarily used in the summertime for cooling and dehumidifying processes; they are also being used for the heating processes for the buildings which do not have a central heating system. As with other household appliances, the demand for high-performance split air conditioners (SACs) has increased rapidly. Adequate air supply and heat transfer performance to assure thermal and acoustic comfort, together with high energy efficiency and vibration control, are important design constraints for the thermal and flow design of the SACs.

The performances of the SACs depend on both the indoor and outdoor units therefore the indoor and outdoor units of the SACs need to be coherent. However, indoor units require more attention because of the necessity for high performance on a small scale and the more complex flow characteristics of the cross flow fan (CFF). In addition, the interaction between the user and SAC device is through the indoor unit. Thus, the designs of the casing of the CFF, the CFF parameters (the number of the blades, blade shape, fan diameter, the distances between the CFF and the rear wall and the vortex wall etc.) and the outlet section geometry of the SAC indoor unit are more difficult and important.

1.1 Split Air Conditioner Indoor Unit

Operation of the SACs is based on the cooling cycle principle which has four main components; two heat exchangers (evaporator and condenser), a compressor and an expansion valve. Outdoor unit contains three of these components (heat exchanger, compressor and expansion valve) whereas the indoor unit contains only one heat exchanger. The fin and tube heat exchangers (FTHEs) inside the SAC indoor and outdoor units work as both evaporator and condenser depending on the different demands of the end user. The FTHE inside the indoor unit is an evaporator for the cooling mode and condenser for the heating mode. The operation of the FTHE inside the outdoor unit is vice versa. Two fluids are used to make this operation possible and to transfer heat from a low temperature region to a hotter environment. These two fluid domains for the SAC operation are the air and the refrigerant. Although the refrigerant side heat transfer has an important role on the performance of the device, more attention should be paid on the air side because of the lower heat transfer capability of the air.

SAC indoor units have three main parts for conditioning the air; FTHE, CFF and outer shell (Figure 1.1). Air flow is driven by the CFFs in SAC indoor units and the flow obtained by the CFF should be controlled carefully for ensuring thermal and acoustic comfort for indoor applications of the SACs. Besides, to reduce the energy demands for air conditioning it is important to control the flow of CFFs for improving their performance. The form and characteristics of this flow depend on the CFF parameters, the outlet section geometry and the directing airfoil's geometric parameters. Therefore, these parameters should be well designed to control the outflow of the SACs, however except the outlet section geometry of the body, they depend on the different demands of the end user.

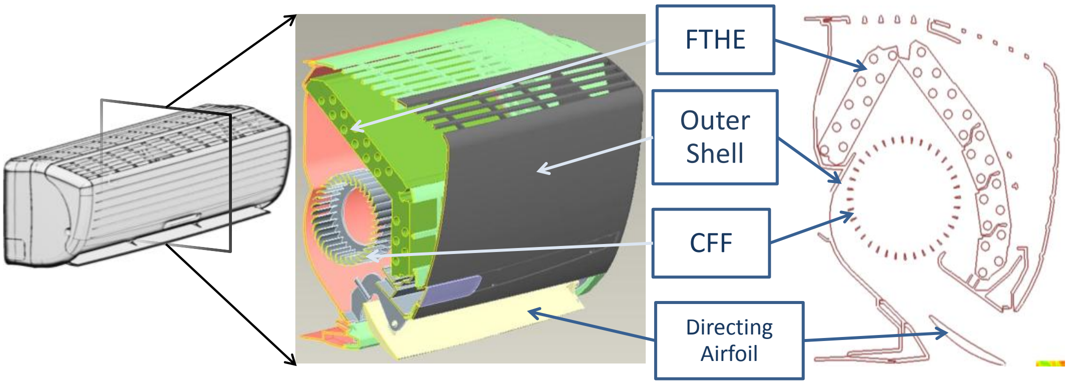

Figure 1.1 SAC indoor unit components.

Air enters the device through the air-return grill where and following through the fins of the heat exchanger, which straightens the flow, air enters the cascades of the airfoils of the CFF in the radially inward direction on the upstream side, flowing through the interior of the impeller passes radially outward through the balding a second time. The flow is directed backwards and squeezed between the rear wall and the eccentric vortex. The eccentric vortex which provides the air suction from the upstream and behaves like a seal against the reversing flow of the air from the downstream is the main source of the CFF flow. The shape and position of the eccentric vortex strongly depend on the vortex wall's geometrical parameters. The outflow of the SAC indoor unit is a planar jet flow under ideal conditions (when there are no side walls or any other obstacles inside the flow). A schematic of the flow inside the SAC indoor unit and the outflow is given in Figure 1.2.

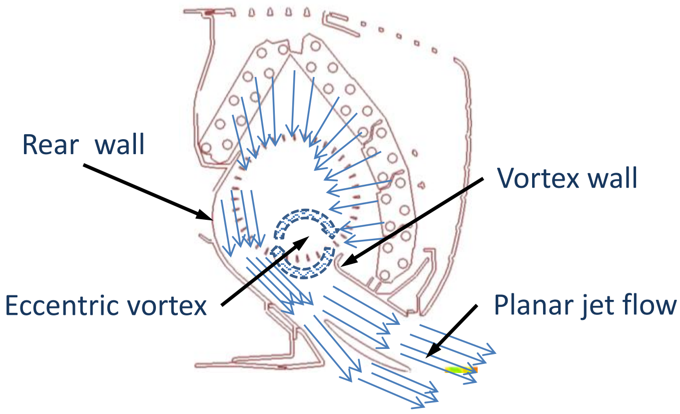

Figure 1.2 Flow structure inside the SAC indoor unit and components of the device to control the flow.

Although the CFFs are known to be producing a two dimensional planar jet flow, their high dependency on the surrounding objects such as the vortex wall, rear wall, device edges etc. causes fluctuations inside the flow and changes the flow conditions. These fluctuations are the sources of the heat transfer, vibration and noise problems; hence they are important for the thermal and acoustic comfort. In order to minimize the problems, the inner design and the properties of both the CFF and casing should be optimized. The flow visualization methods are very useful for identifying these deviations from the ideal conditions.

1.2 Objectives of the Study

The objective of this research is to visualize experimentally the velocity distribution inside and outside a SAC indoor unit by Stereo Particle Image Velocimetry (SPIV) method and to visualize the temperature distribution at the outflow of the SAC indoor unit by infrared thermography. The secondary objective is to develop a method (Meshed Infrared Thermography, MIT) for determining and visualizing the temperature profile in an air flow field.

1.3 Outline of the Thesis

This thesis is composed of seven chapters.

In the first chapter; an introduction to the study is given with some information on SAC indoor units and the objectives of the study.

In the second chapter; the literature review about the CFFs, SAC indoor units, and measurement methods is presented.

In the third chapter; the experimental setups for both the velocity and temperature measurements are given and the validation study of the MIT method is presented.

In chapter four; the results of the flow measurements at the outlet section of a SAC indoor unit is given with the discussion about the characterization of the outflow of the SAC indoor units.

In chapter five; the effects of different parameters on the characteristics of the outflow are presented by the measurements at the outflow of Model 1 with a skewed CFF, and at the outlet of Model 1 with a straight CFF at different fan speeds. In addition, the change of the flow structures at the outlet section of Model 1 for the different angular positions of the directing airfoil is presented.

In chapter seven; the temperature distribution in the outflow of Model 1 with a skewed CFF is given with a discussion on the temperature distribution characteristics of the SAC indoor unit.

And finally in chapter seven; concluding remarks and the future work recommendations are given.

CHAPTER TWO
RELATED WORK

CFFs are the main parts of the SAC indoor units for driving the flow and they are frequently used for heating, ventilating and air conditioning (HVAC) and industrial applications. The eccentric vortex inside the CFF characterizes its flow and directly affects the performance. Fan casing (rear wall and vortex wall), CFF dimensions, and position are the main parameters which control the shape and the position of the eccentric vortex. Complicated relations between these parameters and the performance of the CFF have not been totally explained yet; therefore the research on the performance of the CFFs remarkably developed during the last decades.

CFFs have been used for more than a hundred years in the industrial applications (firstly for the ventilation of the mines), but they were very inefficient at the beginning of their usage. After the other types of fans were developed, CFFs disappeared for a very long time, until they are re-discovered in the middle of 20th century. Eck (1973) discovered and visualized the eccentric vortex inside the CFF, which made the research on them develop remarkably.

There are some studies on the CFFs in which fan performance characteristics under different operating conditions were investigated. The experimental setups in those studies were consisted of wind tunnels with some instrumentation on them for studying the pressure distributions and determining the flow rates. Yamafuji worked on the CFFs experimentally and analytically (Yamafuji, 1975a, 1975b), by visualizing the transient process of the formation of an eccentric vortex, the flow pattern under the steady rotation conditions and the interference between a counter vortex and the eccentric vortex inside the CFF. A series of papers were published under the coordination of Susumu Murata between 1976 and 1995 dealing with experimental investigation of CFFs. They built a test apparatus in which rotors, casings and inner guide vanes having different properties could be connected and detailed pressure and velocity measurements could be made. Firstly Murata & Nishihara (1976a, 1976b) studied the effect of the casing, showing that the geometry of the casing results to stable or unstable performances although the same rotor was used for both cases. They also investigated the flow patterns by using the fans with different geometric parameters. Then Murata, Ogawa, Shimizu, Nishihara & Kinoshita (1978) studied the effect of the inner guide vanes on the performance. They made measurements of the internal flow of rotors with a Pitot tube.

In (1994), Tanaka & Murata considered the Re number and fan size effects on the flow characteristics and performance curves for obtaining an affinity law for the CFFs. The flow coefficient's change with respect to total pressure rise coefficient is defined as the CFF performance curves, similar to the definition for the other types of fans. They used two different casings that they determined to be stable and unstable in their early works. As a result, it is shown that the performance is effected by the size of the fan and Re number for relatively law chord length based Re numbers ($<1\sim1.5\ 10^4$). For higher values of the Re number than the critical value, Re number effects tends to saturate but the fan size has an effect on the performance meaning that the CFFs doesn't obey the conventional affinity law for the fans. Hence, it is concluded that the diameter of the rotor should be introduced as a parameter to represent the performance of the CFFs of different sizes on a uniform curve. The effect of the gap between rotor and vortex wall, surface roughness, thickness of blade and flow conditions of the suction side were also considered for proving that their results are unaffected from the production, assembly and flow condition errors.

Uskaner and Göksel studied the effects of the rotor parameters (geometry and number of airfoils) and rear casing on the CFF performance experimentally (Uskaner & Göksel, 1999a, 1999b), using an open-circuit CFF test rig similar to that Murata et al. used in their experiments. Six different airfoil geometries, three different numbers of airfoils and 27 different rear wall geometries were determined systematically to identify their effects on the CFF performance. The static pressure coefficient and fan efficiency are introduced in the performance curves together with the flow and total pressure rise coefficients. They showed that the performance increases with the increasing airfoil numbers and the cord length. Besides, airfoils having a profile of circular arc are more efficient than the ones having angle profile. Also, the effect of the stager angle of the airfoil was considered and 10° was said to be the minimum value to have a flow, and 30° was the most efficient stager angle. The results for the different rotational speeds of the rotor were also given. Although one of the rotors that they used (with the airfoil profile blade 1, outer diameter 142 mm and the inner and outer diameter ratio 0.83) is similar with the one that Tanaka & Murata (1994) used (having an outer diameter 135mm and inner and outer diameter ratio of 0.85); their results do not agree well with each other. The results of Uskaner and Göksel (Uskaner & Göksel, 1999a), are similar with the results of Tanaka and Murata (1994) for the so called unstable case model such as; discharge pressures rapidly increase as the flow rate increases. However, the sudden decrease shown by Tanaka and Murata cannot be seen in the results of Uskaner and Göksel. This difference may be due to the unsimilar rear and vortex wall shapes and should be discussed in detail. Furthermore, the results of the performance curves for the stable case model are totally different. The geometric parameters of the rear wall and outflow section were also investigated systematically and the results were presented by the performance curves as well as some comments on the suitable values for different dimensions. It must be impressed that, although the geometry of the casing was investigated in a very wide range; there is no sign of such a casing with the unstable performance, different than the results given by Tanaka and Murata (1994) .

The flow visualization methods were also used in the CFF studies to figure out the effects of the different parameters on the performance of the CFFs. Particle Image Velocimetry (PIV), Particle Tracking Velocimetry (PTV), Laser Doppler Anemometry (LDA), smoke or dye injection are the experimental flow visualization methods which have been used for this purpose. Porter and Markland (1970) measured the internal flow of a CFF using a hotwire probe and flow visualization and this was the first time when a quantitative velocity information was taken from the inside of the CFF.

In their latest study Tanaka & Murata (1995) made some upgrades on the apparatus such as changing some parts with the transparent ones for the need of optical access while using the LDV method for the measurements inside the CFF. It is the earliest paper of the LDV method used for a CFF analysis to our knowledge. Combining the inner flow field data from LDV and static pressure measurements with the results of their previous study, they proposed a new procedure to represent the performance of the CFFs. The velocity vectors obtained from the LDV measurements were used to calculate the normalized flow parameters; such as streamlines, vorticity, and velocity fluctuations. It was shown that, increase in the dimensions of the rotor makes the flow more active which means that the time-mean velocity, vorticity, velocity fluctuation or pressure drop in the eccentric vortex increase with the dimensions of the rotor. Besides, comments on the scale effects and formation of the eccentric vortex due to the reciprocating motion of the cascades of airfoils that are located along the periphery of the rotor were given. They noted that CFFs operate quite unstable with highly turbulent internal flow field and the flow is driven by the random fluctuations of the flow conditions. However, they managed to give a universal representation of the fan performances by defining Re number based coefficients called the reduced flow coefficient and the reduced total pressure rise coefficient.

In 1996 and 1997, Tsurusaki, Shimizu, Tsujimoto, Yoshida & Kitagawa (1996), and Tsurusaki, Tsujimoto, Yoshida & Kitagawa (1997) studied internal flow of the CFFs by flow visualization, using PTV method for the first time, for determining the streamlines and vorticity distribution of the flow passing through the CFF. Water was used as the fluid in their study to overcome the difficulties of the seeding particles and proper illumination. The rotational speed of the fan was maintained at 50 rpm which is a very slow speed compared with the actual rotation of CFFs inside the air conditioners. The accuracy of the PTV method was tested by the measurements made with a pitot tube, and it was shown that the results were in good agreement. They showed that the center of the eccentric vortex moves to the rear casing side and the area of the recirculating region increases as the flow rate decreases. This effect was seen as a slight change of the center of the eccentric vortex towards the vortex wall as the CFF diameter increases (which mean the flow rate also increases) in the study of Murata & Tanaka (1995), but not emphasized on the results. Another important result of this study was that, the CFF was divided into parts of pump and turbine for defining the energy input and output from the CFF to the flow. According to this classifying, most of the energy is given to the flow and eccentric vortex in the pump region located at the rear casing side. In the eccentric vortex, some of the energy of the flow is taken back to the impeller (turbine region). Another but weak pump region is located at the CFF inlet. The authors reported that PTV is useful for the measurements of the CFF flow field and the quantitative experimental analysis of the CFF performance.

In the later study of Tsurusaki et al. (1997), the details of their work was given as the vorticty distributions used for the prediction of the vorticty diffusion model of the eccentric vortex. Besides, the mechanism of vorticty supply and diffusion in eccentric vortex was explained and effective kinematic viscosity was found to be 200-900 times greater than the molecular kinematic viscosity which is a result of the very strong mixing in the CFF. Furthermore, the random walk model was used as the numerical analysis to compare their results with the experiments and good agreement between them was obtained. They showed that the work done by the impeller in the flow region is significantly larger than the work done in the eccentric vortex region at high flow rates, and decreases as the flow rate decreases.

Because of the insufficient investigation on the CFF similarity, Lazzarotto, Lazzaretto, Martegani & Macor (2001) studied the effect of the Re number on performance for the different casing shapes and the similarity of CFFs. Although Tanaka and Murata (1995) made a conclusion on this subject by defining the Re number based coefficients to represent the CFF performance, it was far from being a universal design suggestion since only two casings was used to validate their results. Therefore, Lazzarotto et al. (2001) designed a series of experiments using five geometrically similar CFFs having different diameters and matching them with five different pretested rear casing walls. The position of the vortex walls for each situation was determined by their previous experiments which were resulted more stable characteristics. Every configuration of the rear walls and CFFs were than subjected to the tests to identify their characteristics. The results of this study again showed some differences than Tanaka and Murata (1995) which can be given as; critical Re number depends on the casing shape (4000-15000) and scale effects have limited influence on CFF performance.

Using the same test rig in their previous study Lazzaretto, Toffolo & Martegani (2003) made more experiments to find which are the parameters most affecting fan performances and the effects of their design choice. They showed that five variables are the most significant which are; the rear wall radial width, vortex wall height and thickness, internal and external blade angles of the impeller. Lazaretto (2003) made an original criterion to parameterize systematically a CFF configuration according to the most significant variables defining the geometry and then affecting the performance and efficiency. They further investigated experimentally the effects of the throttling conditions and different geometries of the fan casing on the flow field pattern within the impeller by velocity and pressure measurements (Toffolo, Lazaretto, & Martegani, 2004). Furthermore, Tofollo (2005) used the experimental results of their previous studies on CFF performance for validating the Computational Fluid Dynamics (CFD) analyses and used the CFD analyses for explaining how a specific set of design parameters corresponds to a given performance and efficiency in a theoretical perspective. Finally, Toffolo (2004) presented a theoretical approach to analyze systematically their previous experimental results in order to come to a unified interpretation of the characteristic curves for all fan configurations. A normalized stream function was introduced and applied to reveal the theoretical archetype of performance and energy curves.

Kim and Oh (2004) utilized the mean stream line analysis procedure for the prediction of the performance characteristics of CFFs. The results of the overall performance predictions were compared with the test data from the literature and the accuracy of the proposed method were demonstrated. Govardhan and Venkateswarlu (2003) studied experimentally the effect of the impeller geometry and the vortex wall shape on the flow field of the CFFs. They made pressure measurements along the circumferential direction around the CFF and investigated the flow field’s change. It is concluded that, the flow parameters like total pressure and static pressure do not vary along the span except near the side walls, therefore the flow inside CFF is said to be 2D. However, the flow along the circumference of the fan varies substantially. In a later study, Govardhan and Sampat (2005) used CFD method to analyze the effect of the blade geometry on the flow and performance of the CFFs. Similarly, Kim, Kim, Park & Kim (2008) experimentally and numerically studied the performance of a CFF with three different shapes of the rear wall and five different setting angles of the vortex wall.

Gabi and Klemm (2004) experimentally and numerically studied the aerodynamics of the flow and vortex regions inside the CFF. This is the first PIV study on CFFs in the literature to our knowledge. They made PIV measurements and CFD analyses for different flow coefficients and showed that PIV measurements in combination with CFD are useful tools for the design purposes of the CFFs.

Tsai, Tu, Li & Wang (2006) employed the smoke injection technique, for investigating the noise emission, flow style and fan's performance, on three different types of rotors having different rotor skew angles. The skewed angle rotors are commonly used in split air conditioners indoor unit, therefore this study may be important for us to compare our results for the models with this type of rotors. They used only a small portion of the fan, using the advantage of the two dimensional flow characteristics of the CFF. They found that for a better compromise between acoustic and flow performance, one pitch skewed rotor is the best choice. It is mentioned that, because of the skewed angle rotor, continuous pressure waves come out from the blades when they are passing through the vortex wall (tongue), and this causes 3-D axial variation in flow characteristics and therefore, using PIV or LDV methods becomes difficult to observe the flow. Furthermore, they showed that the outflow of the CFF deviates from the normal direction of the rotor-axis for the skewed rotors and this deviation increases for the larger rotor skew angles. In thesis, stereo PIV technique was used to visualize the 3D flow field at the outlet of the SAC device.

Funaki, Kimata, Hisada & Hirata (2006) and Hirata, Iida, Takushima & Funaki (2008) studied short span CFFs without casing (rear wall and vortex wall) using the

PIV method for the flow visualization of the CFFs. The same experimental setup was used for both studies. Although flow cannot be controlled without rear and vortex walls, they asserted that they eliminated the complex factor (casing) that influence the characteristics and compared fans having different aspect ratios. It is said that, when the CFF is inside the casing, it is difficult to estimate their fundamental characteristics.

Noël, Farall & Casarsa (2007) studied the aero-acoustics of a CFF both experimentally and numerically. The experiments about the velocity distribution were made by a PIV system. Although their main goal was validating the commercial CFD code for noise reduction, their results of PIV and the experimental setup contains useful knowledge for our study. They gave both the qualitative results of the computed and measured velocity distributions as contour plots and the quantitative comparison of them as a graphic. They showed that, the flow resulting from the CFF may have some unexpected 3D characteristics different than the generally expected flow conditions of the CFFs (2D or planar jet flow); namely there is a recirculation region at the outlet of the CFF on the side where the driving motor is situated, a two peak jet flow was observed for which the existence was explained by the effect of the volute side walls and the metal ring that is located at the wheel center plane and used to avoid deflection of the blades. Furthermore, they reported a good match between the experimental and numerical results, however, the CFD method was said to be over-predicting the flow speed.

CFD analyses and measurements using hot-wire anemometers were used to study the flow configuration and performance of a CFF with two outflows by Gebrehiwot, Baerdemaeker & Baelmans (2010). The effects of the position of the vortex wall and the size of the inlet on the fan performance were studied numerically by using unsteady Reynold’s Averaged Navier-Stokes (URANS) equations. They showed that the position of the vortex wall plays a crucial role for the CFF performance, in particular the airflow division between the two outlets and mass flow rate division between the two outlets is influenced by the rotor outlet opening.

Some of the scientists focused on the noise characteristics of the CFFs and thereby the SAC indoor units. Moon, Cho & Nam (2003) and Cho and Moon (2003) investigated time accurate viscous flow solutions for the prediction of unsteady flow characteristics and associated aero-acoustic blade tonal noise of a uniform and two random pitch blades CFFs, by solving the 2D incompressible Navier-Stokes equations. The accuracy of the numerical method was assessed by comparing the fan performances with the experimental data. In addition, the unsteady vortical flow motions such as; vortex shedding from the blades, formation of the eccentric vortex and the vortex interactions with the stabilizer were visualized from the unsteady numerical simulations. Chen, Li & Huang (2008) also performed numerical simulations for studying the noise predicted from a CFF under different operating conditions for a SAC indoor unit. Gan, Liu, Liu & Wu (2008) investigated the eccentric vortex induced pressure fluctuations in a CFF and the vortex-stabilizer interaction numerically. In addition, sound pressure in the far field was obtained with a noise experiment for a CFF inside a SAC indoor unit.

Dang and Bushnell (2009) reviewed the fundamental aerodynamics and flow regions of CFFs, CFF propulsion and flow control concepts, and experimental data for fans intended for aircraft applications. The experimental data was also compared with the calculations using unsteady Navier-Stokes methods, showing the state-of-the art in flow field and performance prediction capability.

In e very recent study, Casarsa & Giannattasio (2011) experimentally investigated the 3D flow field in the CFFs by using PIV method and pressure measurements. One CFF was placed in two different casings and the performance of the both CFF configurations were investigated at three different rotational speeds (1000, 1300 and 1600 rpm) by the curves of total pressure vs. flow rate. The PIV measurements were made only at the rotational speed of 1300 rpm and for the flow coefficient (φ) of 0.6, because of the stable characteristics of the both fan configurations at this flow conditions. PIV measurements were made for the planes normal and parallel to the fan axis, despite the well-known difficulties of obtaining the optical access inside the impeller. The internal flow planes were visualized and illuminated through the moving blades, and the flow data was obtained by properly processing a large number of PIV images (up to 5000 images per plane). The detailed analyses of the PIV data normal to the fan axis showed that the existence of axial velocity components inside the blading and the volute are significant. Further investigations at the planes parallel to the fan axis confirmed the existence of the 3D recirculation structures that develop near the casing end walls at the discharge of the fan. Both the experimental and numerical investigations on the CFFs in the literature before this study assumed a two dimensional flow through the fan, which seems to be reasonable for the high length/diameter ratio cases. However, as a result of this study, it is recommended that caution should be exercised in design of CFFs from the predictions of 2D flow models or from the experimental data in a single transverse plane of the fan especially when the length/diameter ratio of the CFF is small.

There is limited information about the numerical flow visualization of the SAC indoor units and almost no study exists about the experimental flow visualization of the SAC indoor units in the literature, except the CFFs investigations (given above) by using the numerical simulations and the flow visualization methods without including the device's parts such as fin and tube heat exchanger, and outer cover etc. There are some numerical studies which are directly dealing with the flow inside SAC indoor units. Shih, Hou & Chiang (2008) simulated the SAC indoor unit by a commercial CFD code to develop similarity laws for the CFF performance. Owing to the proved success of the numerical methods for simulating the CFF flow by the former researchers, they used the CFD method with systematic analysis to create enough flow field data to obtain the similarity laws of the CFFs for the CFF constructions of a simplified flow duct, a conventional SAC indoor unit and a SAC indoor unit without the air-return grill and heat exchanger. The study mainly focused on the effect of the rotational speed of the CFF on the air supply performance and it was found that; the total pressure of the eccentric vortex center was proportional to the square of the fan rotational speed for all CFF constructions. Furthermore, the total pressure rise between the entrance and the exit was proportional to the square of the fan rotational speed for the simplified flow duct, however; this is not true for the

CFF constructions of the convectional SAC indoor unit for the low RE number flow conditions.

Xue, Gan, Wang & Wu (2010) numerically simulated the internal flow of a SAC indoor unit, containing both the CFF and the fin and tube heat exchanger (FTHE) under refrigerant operating condition using user-defined functions. The drying effect of the FTHE on the humid air and the performance of the CFF under dry or humid air conditions were discussed.

A detailed numerical analysis of the effect of blade angle on the flow characteristics in the vicinity of diffuser blades of a SAC indoor unit was made by Seo, Kim & Kim (2009). Three different angular positions matched with three different CFF speeds for studying their effects on the flow characteristics, and the flow patterns were visualized. The vortex distributions for the different flow conditions were investigated and the effect of the vortexes in the vicinity of the diffuser blades on the outflow characteristic was discussed. Although the flow characteristics of the CFF alone and the SAC indoor unit were studied by other researchers, no one included the effect of the diffuser blades on their analyses. Later in this thesis it will be shown that, the angular position of the directing airfoil (diffuser blades) may affect the position of the eccentric vortex in some cases, which may lead to the totally changed flow conditions inside the device and thereby the performance of the SAC.

The only study found in the literature on the SAC indoor unit by using the PIV method was prepared by Lee, Na, Kang & Ko (2011). Flow distribution at the inside and outlet section of a SAC device was visualized by PIV measurements and 2D CFD analyses for improving the efficiency. Although, a number of design improvements were proposed in this study (solution for the condensation problem and optimization of the CFF rib shape), the results are not given in detail and they are not well represented. However, the success of the PIV method for the characterization of the SAC indoor units is apparent and further investigations are needed for better designs.

Determining the temperature distribution inside a flow section or all through the flow is another important point for the thermal comfort and characterization of the SAC device. However, neither experimental nor numerical studies exist about the temperature distribution of a SAC indoor unit in the literature. For the temperature measurements, most of the conventional methods are point based, for which a sensor (e.g. thermocouples) or a group of sensors are positioned in the investigation area. It is simple, reliable and cost effective to use the sensors for the temperature measurements. However, there may be some local effects of these sensors on the flow. Another important problem is positioning and controlling them.

Planar Laser Induced Fluorescence (PLIF) or Particle Image Thermography (PIT) is a noncontact, whole-field temperature measurement and visualization technique which is used to determine the temperature distribution inside a fluid section. It is based on seeding the flow with fluorescence particles that change color with the temperature and capturing the images of these particles while they are passing by a laser light sheet (Dabiri, 2009).

Infrared thermography is another temperature measurement method which is used to determine and visualize the surface temperatures of the objects. The temperature distribution data can be used for different investigations such as medicine, agriculture, environment, maintenance, non-destructive evaluation and thermo-fluid dynamics (Meola & Carlomagno, 2004). Infrared thermography is widely used for determining the temperature distribution on the substances which are opaque for the radiation at the infrared wavelength. However, the air like gaseous fluids are transparent for the radiation at the infrared wavelength, therefore it is impossible to measure the temperature at any point inside the air. Nevertheless, some indirect measurement techniques were developed for determining the convection characteristics of the flows by visualizing the surface temperature distribution of the solids using infrared thermography (Astarita, Cardone, Carlomagno, & Meola, 2000), (Astarita, Cardone, & Carlomagno, 2006). By this manner; the infrared thermography method is used instead of the heat flux sensors for measuring the heat fluxes as well as to investigate the surface flow behavior over complicated body shapes. The non-intrusive characteristic of the infrared thermography method allows to get rid of the measurement errors occurring from the direct measurement techniques.

The basic technique for visualizing the temperature distribution inside the airflows by placing a solid media within the air stream and visualizing by infrared thermography was originally proposed by Anderson, Hassani & Kirkpatrick (1991) and used to visualize ventilation flows in rooms and automobiles (Burch, Hassani, & Penney, 1992). Comparison of the results with the calibrated thermocouple data yielded an accuracy of ±1.3 °C. Furthermore, they used a 0.25 mm thick fiberglass screen with a porosity of %70 for reducing the time response of the measurements. But the details of the work were not published and the development of the technique was limited.

A whole field flow visualization technique based on the infrared thermography was developed by Narayanan, Page & Seyed-Yagoobi (2003). A trace quantity of sulfur hexa-fluoride (SF_6) gas injected into the flow field of an impinging jet to detect the intensity patterns using a scanning IR thermography system with a single 8-13 μm bandwidth detector. However, this method did not deal with the temperature distribution inside the airflow and not attracted much attention from the latter researchers.

Cehlin, Moshfegh & Sandberg (2002) proposed a variation of the method developed by Anderson et al. (1991) for the visualization of air temperatures and air flow patterns over a large cross section of the low velocity diffusers. They placed a measurement screen inside the flow and measured the screen temperature by an infrared camera to determine the air temperature. Black painted paper or plastic sheets are used as the measurement screen. The heat transfer with the surrounding surfaces is an important factor for the measurement mesh because of the big view factors between the measurement screen and the surrounding walls. Another important point about the measurement screen is the conduction heat transfer inside the screen itself. In addition, measurement screen divides the flow into two parts therefore it should preferably be used for the two dimensional flows and/or when the velocities are small and the flow is calm. Nevertheless, for certain radiative conditions (high emissivity for the screen, known surrounding wall temperatures and view factors between the screen and surrounding walls etc.) as well as the low thermal conductivity for the screen and low flow velocities, this method gives sufficient results for determining the temperature distribution inside the air flow.

An application of the measurement screen method proposed by Cehlin et al. (2002) on the temperature measurement and visualization of the air curtain devices was made by Neto, Gamerio Silva & Costa (2006). The flow velocity at the outlet of the air curtain device was changed up to 8 m/s the change of the shape of the vertical jet occurring from the device was investigated. Although the results are useful for understanding the flow topology and temperature fields, authors concluded that the intrusive structure of the measurement screen introduced some perturbation on the analyzed flow and the temperature of a point an the measurement screen is not exactly the same as the one of the air in the same location. Another application of the measurement screen method was on the buoyant jet in a ventilated room (Elvsén & Sandberg, 2009). The instantaneous velocity and temperature fields close to a diffuser for displacement ventilation were measured and the air flow patterns were visualized by Particle Streak Velocimetry (PSV), PIV and infrared thermography methods. They used a two sided measurement screen with one side is made of thin coarse paper and the other side is aluminum foil to decrease the radiation from the background as was offered before by Cehlin et al. (2002). However, this may cause an increase of the in-plane conduction heat transfer for the measurement mesh which will lead to errors in the measurements.

A modification on the measurement screen method was made by Neely (2008), by replacing the measurement screen with a highly emissive and highly porous mesh for improving the visibility of the screen and minimizing the disturbance of the flow field. In addition, the filaments of the mesh must be fine enough to reach the gas temperature, the mesh weave must be fine enough to provide a uniform view for each pixel of the camera, and the reflectivity of the mesh material should be low to minimize the error due to the reflection of the surrounding radiation to the camera. The effects of different parameters (material type, flow conditions, orientation of the mesh etc.) on the performance of the method were investigated by applying it on the visualization of the flows with different temperatures. Despite its small upstream influence, a transverse mesh is responsible for a strong downstream impact resulting both in the formation of wake structures and in the alteration of the turbulence levels.

Recently, Gallo, Kunsch & Rösgen (2010) introduced an infrared thermography based experimental technique for the determination of the temperature distribution inside hot gas flows. They used a high porosity mesh made up of a thin electrically conductive wire and calculated both the convective heat transfer coefficient and the local fluid temperature by measuring the grid temperature distributions by an infrared camera.

As seen from the literature, there are not any studies directly dealing with the outflow characterization of the SAC indoor units. In addition, the temperature distribution inside and at the outlet of the SAC indoor unit has not been studied yet. Therefore in this thesis, velocity profile inside and outside a split type air conditioner indoor unit is visualized experimentally by Stereo Particle Image Velocimetry (SPIV) method. Besides, a novel method called Meshed Infrared Thermography (MIT) for determining and visualizing the temperature profile in an air flow field was introduced and used to investigate the temperature distribution at the outflow of the SAC indoor unit.

CHAPTER THREE
EXPERIMENTAL SETUP

Experimental study in this thesis was performed in two parts; Stereo Particle Image Velocimetry (SPIV) method was used for the velocity measurements and Meshed Infrared Thermography (MIT) method was developed and used for the temperature measurements. In this chapter, the parts and flow characteristics of a SAC indoor unit was described first, than the implementation of the SPIV method for the velocity measurement at the inlet and outlet sections of the SAC indoor unit were explained and finally the MIT method was proposed and validated.

3.1 Velocity Measurements

Flow visualization methods have been used since the beginning of the observations on the fluids. Parallel to the development of the science and technology, equipment has been changed together with the power and benefits of the flow visualization methods. In the early investigations, only qualitative methods were used because of their relatively simpler application. The only need for visualizing the flow qualitatively is adding tracer particles into the flow and observing the flow structures or capturing the images of the flow for a later observation. The smoke or dye injection methods are still in use for the investigations on the flow structures in gas and liquid flows, respectively. On the other hand, early quantitative methods that were used for the determination of the flow characteristics were point and probe based (measurements can be done at one point and by the existence of a probe at the measurement point) such as pitot tube measurements. Constant Temperature Anemometry (CTA), Hot Wire Anemometry etc. are other recent point an probe based velocity measurement methods which can be used for investigating large areas when they are positioned on the computer controlled traverse systems. However, point and probe based methods are not suitable for the boundary layer flows (because of their disturbance on the flow) and simultaneous measurements on the different points at the investigation area.

The implementation of the laser techniques to the flow visualization methods has increased the research on the development of the different visualization methods, which leaded the improvement of the high technology optical methods such as Laser Doppler Anemometry (LDA), Particle Tracking Velocimetry (PTV), and Particle Image Velocimetry (PIV). The tracer particles are added into the flow for using these methods as in the case of qualitative flow visualization, however; quantitative information is obtained from the movement of the particles different than only visualizing the flow structures. LDA is a point based velocity measurement method that removed the disturbances of the existence of a probe at the investigation area, therefore velocity is measured non-intrusively. However, the simultaneous measurements of the velocities at the different points are still not possible with the LDA. PTV and PIV are non-intrusive and whole field velocity measurement methods that are used for simultaneous velocity measurements at every point in the investigation area. Early applications of PTV and PIV were limited to the two dimensional steady state flow conditions and time consuming experiments and data processing. With the development of the dedicated high speed lasers, cameras and software together with the increasing CPU and memory capacities of the computers, PIV is now a standard experimental tool for both the industrial research and development applications and scientific fluid dynamics investigations. Recently developed three dimensional three component (3D-3C) PIV method is still in progress, but capable of resolving the complex flow structures. Therefore, employing the PIV technique on highly turbulent flows with 3D flow characteristics became possible with the today's technology.

3.1.1 The SPIV System

Stereo PIV method which needs high technology and sensitive components as well as a sensitively designed experimental setup was used for the in-plane 3D velocity measurements. Due to the sensitivity of the system, all the procedures must carefully be taken into consideration. Limited information was found in the literature about the usage of PIV method on split air conditioners as discussed earlier in the introduction part.

The SPIV system basically consists of two cameras (for in plane three dimensional measurements), laser, fog generator, computer and software to control the components and post processing, timer box and cables. Details of these components are given in Table 3.1. Air is seeded by particles and a light sheet is formed by using a high energy light source (laser) passing through proper lenses. Light scattered by the particles is acquired by the two cameras which are synchronized with the laser source assuring that the photographs are taken just in time. Consecutive image pairs from both cameras are post-processed to determine the displacement of particle groups within elapsed time, resulting to a velocity vector for each interrogation area. Combination of the vectors forms the vector field for the investigated portion of the flow.

Measurements were made in a 3480 x 6840 mm rectangular room in which all the components are placed (Figure 3.1). The positions of the laser, cameras and the measured area with respect to each other and inside the room are very important for the accuracy of the experiments. It is placed on a hanger at 1.5 m above the ground level and is situated on the longitudinal axis of the room such that it blows along the longitudinal axis of the room. The distance between the device and the wall behind the device is 1 m. Therefore, there were enough places around the device to assure that there is no reversed flow from the surrounding walls.

Table 3.1 Specifications of the PIV system components

Component	**Specification**
Laser	135mJ, 15Fps double pulse ND:Yag Laser
Cameras and lenses	Flow Sence Mark II, 4 MPx, square sensor camera. 60mm f2 Zeiss Planar Macro Lens
Computer	Dell T7500 work station, 12 GB ram, Raid 0
Other	Synchronizer and cables
Fog generator	Safex fog generator, with extra clean fog fluid

Cameras and the laser are attached to each other by rigid aluminum profiles to assure that the positions of the cameras and laser don't change while re-positioning all the setup inside the room or just changing the position of the indoor unit. In this manner, cameras and laser can be slid on the profiles to different positions without changing their layout.

Figure 3.1 The test room.

3.1.2 Measurements at the Outlet of the Device

For the first study, outflow section of the split air conditioners' indoor unit was chosen for investigation, because of the relative simplicity of the measurements. Besides, some flow defects and the performance of the device may be determined by measuring the flow on this part. But for the certain determination of performance and flow defects, inner flow must be visualized. Positions of the system components for outflow measurements are given in Figure 3.2. One of the cameras is positioned vertical to light sheet to focus on the particles inside the light sheet easily. The angle between the two cameras is chosen as 35˚.

After the components are positioned, calibration was made which is needed for processing the images properly. A 95 x 75 mm, double layer calibration target which is designed for the stereo PIV measurements was used. Target is placed inside the interested area and cameras are focused on the target as seen in Figure 3.2. The captured images of the target from the both cameras are processed to determine a correlation between the pixel size and the real dimensions in the interested area (Figure 3.3). So that, the data of how many pixels the particle groups moved between the consecutive images can be transformed to the real displacement of the particles and the velocity vectors can be obtained.

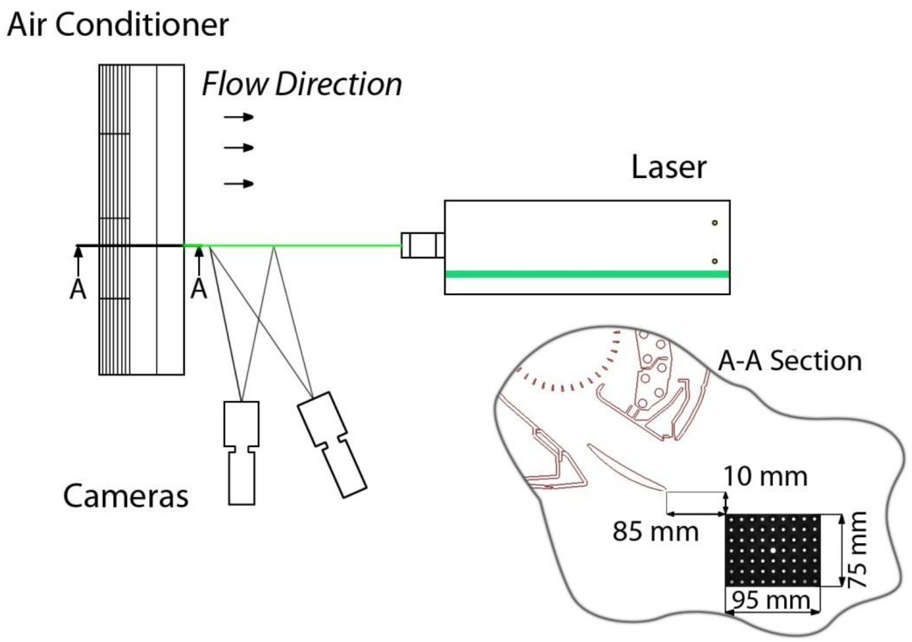

Figure 3.2 Layout of the laser, cameras and device and the position of the target

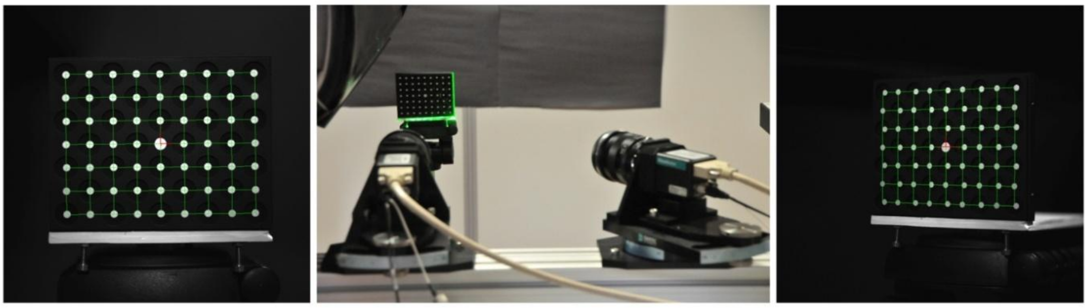

Figure 3.3 Position of the target with respect to cameras and images captured by the cameras for calibration

Once the cameras are focused on the interested area and calibration is made, split air conditioners' indoor unit can be slid horizontally (to right or left) to measure the outflow all through the device without changing the positions of the cameras and laser. The measurements were made for the different cross sections to visualize the flow at the outlet section of the device three-dimensionally. These planes were chosen closer in some parts in which the flow may change rapidly and separated in the parts in which the flow is expected to have small differences due to the two dimensional flow characteristics of the CFF and the design of the device. An example of the selected planes is given in Figure 3.4. The control units and motors of the SAC indoor unit are situated at the left side of the device for most of the models. There is not any flow coming out of the device at this part therefore, the symmetric structure of the device changes and this might be changing the outflow structure, too. Therefore, this part of the device was also investigated for some of the experiments.

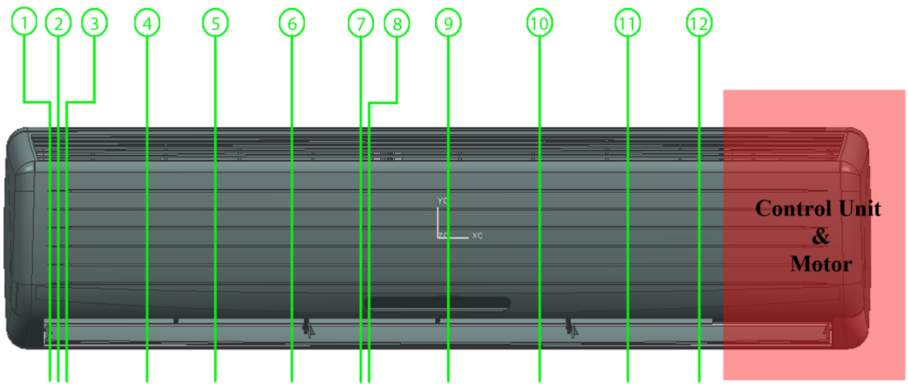

Figure 3.4 Investigated planes on the device

The last step for determining the velocity vectors is seeding the flow. Fog is used for this purpose, which is generated from liquid glycol-water mixture having an average diameter of 1µm. Before the experiments, test room is filled with the fog, assuring that enough particle density is supplied all through the measuring time. The images of the particles passing through the light sheet are captured by the cameras to obtain vector field of the flow.

The dimensions of the investigated area depend on the positions of the components of the SPIV setup. To see a wider area at the outflow section, cameras may be drawn back but this leads to difficulties of picking out the particles and larger un-illuminated areas at the top and bottom sides of the images which means the total visualized area becomes smaller. A wider light sheet may be used to solve this problem, however light density reduces and visibility of the particles also decreases for constant laser power and a wider light sheet. Therefore, the investigation area for each set up is limited and the largest area used for this thesis was 190 x 145 mm. Separated experiments should be done for investigating larger areas and the results should be stitched afterwards. An area which includes the main flow passing through its diagonal was visualized for the outflow investigations. A sample setup and the investigated area are given in Figure 3.5.

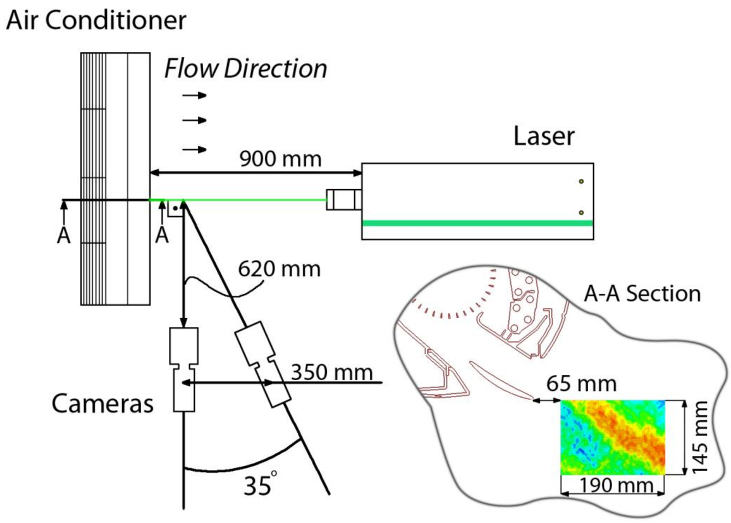

Figure 3.5 Layout of the laser, cameras and device and the investigated area

3.1.3 Measurements Inside the Device

A light sheet should be formed and a camera or cameras should be positioned as they would see the light sheet perpendicularly in the area of interest. Furthermore, the calibration target should be positioned exactly at the same investigation area on the measurement plane before the model is placed in front of the camera or cameras and the light sheet is formed. As a result of this complex measurement technique, a device taken from the manufacturing line cannot be used for the investigations of the inner flow. Therefore, a new experimental setup and also a new model of the device were prepared to investigate the flow inside the SAC indoor unit.

The device is cut to two pieces for the optical access inside, and a new support was made for the free part of the CFF to ensure the operation of the CFF is proper.

This model is sealed at the outer edges and positioned between two plexiglass plates with 2 cm thickness. The plates and the device between the plates are hold by a traverse system, which also provides the movement of the device to and from the area of interest that is needed for both the calibration of the system and to make measurements on different sections of the device. Positions of the traverse, device and laser are shown in Figure 3.6.

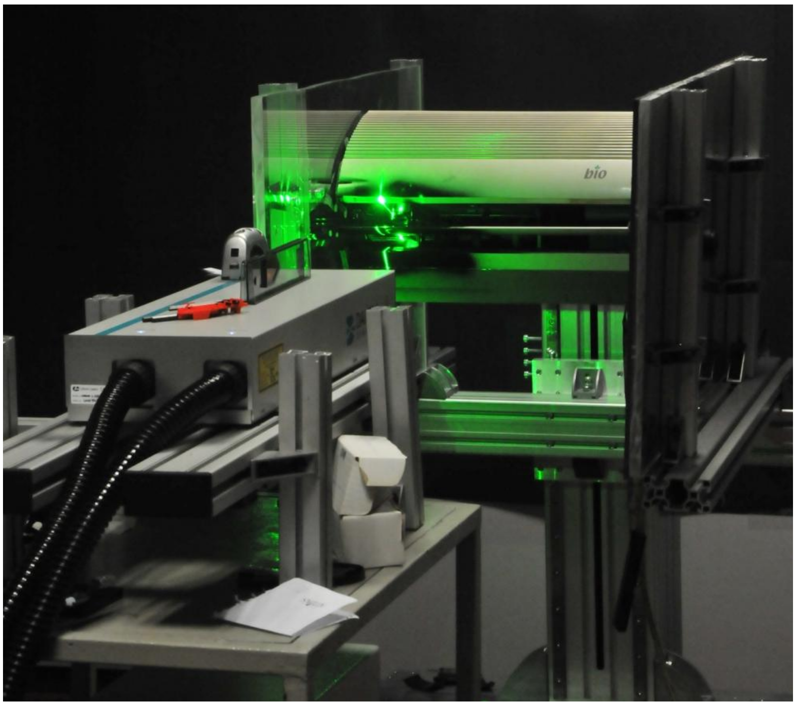

Figure 3.6 Positions of the traverse, device and laser.

Two different sections of the device were examined in this part of the thesis. One of them is in a similar position to the previous study shown in Figure 3.7 (a) but including the area around the airfoil which is used for directing the flow at the outlet and the area between the CFF and outlet sections (Figure 3.7 (b)). The rear wall and bottom part of the vortex wall are also included in this section which are very important for CFF performance. Besides, the pre-investigated area of the outlet section is also covered in the experiments which make the comparison of the new result with the previous ones possible.

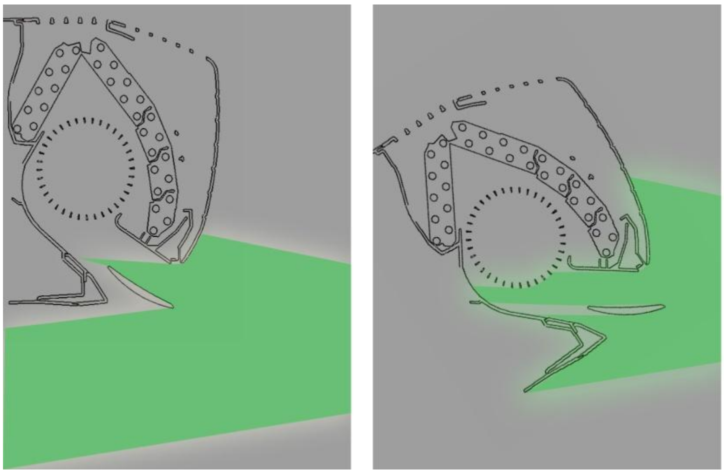

(a) (b)

Figure 3.7 (a) Light sheet position and orientation of the device for the measurements at the outlet of the device, (b) Light sheet position and orientation of the device for investigating the outflow section.

Panoramic PIV technique was used for visualizing a wider area at the outflow section. The technique is based on two cameras looking at the light sheet perpendicularly and positioned parallel to each other for taking the images of different sections simultaneously (Figure 3.8). Images taken by the cameras are stitched to visualize a wider area, without losing the better particle view advantage of a close up shot.

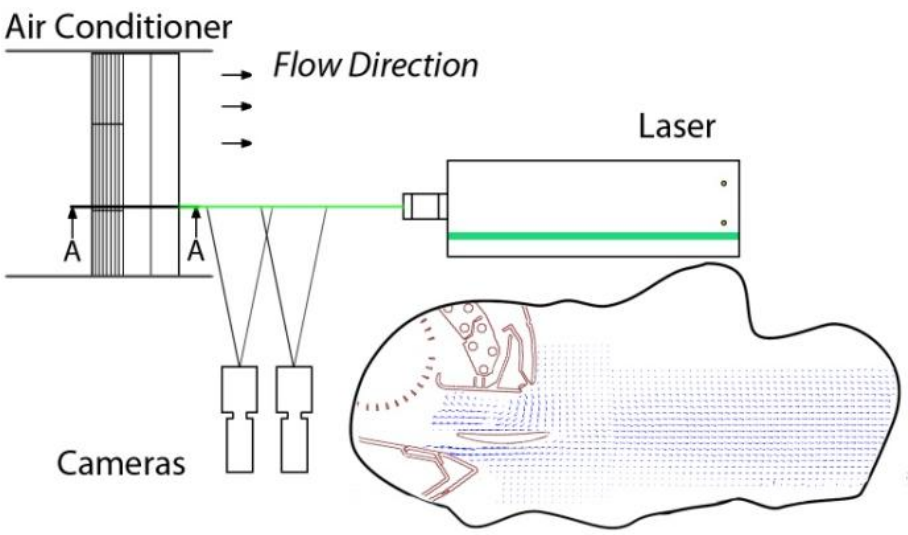

Figure 3.8 The positions of the components for panoramic PIV setup.

3.2 Temperature Measurements

Every object emits electromagnetic radiation at the infrared part of the electromagnetic spectrum (1-1000 μm) when they are at a higher temperature than the absolute zero (-273 °C). This energy is generally emitted from about 2.5×10^{-5} mm of the object surface and is not in the visible band (Meola & Carlomagno, 2004). Infrared thermography is a non-contact, non-intrusive technique, which transforms the thermal energy emitted from the objects into advisable image. In fact a sensor produces an electronic signal depending on the wave length of the oncoming electromagnetic radiation in the infrared bandwidth, which is than transformed to a visible image with each energy level presented by a color. This feature has a great potential to be applied in many fields.

3.2.1 Meshed Infrared Thermography (MIT)

The MIT method is based on the measurement screen technique (details given in the introduction part); however the measurement screen is replaced with a measurement mesh so that the disturbing effects on the flow, the thermal interaction between measurement mesh and the surrounding walls, and the effect of the conduction inside the measurement instrument are reduced by using a distinct measurement structure. In addition, unlike the probe methods, many measurement points could be established easily at the investigation area.

3.2.1.1 Components of the MIT

The measurement mesh is formed by the measurement points (dull black painted metal spheres were used) which are positioned periodically on the carriers (pieces of ropes) that are tightly fixed on a frame (Figure 3.9). The measurement points should be as small as possible for not disturbing the flow and to have a small heat capacity for having a better response time, however at the same time they should be as big as possible to be realized by the infrared camera. They could have any shape but the material should have a thermal diffusivity as big as possible for improving their response time. The distance between the particles could be changed for increasing the spatial resolution of the measurements; however, there should be enough gap between the particles for not affecting the flow and the interaction between the particles should be controlled.

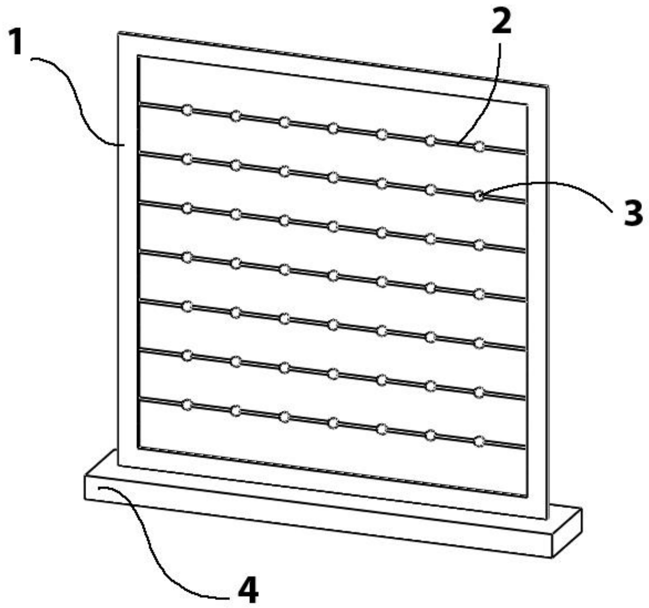

Figure 3.9 Measurement mesh; 1- Frame, 2- Carriers, 3- Measurement points, 4- Holder.

The carriers should be thin and should have low thermal conductivity for decreasing the heat conduction between the particles through the carriers. The distance between the carriers could be changed for increasing the spatial resolution of the measurements, depending on the flow conditions. The frame should be as thin as possible (especially the leading edge side) and should be robust enough against the vibration problems. The shape and the dimensions of the frame could be anything as long as the accuracy of the temperature measurement is enough for the desired application. The measurement mesh is positioned, aligned and translated inside the investigation region with a holder. Although the frame, carriers and measurement points may have some local effects on the flow, as long as the carriers and frame are thin and measurement points are small both in dimension and number, their effects on the flow are negligible.

The measurement mesh is placed into the flow where the temperature distribution is wanted to be known and the infrared camera is placed perpendicular to the measurement mesh to capture the infrared images. The infrared camera used in this study has 320x240 pixels of resolution, is sensitive to infrared radiation between 7-13.5 μm wavelengths and has an accuracy of ±50mK at 30 °C. The distance between the camera and the measurement mesh should be optimized between having enough pixels on the measurement points and including all the investigation area inside the captured images. Theoretically one pixel for every measurement point is enough for determining the temperature at that point, but more pixels would increase the accuracy and reliability of the measurements.

3.2.1.2 Theoretical Consideration

The temperature distribution on the investigated plane is found by assuming that the temperatures of the measurement points are equal to the air temperature at that point. Therefore, the change of the temperature of the measurement points with respect to time is important to verify this assumption. The time delay of the heating process of the measurement points should be considered to obtain more accurate results. Therefore the time needed for the points to reach the free stream temperature should be calculated before the experiments.

Assuming a free sphere suspending in the flow the average Nusselt number ($\overline{Nu}_D$) for the sphere is calculated as (Incropera & DeWitt, 1996);

$$\overline{Nu}_D = 2 + \left(0.4Re_D^{\frac{1}{2}} + 0.06Re_D^{\frac{2}{3}}\right)Pr^{0.4}\left(\frac{\mu}{\mu_s}\right)^{\frac{1}{4}} \qquad 3.1$$

$$\begin{bmatrix} 0.71 < Pr < 380 \\ 3.5 < Re_D < 7.6 \times 10^4 \\ 1.0 < \left(\frac{\mu}{\mu_s}\right) < 3.2 \end{bmatrix}$$

where Re_D is the Reynold's number, Pr is the Prandtl number, and μ is the dynamic viscosity of air. Re_D can be calculated from;

$$Re_D = \frac{VD}{\nu} \qquad 3.2$$

where V is the free stream velocity, D is the diameter of the sphere and ν is the kinematic viscosity of the fluid. Once the $\overline{Nu}_D$ and the thermal conductivity of the sphere (k) is known, the average convection coefficient ($\bar{h}$) is calculated from;

$$\bar{h} = \frac{\overline{Nu}_D k}{D} \qquad 3.3$$

Lumped capacitance method can be used to estimate the time required (t) for the sphere to reach some temperature T if the following condition for the Biot number (Bi) is satisfied;

$$Bi = \frac{\bar{h}\, L_c}{k} < 0.1 \qquad 3.4$$

Then the time required for the sphere to reach some temperature T can be calculated as;

$$t = \frac{\rho C_P D}{6\bar{h}} ln \frac{T_i - T_\infty}{T - T_\infty} \qquad 3.5$$

where ρ, C_P are the density and specific heat of the fluid, respectively. All the properties in Equations 3.1 - 3.5 (except μ_s) are evaluated at free stream temperature (T_∞), whereas μ_s is evaluated at the initial surface temperature (T_i). As seen from the Equation 3.5, the difference between the solid and fluid temperatures must decay exponentially to zero as t approaches infinity. However, the time for the sphere to reach a temperature as close as the fluid temperature can still be calculated.

3.2.1.3 Image Processing

One or more images could be captured for a steady state measurement. However, for determining the steady state temperature distribution, more than one image should be taken to have more reliable results. Once the infrared images are taken, the temperature at any point on the image could be determined by eye or by using the computer program of the thermal camera. However, such a determination is time consuming and strongly depends on the skills of the user. Therefore the obtained infrared images were processed by a developed computer program in which the spheres are distinguished, and their temperatures are determined.

A binary mask is produced for the infrared images, which has the value one for the pixels on the spheres and zero for all the other pixels. Masks having 5 pixels, 13 pixels and 21 pixels per measurement point were prepared for the validation study and their basic elements are given in Figure 3.10. The mask is multiplied by the infrared image to distinguish all the pixels from the image but the measurement points. What is left after the multiplication is an image, which has the temperature values on the point that has the one value for the corresponding point on the mask and zeros elsewhere. Therefore, the shape and the dimension of the points on the mask have an important role on the determination of the temperature from the infrared image. Besides, even small vibrations of the carriers on the measurement mesh produce some displacement for the measurement points on the captured infrared images. This displacement sometimes is the thin line for a pixel to have the temperature of the measurement point or the backside object. Therefore, the mask should be adaptable on every infrared image. A sample infrared image and corresponding binary mask is given in Figure 3.11.

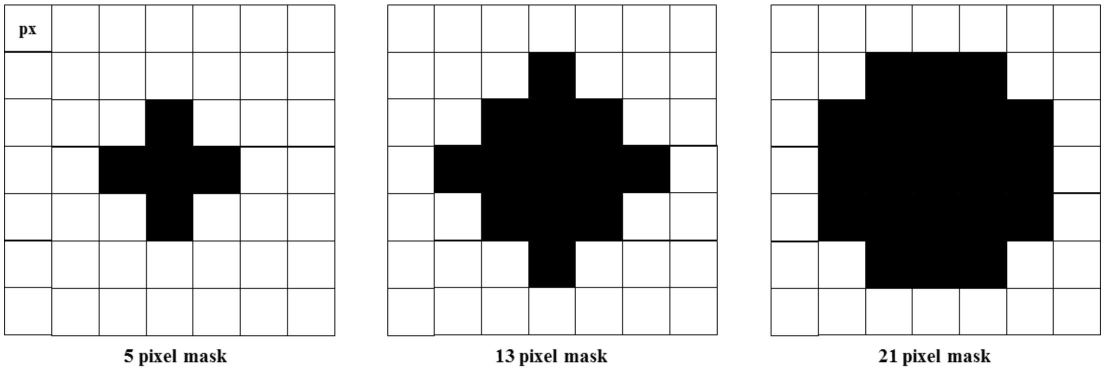

Figure 3.10 Different masks used for the validation study

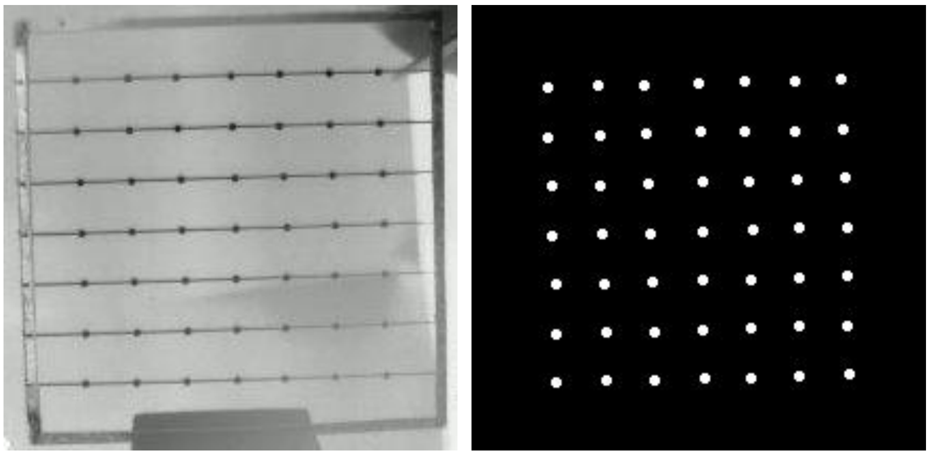

Figure 3.11 A sample infrared image and the mask.

Mean and maximum/minimum algorithms were used to adapt the mask on the consecutive images. The mean of the temperature values of the pixels is taken as the temperature at the measurement point for the mean algorithm, whereas the maximum or minimum of the temperature values of the pixels is taken as the temperature at that point for the maximum or minimum algorithms, respectively. The choice for the maximum or minimum algorithm depends on the air temperature and the backside object's temperature. If the air temperature at the investigation area is higher than the backside object the maximum temperature is used and vice versa. The mean algorithm is useful when the number of the pixels for a point is big, and if the displacement of the measurement points is small between the consecutive images. If the number of the pixels for a point is small, the difference of the temperature of even one pixel would cause big differences of the measured temperature at that point. Therefore, when the number of the pixels for a point is small and/or vibration of the measurement points is relatively more, maximum or minimum algorithms are more useful.

3.2.1.4 Validation Study

A blower which produces an air jet at 60 °C with 10 m/s velocity at its outlet was used for the validation of the method together with 10 K-type thermocouples. Thermocouples were tested inside a water-bath at three different temperatures (12°C, 50 °C and 70 °C) before the validation study and it is seen that the absolute difference from the bath temperature is between 0.1 °C and 0.5 °C whereas the standard deviation of the measured temperatures from the different thermocouples is 0.15 °C. The three point calibration curve for the thermocouples is given in Figure 3.12. The temperature data from the thermocouples are calibrated by using this calibration curve.

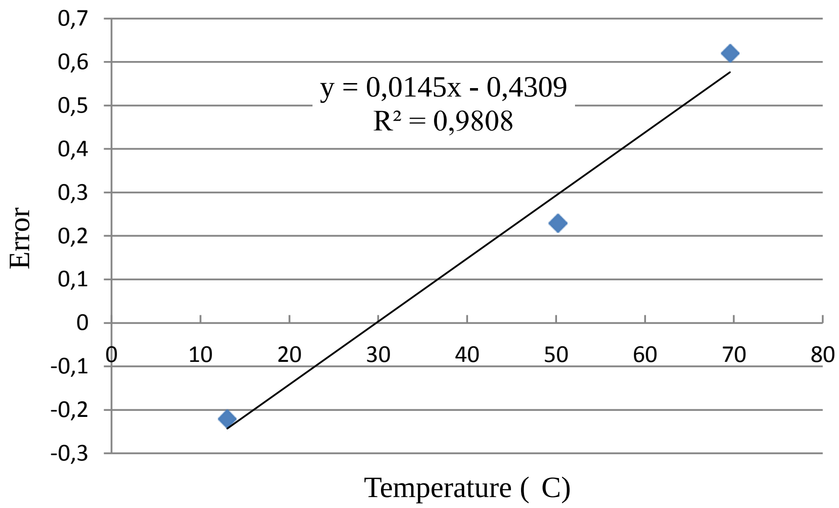

Figure 3.12 Calibration curve for the thermocouples

The measurement mesh was placed into the flow parallel to the axis of the jet having the jet flow through its diagonal. The dimensions of the frame were 210x210 mm and the horizontal and vertical distance between the spheres was both 25 mm for forming a 7x7 nodes measurement mesh (Figure 3.13). The diameter of the spheres was 4 mm. The distance between the top left corner of the measurement mesh and the outlet of the blower was 10 cm. 10 K-type thermocouples were placed to the neighborhood of the 10 randomly selected spheres for comparison and their positions are also given in Figure 3.13.

The blower was turned on after the measurement mesh had been put in front of it and measurements had been started. This part of the experiment showed that the temperatures of the thermocouples are the same before the experiment. 65 infrared images were captured during the validation study for 1200 seconds, including the startup and steady state durations and cooling period of the measurement points after the blower was turned off. Steady state part of the experiments was long enough to examine the robustness of the MIT method (660 s). The data logger's measurement frequency was 1 s all through the experiments. Infrared images were taken frequently for the heating and cooling durations and less frequent for the steady state part of the experiment.

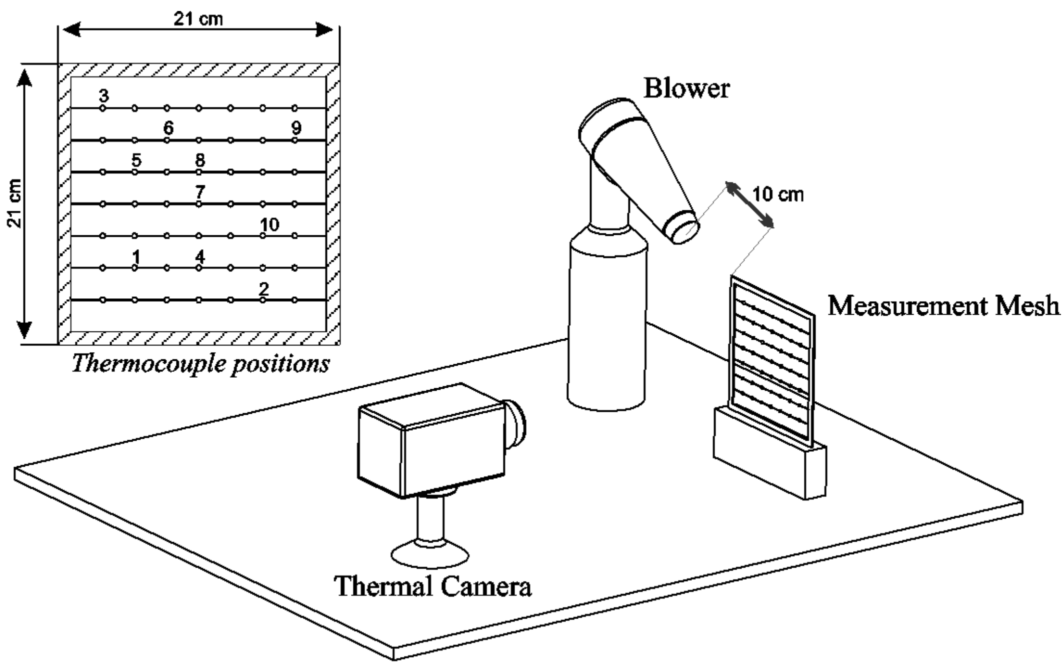

Figure 3.13 The validation setup; placement of the measurement equipment and the positions of the thermocouples.

Different mask types and algorithms were tried for the MIT measurements and a sample for comparison of the results with the thermocouple data (TC10) for the measurement point 10 (indicated by MIT10) is given in Figure 3.14. For the steady state part, the mean algorithm for the 5 pixels mask (MIT10-5m) has the biggest deviation (2.7 °C) from the thermocouple data whereas the deviation decreases for the maximum algorithms. Besides, the deviation also decreases as the pixel number of the mask per measurement point increases. The differences from the thermocouple data for the mean temperatures of the steady state part of the data is 2.07, 1.88 and 1.7 °C for the 5 pixels (MIT10-5), 13 pixels (MIT10-13) and 21 pixels (MIT10-21) maximum algorithms, respectively. Therefore, the maximum algorithm for the 21 pixels per measurement point was used for the determination of the air temperatures.

The response of the MIT method with different masks and algorithms are consistent with the thermocouple data for the heating and the cooling periods. However, the time delays of the heating and the cooling processes for the MIT method are apparent. The time delay for the heating part contains the time for the blower to reach the steady state conditions which takes 45 seconds together with the time needed for the heating of the measurement points. The time that the blower was turned on and reached its steady state flow are indicated in Figure 3.14.

Determination of the starting point of the steady state regime for the MIT method is important for the interpreting the results of the measurements. In addition, the duration that the measurement mesh must stay in the investigation area is important for the steady state measurements. Using the calculation procedure given in Part 3.2.1.2, the heating behavior of a silver sphere with a diameter of 4mm is calculated for different free stream temperatures for a free stream velocity of V=10 m/s, and the result is given in Figure 3.15. The time required for the sphere to reach the temperature 1 °C below the free stream temperature is represented by a line (-1 °C) in Figure 3.15. As the free stream temperature decreases the time required for the sphere to reach the temperature 1 °C below the free stream temperature is also decreases. Therefore, the dominant measurement point for the determination of the steady state regime is the one with the stream that has the maximum temperature when the velocity of the fluid around the measurement point is taken as constant. In addition, the MIT method gives reasonable results even though the difference between the free stream temperature and the initial temperature of the sphere is small.

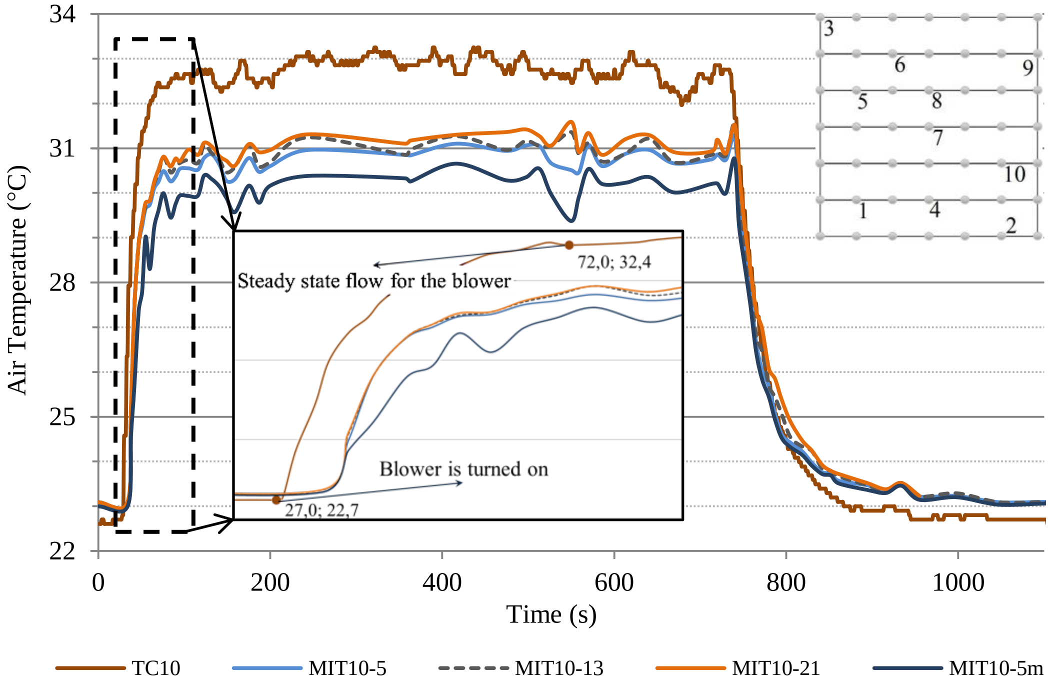

Figure 3.14 Different mask types' and algorithms' response to the temperature change of the measurement points

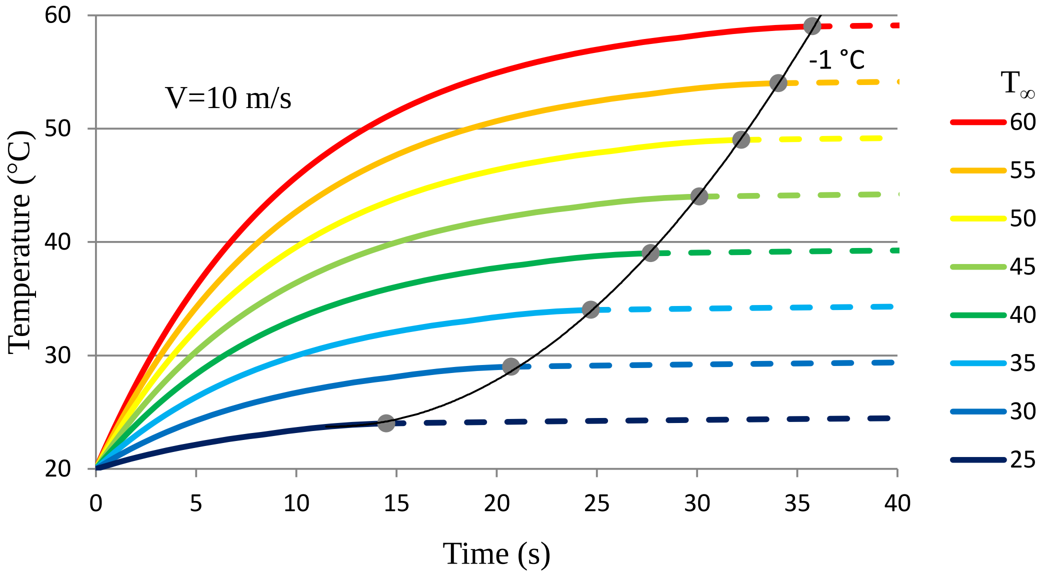

Figure 3.15 The heating behavior of sphere for different free stream temperatures (V=10m/s)

The heating behavior of a sphere suspending in the flow with different free stream velocities is given in Figure 3.16. The dominant measurement point for the determination of the steady state regime is the one with the stream that has the minimum velocity when the temperature of the fluid around the measurement point is taken as constant. It is seen form the Figure 3.15 and Figure 3.16 that, for the determination of the steady state temperature distribution inside air using the MIT method, repetitive measurements may be needed for accurate results. There should be enough time between the placement of the measurement mesh inside the investigation area and the starting time of the measurements. However, different shapes, dimensions, and materials could be used for optimizing the response time of the MIT method. Moreover, by using the proper measurement points, time dependent temperature distribution inside the air may be determined by the MIT method.

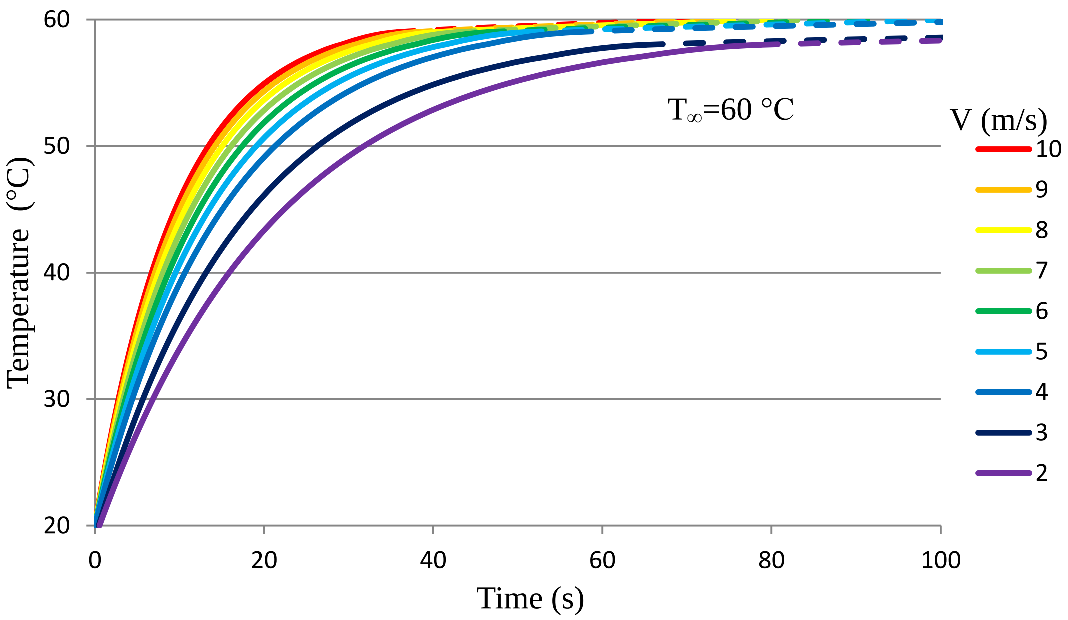

Figure 3.16 The heating behavior of sphere for different free stream velocities (T_∞=60 °C)

The diameter of the measurement points is an important factor for the time response and the visibility of the spheres accurately. The diameter should be reduced for decreasing the thermal mass and therefore increase the time response of the method. However, this will reduce the visibility of the measurement points and pixel to point ratio, which is described as the number of the pixels per measurement point, depending on the distance between the measurement plane and the infrared camera, and the size of the investigation area. In addition, hollow spheres may be used as measurement points which will reduce the thermal mass and increase the time response of the MIT method without reducing the pixel to point ratio of the images. The time response of the MIT method for the spherical measurement points with different diameters (4, 2 and 1 mm) or the thickness of the shell for the hollow spheres with 4 mm diameter (0.5, and 0.2 mm) are given in Figure 3.17 for a free stream temperature of 60 °C and free stream velocity of 5 m/s. The equivalent density of the hollow spheres (ρ_{eq}) was calculated as;

$$\rho_{eq} = \frac{m_{hollow\ sphere}}{V_{sphere}} \qquad 3.6$$

for the theoretical calculations, where $m_{hollow\ sphere}$ is the mass of the hollow sphere and V_{sphere} is the volume of the hollow sphere. As seen from the Figure 3.17 the time needed for the spheres to reach 0.5 °C below the free stream temperature gradually decreases as the diameter of the spherical measurement point decreases. The decrease for the hollow sphere is essentially bigger than the diameter change where the ratio of the time needed for the solid sphere (D=4 mm) to reach the 0.5 °C below the free stream temperature to that of a hollow sphere with a 0.2 mm shell thickness is 7.

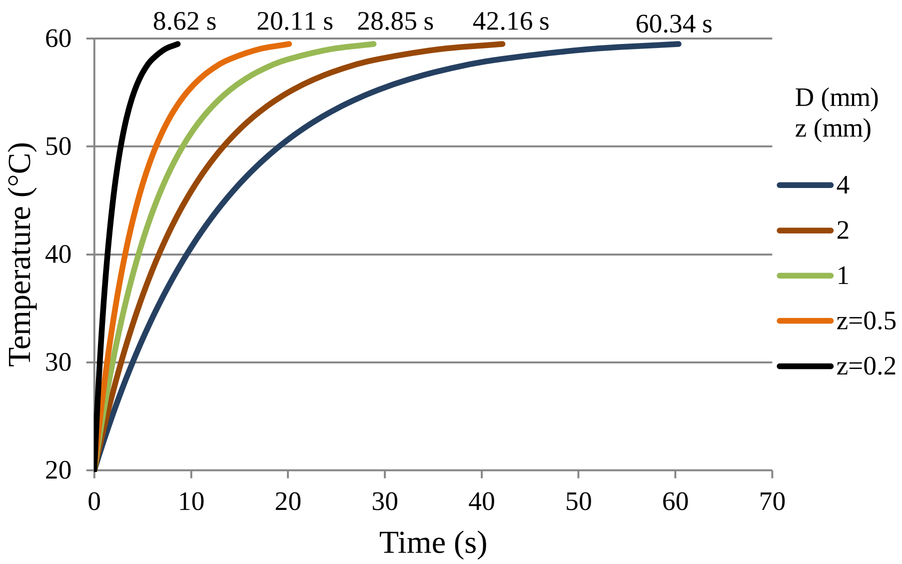

Figure 3.17 Time response of the spherical measurement points with different diameters and shell thicknesses for the hollow spheres.

The temperature measurements by MIT and thermocouples (TC) at different points on the measurement mesh for the validation study is given in Figure 3.18. At this time scale, the time response of the MIT method does not seem to change for different temperatures such that; after the blower had been turned on, temperatures suddenly increased at all the measurement points, and then started to oscillate around the steady state temperature until the blower was turned off. In addition, determination of the steady state part of the measurements form the chart is relatively simpler, because of the relatively long duration of the measurements. However, for the sake of consistency, the time required for the spheres to reach the corresponding steady state free stream temperatures (25.3 °C, 40.6 °C, 37.4 °C, and 32.8 °C for the points 1, 3, 6, and 10, respectively) were calculated using the formulation given in Part 3.2.1.2. The physical properties of the air were taken from the literature (Incropera & DeWitt, 1996) at the temperature values of the each flow condition. The free stream velocities for the measurement points were assumed as 8.15 m/s, 5.93 m/s, 2.11 m/s, and 0.56 m/s for the points 3 and 6, 10, and 1, respectively. These velocity values were obtained from the hot wire anemometer measurements at the vicinity of the corresponding measurement points. The comparison of the theoretical calculation and the results of the MIT method for the measurement points 1, 3, 6, and 10 are given in Figure 3.19.

Depending on the theoretical studies results, the critical measurement point for the determination of the onset of the steady state regime is the Point 1, because it has the lowest free stream velocity of all (Figure 3.16). The time needed for the Point 1 could be as big as 80 seconds depending on the free stream temperature as seen from Figure 3.16. In addition, although the results of the theoretical calculations and the measurement results do not perfectly fit, it is seen from the Figure 3.19 that the theoretical and experimental curves for the Point 1 intersect at around 100 seconds. Therefore, the time for the onset of the assumed to be at least 100 seconds and 25 infrared images were taken as the steady state part of the flow and they were processed to obtain instantaneous temperatures on comparison points.

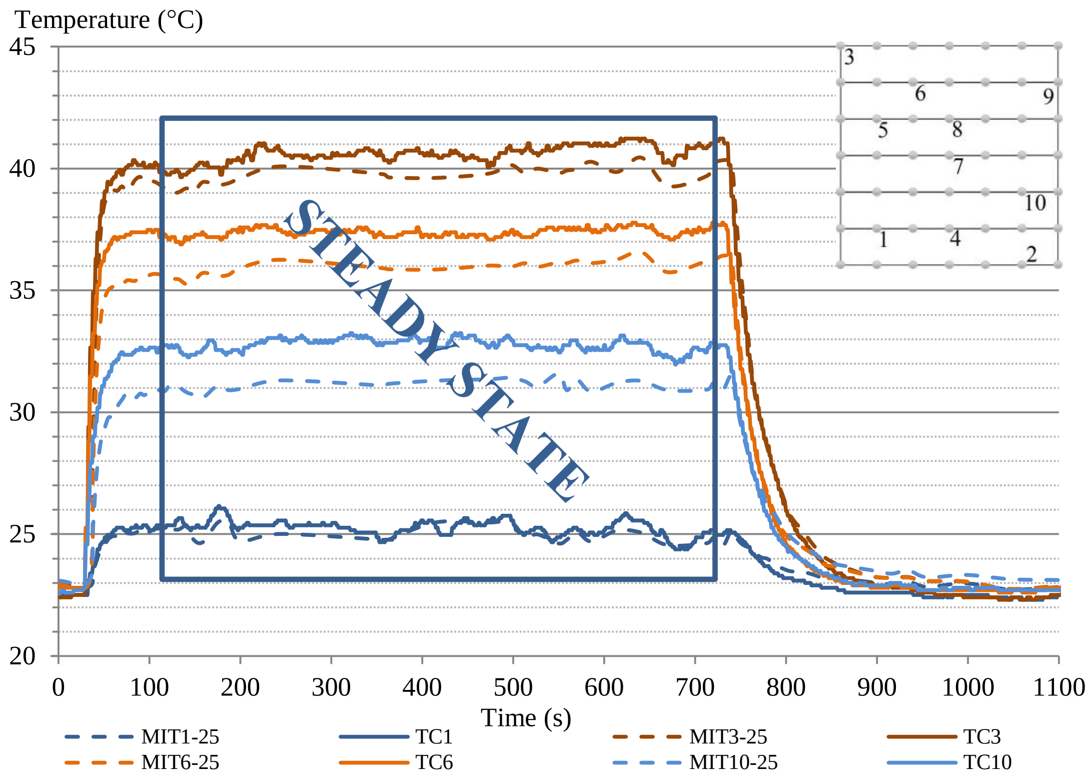

Figure 3.18 The temperature measurements by MIT and thermocouples (TC) at different points on the measurement mesh.

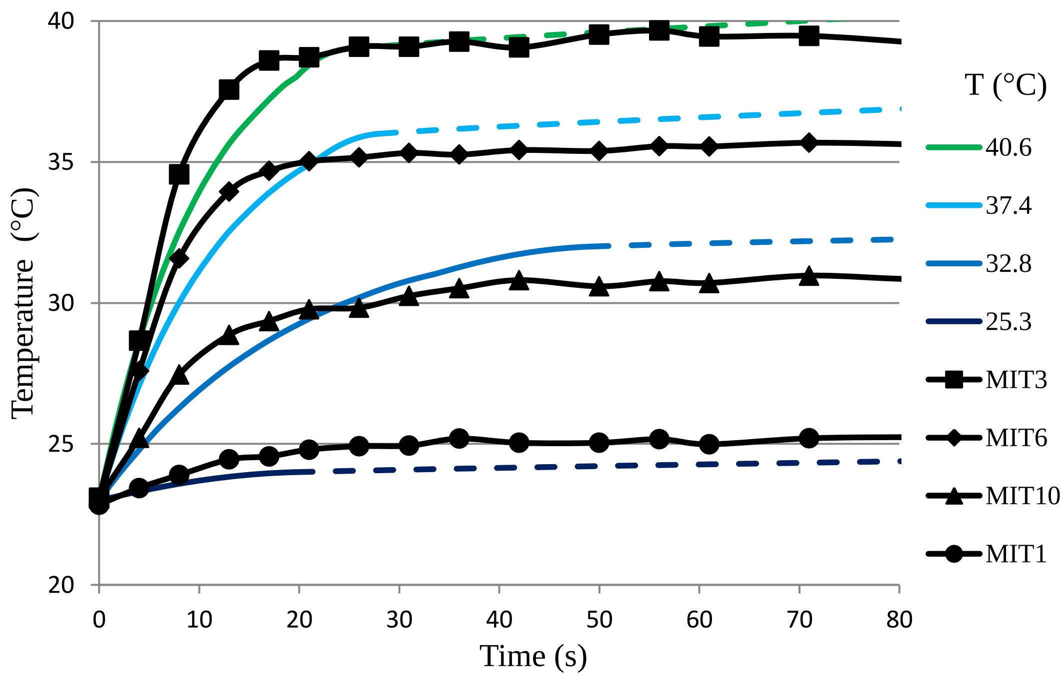

Figure 3.19 Comparison of the theoretical calculation and the results of the MIT method

The steady state thermal behavior of the system was analyzed for determining the difference between the results of the MIT measurements and thermocouples (Figure 3.18). The absolute difference between the averages of these instantaneous temperature values on individual points and the averages of the corresponding thermocouple data is between 0.24 and 2.73 °C. The average and the standard deviation of the absolute differences for all the points are 1.4 °C and 0.64 °C (Table 3.2), respectively. The steady state temperature measurements by the MIT and thermocouples at the points 1, 3, 6, and 10 on the measurement mesh and ambient temperature (T_a) are given in Figure 3.20.

Table 3.2 Steady state average temperatures for the all measurement points and the absolute differences.

	1	2	3	4	5	6	7	8	9	10
MIT	25,02	29,38	39,66	29,01	32,71	35,9	32,77	32,76	32,83	31,09
TC	25,26	32,12	40,56	30,64	34,28	37,38	34,38	34,27	32,18	32,76
Difference	0,24	2,73	0,91	1,60	1,57	1,48	1,61	1,45	0,71	1,67

Standard deviation of the difference = 0.64

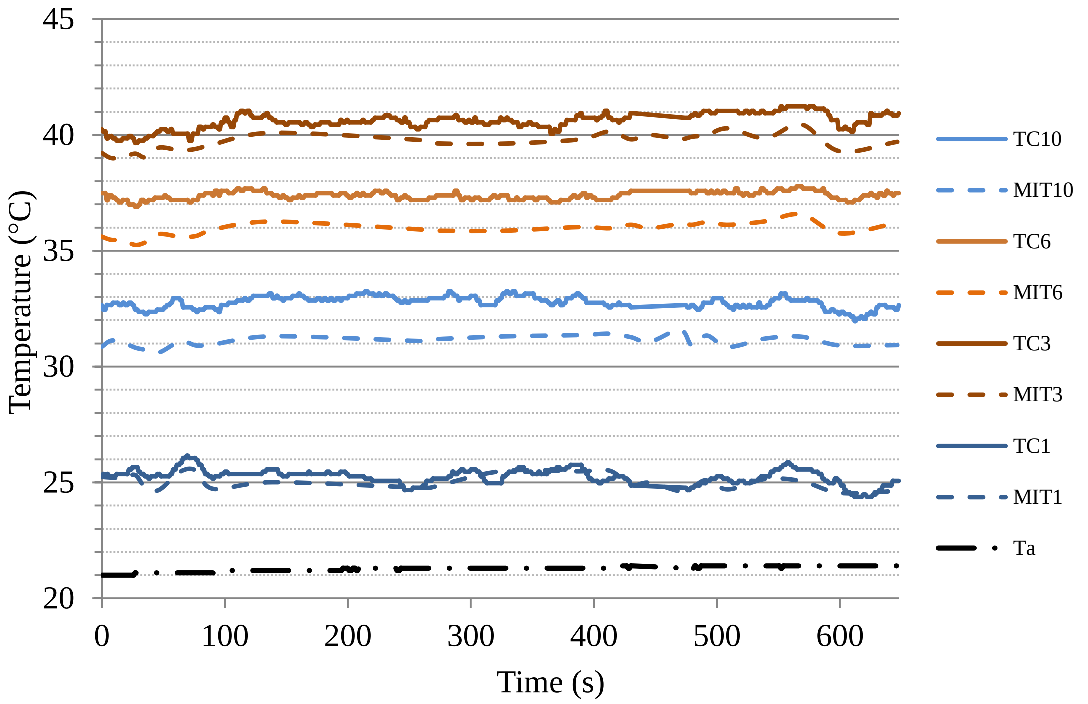

Figure 3.20 The steady state temperature measurements by MIT and thermocouples (TC) at different points on the measurement mesh.

The overall reliability of the MIT method was verified by a linear regression analysis. Every MIT measurement from all the comparison points was matched with the corresponding thermocouple data to calculate R-squared value of a linear trend line. The linear regressions between the MIT and the corresponding thermocouple data are given in Figures Figure 3.21, Figure 3.22, Figure 3.23, and Figure 3.24 for the heating (R^2=0.9031), steady state (R^2=0.9447), cooling periods (R^2=0.952) and whole measurement data (R^2=0.9481), respectively. All the R-squared values are higher than 0.9, which implies that there is an acceptable correlation between the MIT and thermocouple data and the MIT method is adequate for visualizing the temperature distribution at different flow sections. However, it should be noted that the correlation is not as good as the others for the heating period, where the fastest change of temperatures occurs in the investigated area. The reasons for the better values of the R-squared for the steady state and cooling conditions are; the unchanged temperature field and the relatively slower temperature changes during the heat transfer by natural convection. Moreover, the cooling period visualizes the cooling behavior of the measurement points more than the temperature distribution inside the air. After the validation of the method, the measurement mesh is placed in front of the SAC indoor unit to determine the temperature distributions at the planes that are given in Figure 3.4.

The temperature distribution at the investigated area for the validation study is visualized for different times through the heating, steady state and cooling periods in Figure 3.25. Although the temperature distributions for the heating and cooling periods include the time delay of the system and do not visualize the real situation correctly, these results give and idea of how can the MIT methods be used for visualization.

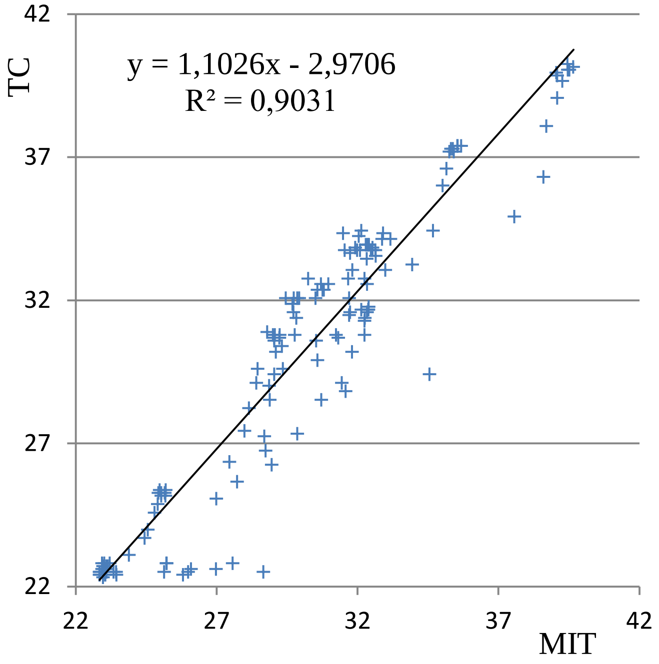

Figure 3.21 Linear regression fitting between the MIT and thermocouple data for the heating period.

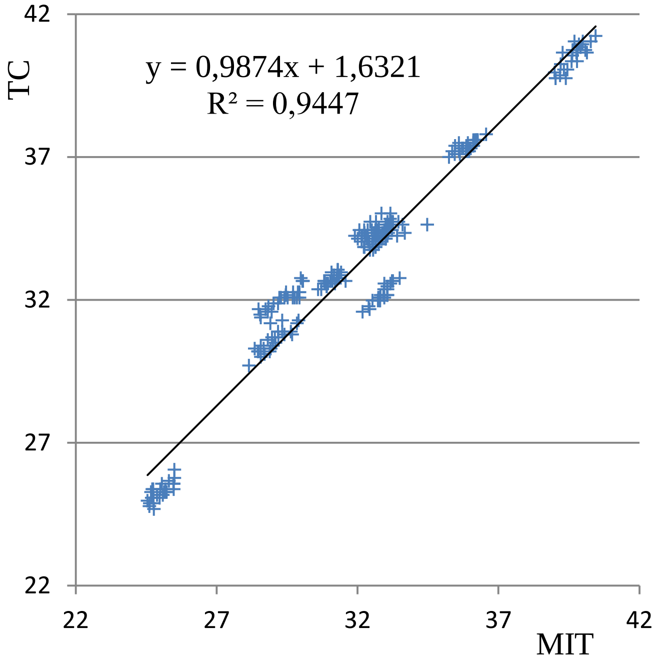

Figure 3.22 Linear regression fitting between the MIT and thermocouple data for the steady period.

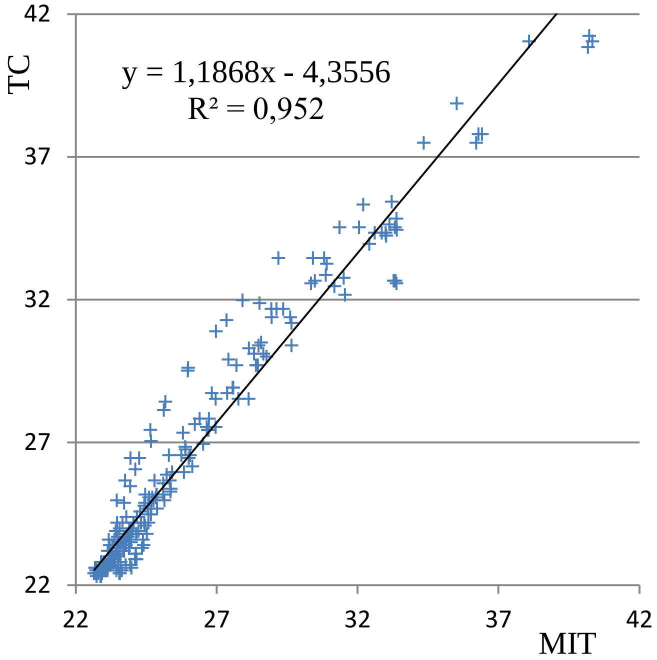

Figure 3.23 Linear regression fitting between the MIT and thermocouple data for the cooling period

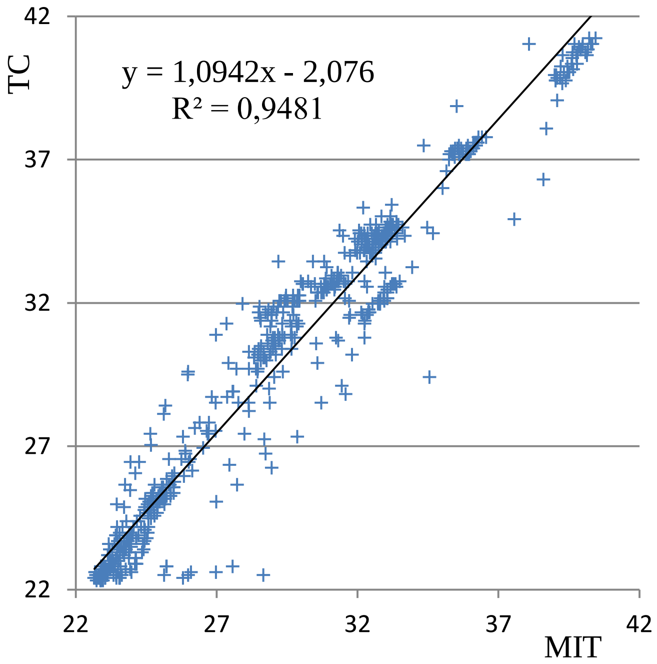

Figure 3.24 Linear regression fitting between the MIT and thermocouple data for the whole measurement data

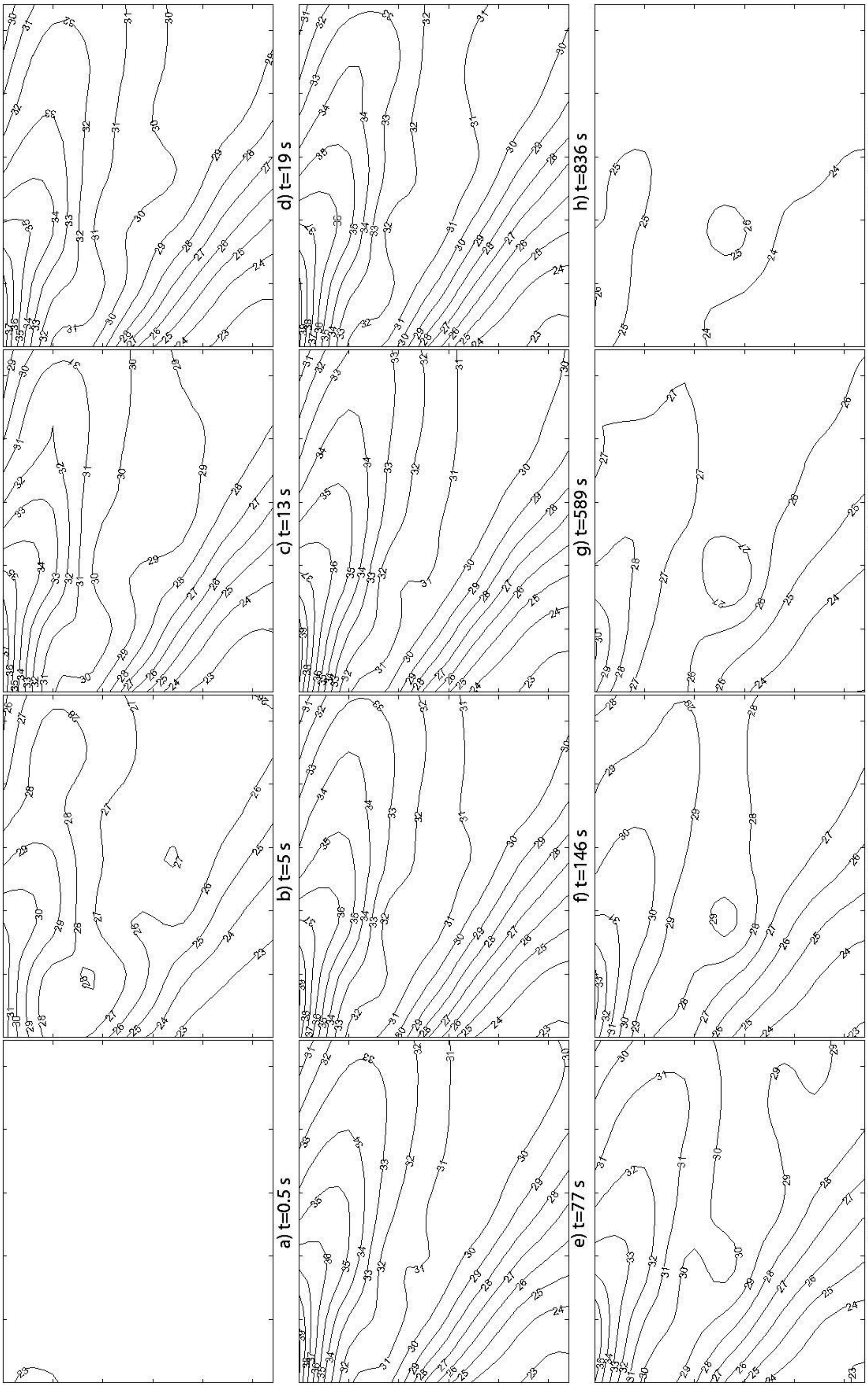

Figure 3.25 Temperature distribution at the investigation area at different times, a-d heating, e-h steady state, i-l cooling

CHAPTER FOUR
OUTFLOW CHARACTERIZATION OF THE SAC INDOOR UNITS

4.1 Introduction

Although CFFs are known to be producing a two dimensional planar jet flow, their high dependency on surrounding objects such as vortex wall, rear wall, device edges etc. results fluctuations inside the flow and changes the flow conditions. As one of the blades of the CFF passes by the vortex wall, small eddies are formed instantaneously until the following blade reaches and suddenly incoming blade forms new eddies which affect the previous ones. Result of consecutive formation of eddies is thought to be the eccentric vortex which dominates the whole stream, being the driving mechanism of the CFF flow. Besides, residual turbulences continuously reach the outflow section forming a fluctuating flow and causing vibration and noise problems. In order to minimize the fluctuations at the outflow, inner design and properties of both CFF and the casing should be optimized. Flow visualization methods are very useful for identifying these deviations from the ideal conditions.

Experiments were made on the outflow section of the device to have an idea on the flow conditions. Although it is important to investigate the inner flow for improving the performance, outflow measurements were useful for both having an idea for the flow characteristics and defects. Three different models were investigated for the outflow characterization; old design (Model 1) which has a relatively low performance, a new and better design (Model 2), and a commercial model taken from the market (Model 3) which is known to have high performance. In this part of the thesis; the results of the velocity measurements at the outlet of the different SAC indoor units with a straight CFF are given for determining the outflow characteristics. Also the results of the temperature distribution measurements were given for further investigation of the outflow of the device.

4.2 Outflow Measurements

20 different measurement planes were defined for the Model 1 for visualizing the outflow of the device. Some of these planes were identified before the measurements had been started, and some (0, 10-1, 10-2, 16, and 17) were identified because of the demand for the more detailed investigation at that part of the device. The measurement planes at the outlet of the device for the Model 1 are given in Figure 4.1.

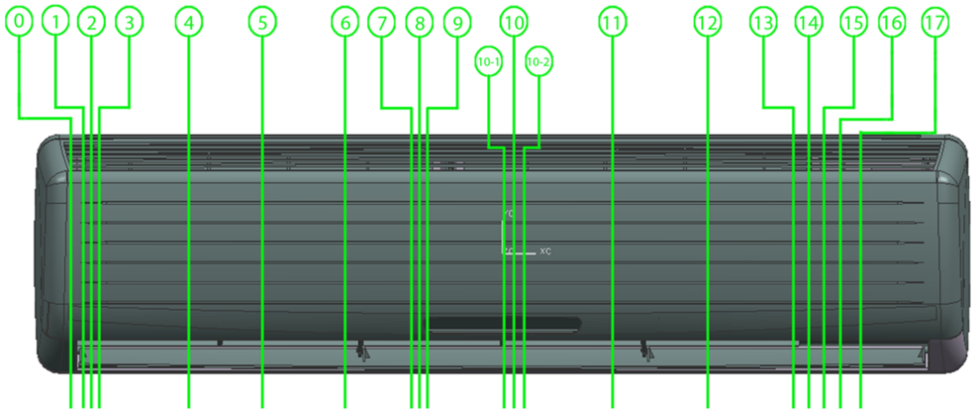

Figure 4.1 Measurement planes at the outlet of the device for the Model 1.

Plane 0 is out of the outflow of the SAC indoor unit, because of the necessity for the determination of the flow boundaries. Planes 1, 2 and 3 are situated closer to each other and to the right edge of the device to investigate the effects of the device edges on the flow. Planes 4-6 as well as the Planes 10-12 are separate because of the expectation of the minor changes for the flow structure, and Planes 7-9 are selected very close to each other to investigate the near field effects of the position at the outlet section of the device at the middle section. There is another tightly selected plane group at the left edge of the device (Planes 13-17) which are important for the determination of the edge characteristics of the planar jet. Finally, Planes 10-1 and 10-2 were investigated for revealing the unusual flow structure at the neighborhood of the Plane 10. The total width of the investigated portion of the outflow section is 906 mm and the investigated area at each of these planes is 195×150 mm. The investigated volume at the outflow section of Model 1 is given in Figure 4.2, which has the same cross section with the investigated part for the Model 2 and 3, but the width of the measurement area is different. Similarly, 14 planes were defined for Model 2 and Model 3 which is given in Figure 4.3. Although the outer shell geometries of the Models 2 and 3 are different, their outlet widths are the same. Therefore, the measurement planes are only given on the geometry of Model 2.

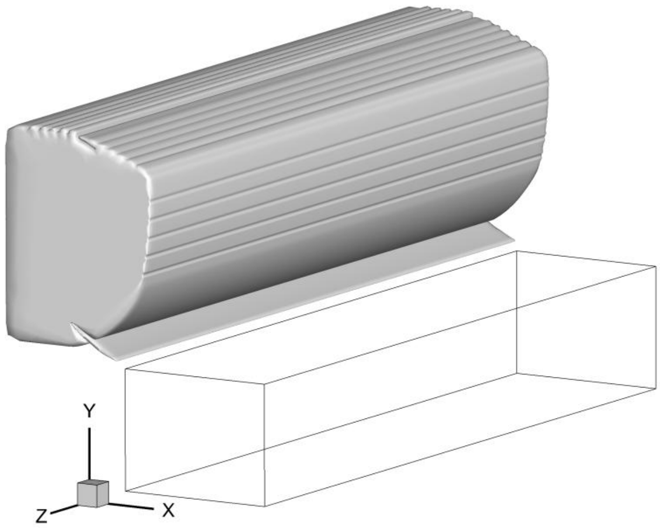

Figure 4.2 The investigated volume at the outlet of the SAC indoor unit.

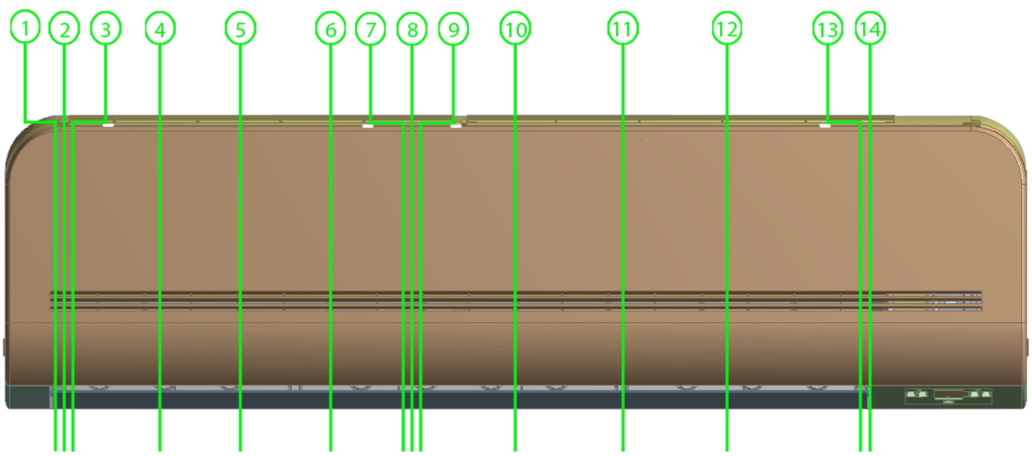

Figure 4.3 Measurement planes at the outlet of the device for the Model 2.

300 image pairs from each of the cameras were taken to obtain in-plane 3D instantaneous velocity vector fields on the selected investigation planes at the outflow section of the device for the Model 1 with straight and skewed CFFs. For the Models 2 and 3, 100 image pairs were taken for investigating their outflows. The instantaneous velocity vector fields can be used to identify the time-dependent

characteristics of the device as given in Figure 4.4 for Plane 6 for the Model 1 with skewed angle CFF. Flow is oscillating up and down on the right side of the investigation area, while eddies continuously form and disappear along the edges of the planar jet flow. More complex studies may be carried out for the detailed investigation of the formation of eddies and oscillation characteristics of the flow but the temporal resolution of the experimental setup used in this study (7 double frames per second for the cameras) is much more lower than the time scale of the CFF rotation (20 rotation per second for the maximum flow speed). Furthermore, the time scale of the formation and disappearance of the eddies is related with the blade passing frequency by the vortex wall, which is up to 700 blade passes per second. Therefore, the average velocity profiles of the instantaneous velocity vector fields were calculated to sort out the instantaneous effects and to distinguish the effects of the position through the device.

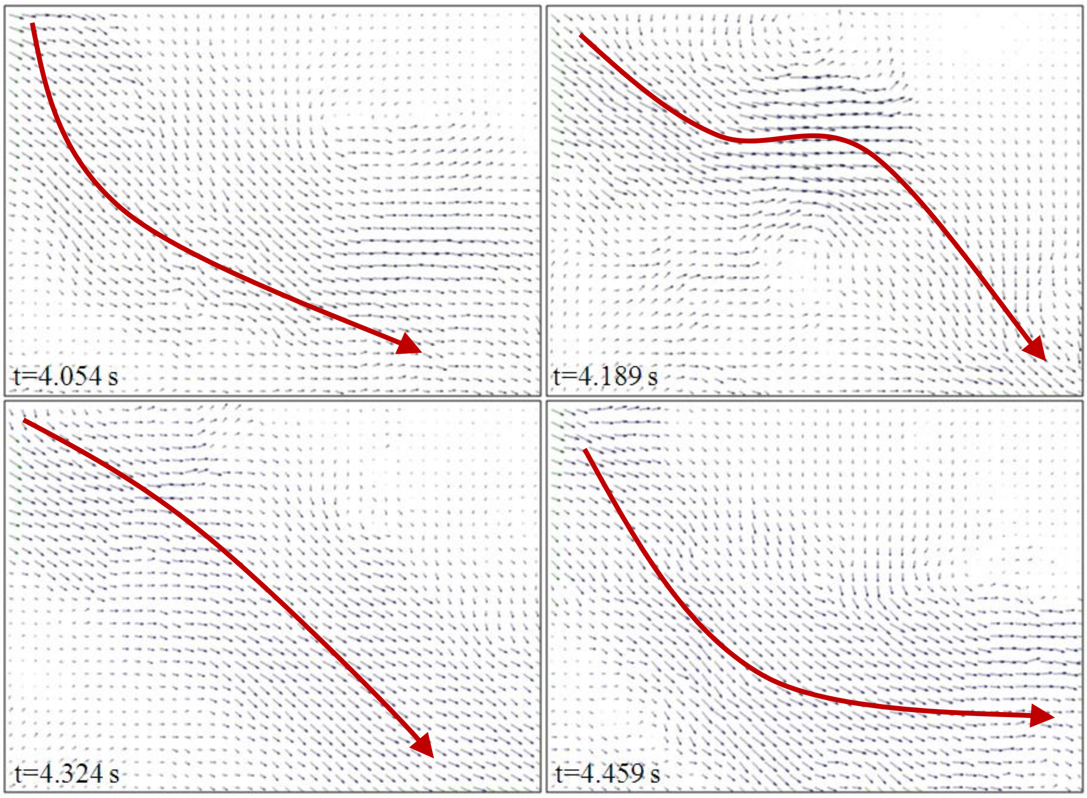

Figure 4.4 Samples of successive instantaneous vector fields.

4.2.1 Outflow of the Model 1

The flow structure for the planes on the different cross sections at the outflow of the Model 1 with a straight CFF are given in Figure 4.5 (Planes 0-8) and Figure 4.6 (Planes 9-15) by the average velocity profiles. 2D flow is shown by the vector map and the out-of-plane movement of the air is indicated by the gray-tones (black is out of the paper plane and white is into the paper plane). The planar jet flow is clearly seen on the Figure 4.5 and Figure 4.6 which is created by the large velocity difference between the conditioned and the ambient air and is characterized by a shear layer that is continuously growing downstream. This planar jet flow is passing through the diagonal of the investigated area; however the flow is not identical on every part of the device.

Plane 0 is out of the planar jet flow with the in-plane velocity components in the order of 0.1 m/s. However, the interaction between the device edges and the planar jet flow results a transverse flow at the outlet section (Region A), which is situated under the jet and the device, and shown at the left side of the investigated area in Figure 4.5. The out-of-plane velocity component in the transverse flow is up to -0.6 m/s, which shows the flow is from the surrounding air inside the test room to the down under the device. The Plane 1 was not investigated for the Model 1 with a straight CFF. The flow patterns for the Planes 2 and 3 are similar to each other, with the edge of the planar jet flow situated along the diagonal of the investigated area, and the transverse flow which was also observed for the Plane 0 existing at the left side of the investigated area. The magnitude of the in-plane velocity component is up to 2 m/s at the exit and the out-of-plane component is closer to that of the Plane 0, with slightly higher velocities at Plane 2. Movement of the surrounding air into the jet flow is indicated by the Regions B in Figure 4.5. Although it is expected that the surrounding air would move into the main stream with the effect of the spreading jet flow, there is a backflow region at the upper and lower sides of the planar jet at the edge of the device. Furthermore, there is a recirculation (Region C), just below the jet flow at the exit of the device, which is the in-plane component of the transverse flow.

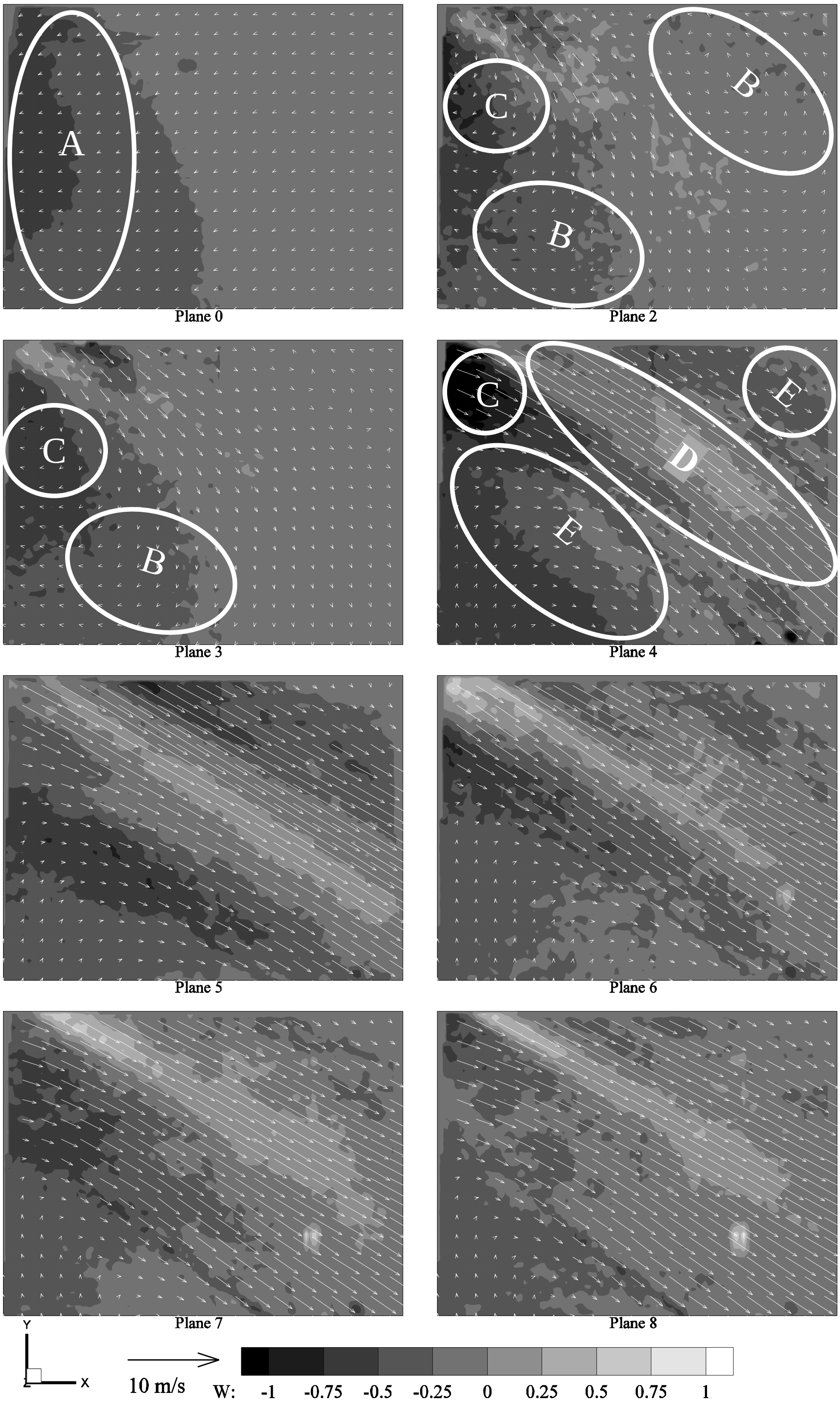

Figure 4.5 Velocity distributions for the planes on the different cross sections (Plane 0-8) at the outlet of Model 1 with a straight CFF.

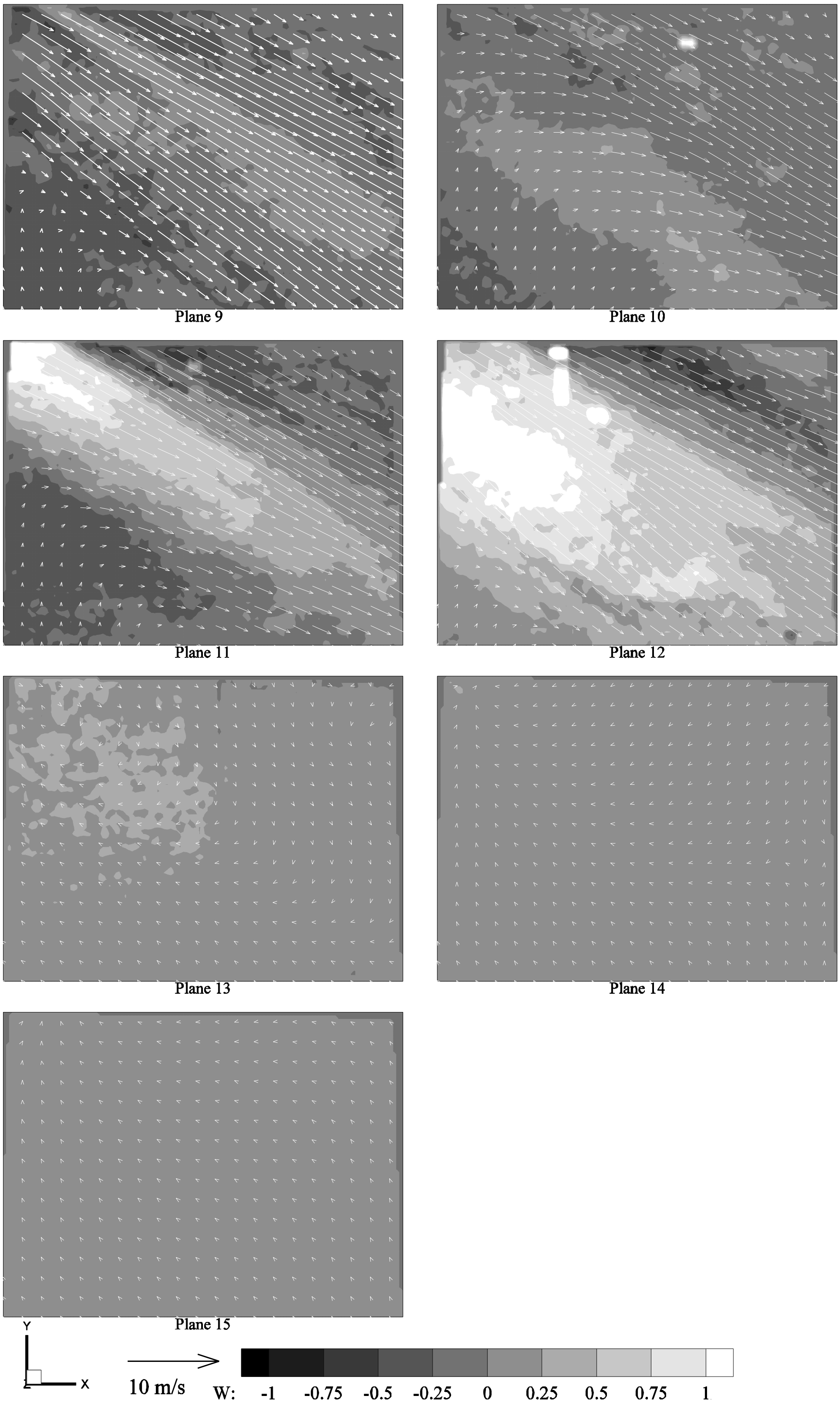

Figure 4.6 Velocity distributions for the planes on the different cross sections (Plane 9-15) at the outlet of Model 1 with a straight CFF.

The out-of-plane velocity component of the flow is small at the outlet of the device. However, as the jet flow develops into the surrounding air it starts to expand to the transverse direction so that the out-of-plane velocity increases at the middle part of the investigated area. After the sudden expansion, the rate of the expansion reduces along the major axis (the axis along the flow) of the jet flow. Both in-plane and out-of-plane velocities reduce and the direction of the out-of-plane component changes as the effect of the main stream reduces through the upper and lower parts of the planar jet flow. However, this is not true for the Region C where the out-of-plane velocities are higher than the in-plane velocities and a reversed transverse flow occurs. This reversed transverse flow is thought to be the result of the interaction between the edges of both the device and the planar jet flow. As the conditioned air comes out at the edges of the device, the planar jet flow suddenly expands to every direction and the gaps beside and under the device let the air to turn back, whereas the surrounding air moves to the middle part following the bottom edge of the device.

The planar jet flow (Region D) is clearly seen in Plane 4 in which the in-plane component of the velocity magnitude is 5 m/s at the exit. As the investigation plane moves towards the center of the device, the velocities get bigger and the edge effects disappear where the movement of the surrounding air into the main stream (Region E) takes the place of the recirculation and backflow zones. The transverse flow does not change at the lower left part of the investigation area but it has an increase in its strength at the upper part close to the exit with out-of-plane velocity components up to -1m/s. The out-of-plane component of the flow is towards positive Z direction only for the planar jet part of the investigation area at the Planes 4 – 8.

For the Planes 5 – 9, the transverse flow gradually gets thinner and its out-of-plane component’s magnitude reduces. However, the shape and velocity distribution of the planar jet does not have any differences for these planes; 5 – 6 m/s in-plane velocity magnitudes at the exit of the device decreases to 4 – 5 m/s at the right side of the investigation area through the diagonal. Flow does not change for the Planes 7 – 9 as expected, because of the close position of these planes. Therefore, it is obvious that the change of the flow at different cross sections does not include any deformations occurring from the repositioning the device for the investigations at different planes.

The flow structure at the outlet of the SAC indoor unit starts changing at Plane 10. The jet flow is shifted upwards at Plane 10 and it is nearly 2D without any dominant out-of-plane flow components. In addition, the in plane velocity magnitudes reduce to 3 – 4 m/s at the exit of the device. The change of the flow structure is more important for the Plane 11, where the out-of-plane component of the velocity field totally changes from negative to positive direction which means that the direction of the transverse flow changes. The in-plane velocity field is getting back to its normal distribution with a wider jet cross-section. The thickness of the jet cross section at the Plane 12 is bigger than that of Plane 11, whereas the strength of the transverse flow is also more. The flow was visualized at the Planes 13 – 15 but the edge of the jet could not be seen, which means that the edge of the planar jet is somewhere between the Plane 13 – 14.

Plane 10 is at the geometric center of the device, but it is not the center of the jet flow. The electric motors and control unit are situated at the left side and there is not any flow at this part of the device. Therefore, the critical section for the outflow of the SAC indoor unit with straight CFF is Plane 10, where the transverse flows coming from the both sides meet at the geometric center of the device.

The velocity fields obtained by the SPIV measurements from the different planes were reconstructed to visualize the 3D flow structures of the outflow of the SAC indoor unit. The reconstructed 3D vector field at the outlet of the SAC indoor unit is given in Figure 4.7. After obtaining the 3D vector field, the flow can be visualized to have a better understanding and investigation. The resulting iso-surfaces of the velocity magnitude of 4 m/s are given in Figure 4.8. The core of the planar jet is divided into two parts at the Plane 10 and the two peak flow structure is obvious. The same iso-surface is given together with the iso-surfaces of the transverse flow for W= −0.6 m/s and W= 0.6 m/s in Figure 4.9.

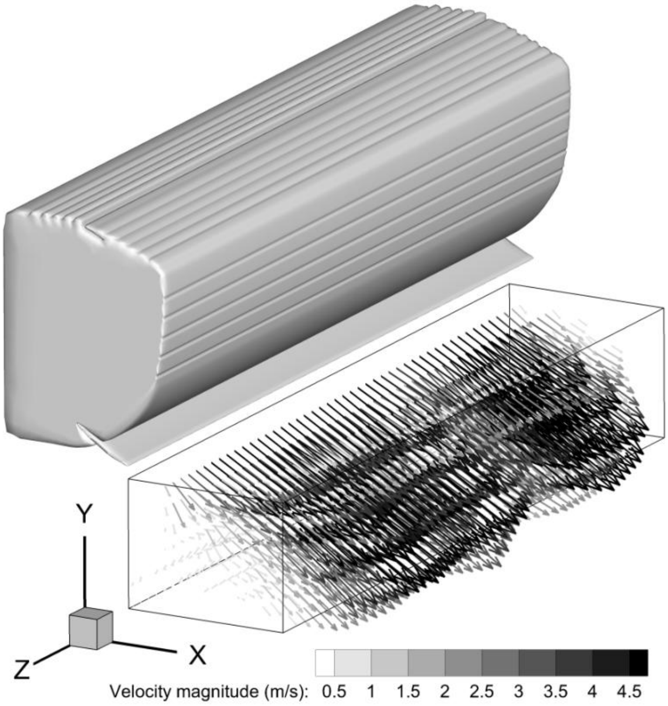

Figure 4.7 Reconstructed 3D vector field at the outlet of the SAC indoor unit.

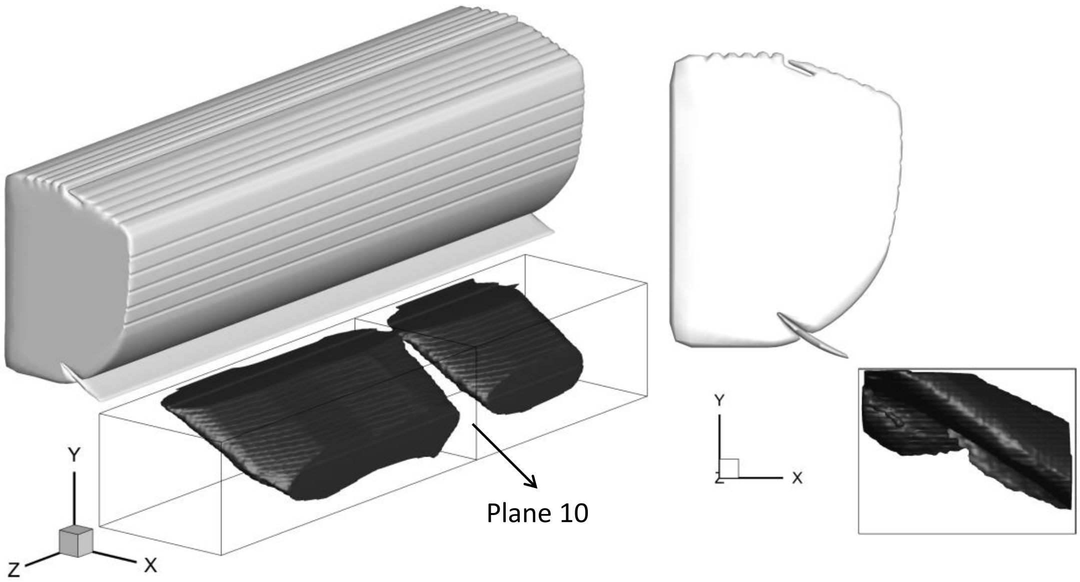

Figure 4.8 Iso-surface of the velocity magnitude 4 m/s for the flow at the outlet of a SAC indoor unit with a straight CFF.

Visualizing the important flow structures (iso-surfaces of the velocity magnitude 4 m/s, velocity vectors of the transverse flow with the W component equal to –0.6 m/s and 0.6 m/s) of the outflow of the SAC indoor unit with a straight CFF is given in Figure 4.10. It is seen from the Figure 4.10 that; there are two waves of the transverse flow moving under the planar jet along the negative z direction. For the first wave, surrounding air enters underneath the jet flow and mixes with the jet around Plane 5, and the second is more like a flow coming from the back side of the device starting from between Plane 5 and Plane 6 (although there is a big piece of cardboard to prevent the outflow from the air coming from the back side) and mixes with the jet flow until it reaches the separation point on the jet (Plane 10). On the other hand, the transverse flow at the other side of the device may be a part of the outflow of the device more than a transverse flow structure. It is thought that; the surrounding air comes from the left side, following the bottom edge of the device (not seen on Figure 4.11) increasing its speed by the suction of the jet flow, and mixes with the outflow of the device causing a tilted flow structure.

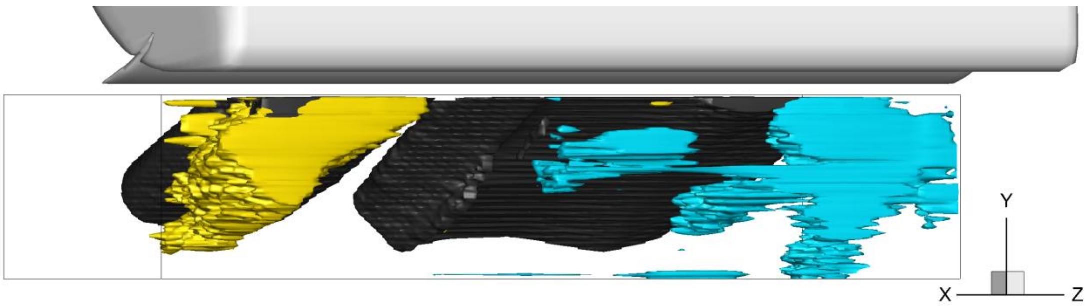

Figure 4.9 Iso-surfaces of the velocity magnitude 4 m/s (dark gray), transverse flow W= –0.6 m/s (blue), and transverse flow W= 0.6 m/s (yellow) for the flow at the outlet of a SAC indoor unit with a straight CFF.

In the results of the PIV measurements of Noel et al. (Noël, Farall, & Casarsa, 2007) it was also shown that, the flow resulting from the CFF may have some unexpected 3D characteristics different than the generally expected flow conditions of the CFFs (2D or planar jet flow); namely there is a recirculation region at the outlet of the CFF on the side where the driving motor is situated, a two peak jet flow was observed for which the existence was explained by the effect of the volute side walls and the metal ring that is located at the wheel center plane and used to avoid deflection of the blades. However, the CFF used in this study has more than one support ring but the two peak jet flow is still observed, instead of a multi-peak planar jet. Therefore, the main reason of the two peak flow structure observed in this research should be the transverse flows coming from the both sides of the device. In the study of Noel et al. (Noël, Farall, & Casarsa, 2007), they made single camera PIV measurements on a plane in the jet principal axis, therefore they might not had observed the transverse flow structures. In addition, there may be a critical width of the CFF for the transverse flows to develop to a level to influence the main stream.

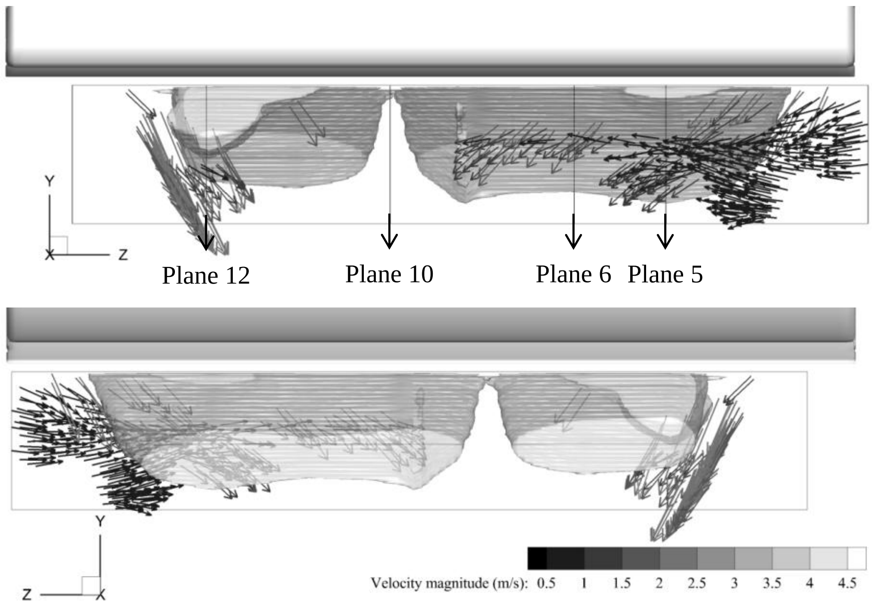

Figure 4.10 Important flow structures of the outflow of the SAC indoor unit with a straight CFF

360° rotation of the results about the y axis for visualizing the important flow structures of the outflow of the SAC indoor unit with a straight CFF is given in Figure 4.11. Iso-surface for the velocity magnitude equal to 2.5 m/s was drawn to visualize the planar jet flow and the following criteria (obtained by trial and error) were determined to visualize the transverse flow with vectors:

- The W component of the flow should be between -0.7 – -0.3 and 0.3 – 0.7 m/s,
- The U component of the flow should be less than 0.8 m/s,
- The V component of the flow should be greater than -0.4 m/s.

The group of the vectors which obey these criteria gathered under the planar jet flow and they show the secondary flow structures at the investigated domain.

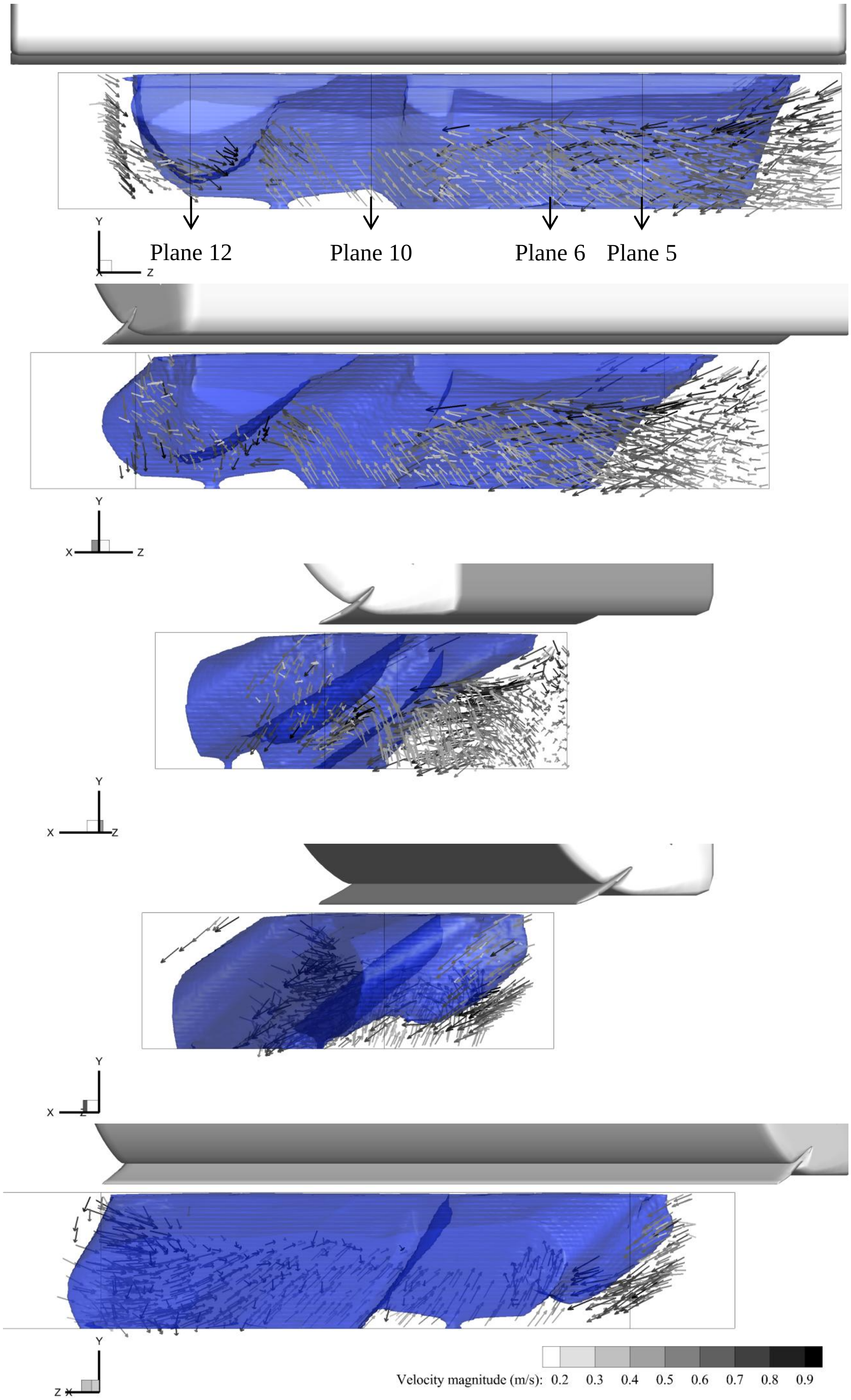

Figure 4.11 Rotation of the results about the y axis for visualizing the important flow structures of the outflow of the SAC indoor unit with a straight CFF

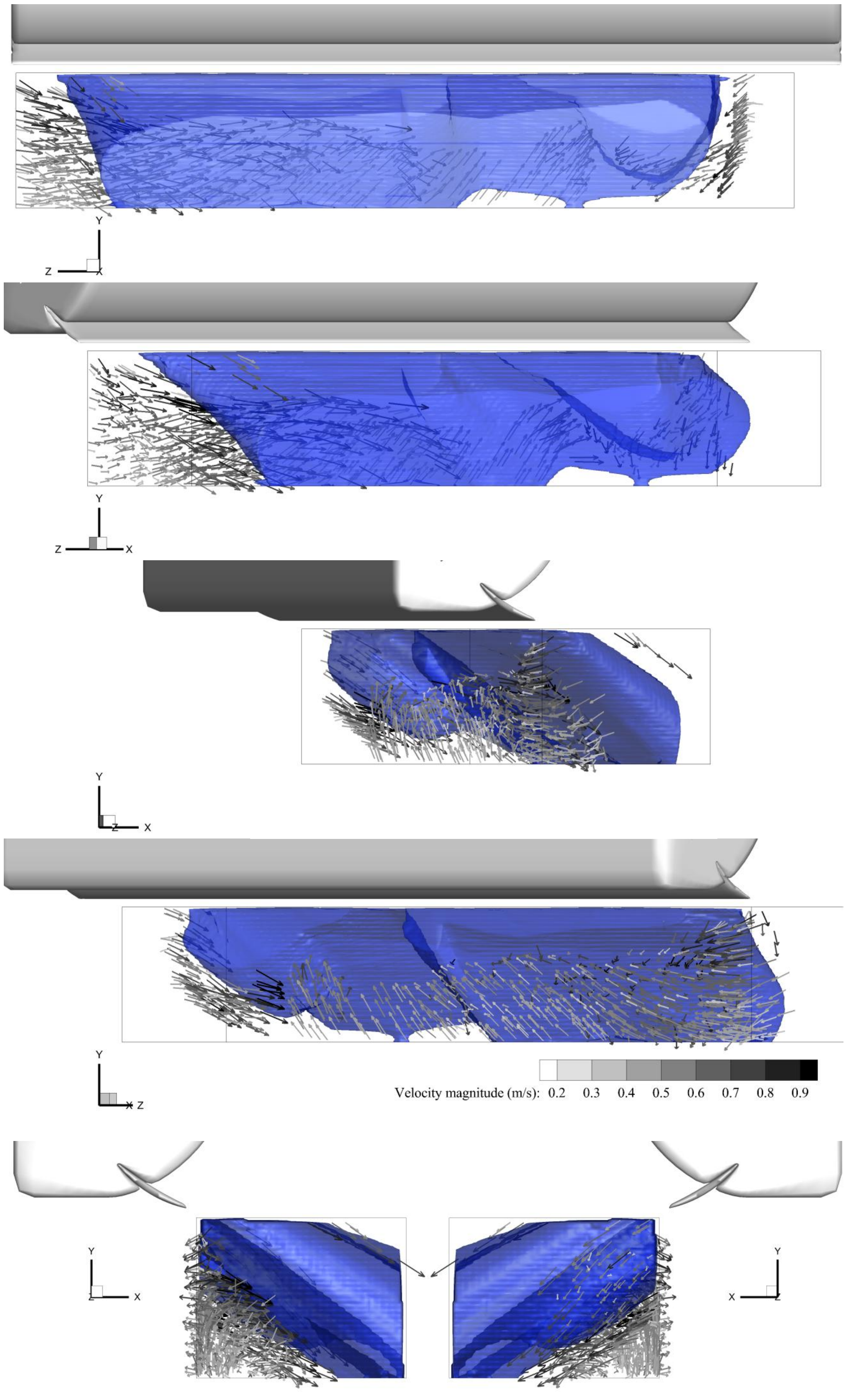

Figure 4.11 (continued) Rotation of the results about the y axis for visualizing the important flow structures of the outflow of the SAC indoor unit with a straight CFF

4.2.2 Outflow of the Model 2

The results of the measurements at the outflow of Model 2 from different planes are given in Figure 13 and 14. The direction of the flow does not change throughout the outlet section of the device; the planar jet flow is along the diagonal of the investigated area. In addition, the planar jet flow is symmetrical along the diagonal of the investigated area and the thickness of the main stream is homogenous throughout the outlet, except for the Plane 1 and 14, which are situated at the edges of the outlet.

The planar jet flow exists at the Planes 1-3 for Model 2 different than Model 1 for which the existence was determined at Plane 4. In addition, the out-of-plane component of the planar jet is in the positive direction with the W component up to 1 m/s. This result shows that the expansion at the edge of the planar jet is more dominant for the Model 2. On the other hand, the reversed transverse flow region which was observed for Model 1 (Regions A and C in Figure 4.5) also exists for Model 2 (Region F), which corroborates the inferences about the transverse flow and the effect of the device edges on the planar jet flow made for outflow of the SAC indoor units. The out-of-plane velocity component for the reversed transverse flow is up to 4 m/s for the Planes 2 and 3 and up to 1.5 m/s for the Plane 1. The out-of-plane velocity component of the reversed transverse flow was in the order of 1 m/s, and that of the planar jet flow was in the order of 0.1 m/s for the Model 1 at the edge planes. Therefore, the interaction between the planar jet and the surrounding air at the edge of the jet may lead to the result that; as the order of the magnitudes of the out-of-plane velocity component of the planar jet increases, the transverse flow becomes more dominant with higher velocity magnitudes. There is a backflow region (G) under the planar jet flow for Planes 1-3, within the first 2 cm from the edge of the outlet; however this backflow region vanishes at the Plane 4 where the movement of the surrounding air into the jet flow takes the place of the backflow. This backflow region was also observed for the Model 1 at the Planes 2 and 3 (again within the first 2 cm from the edge of the outlet). However, the strength of the backflow is less for Model 2, which is more like a wave of in-plane velocity component, separated from the main stream and joined the planar jet again in the far down-stream.

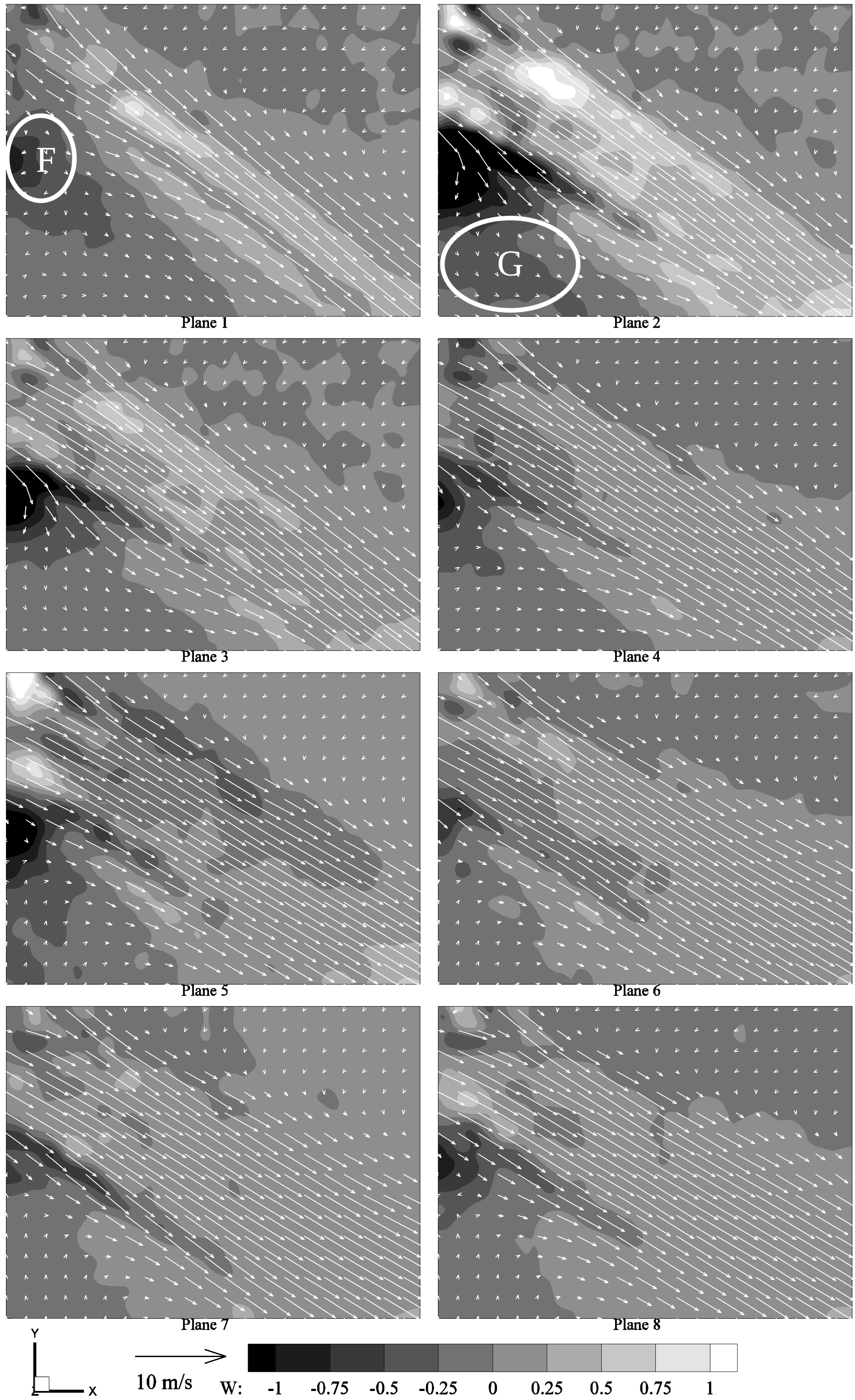

Figure 4.12 Velocity distributions for the planes on the different cross sections (Plane 1-8) at the outlet of Model 2

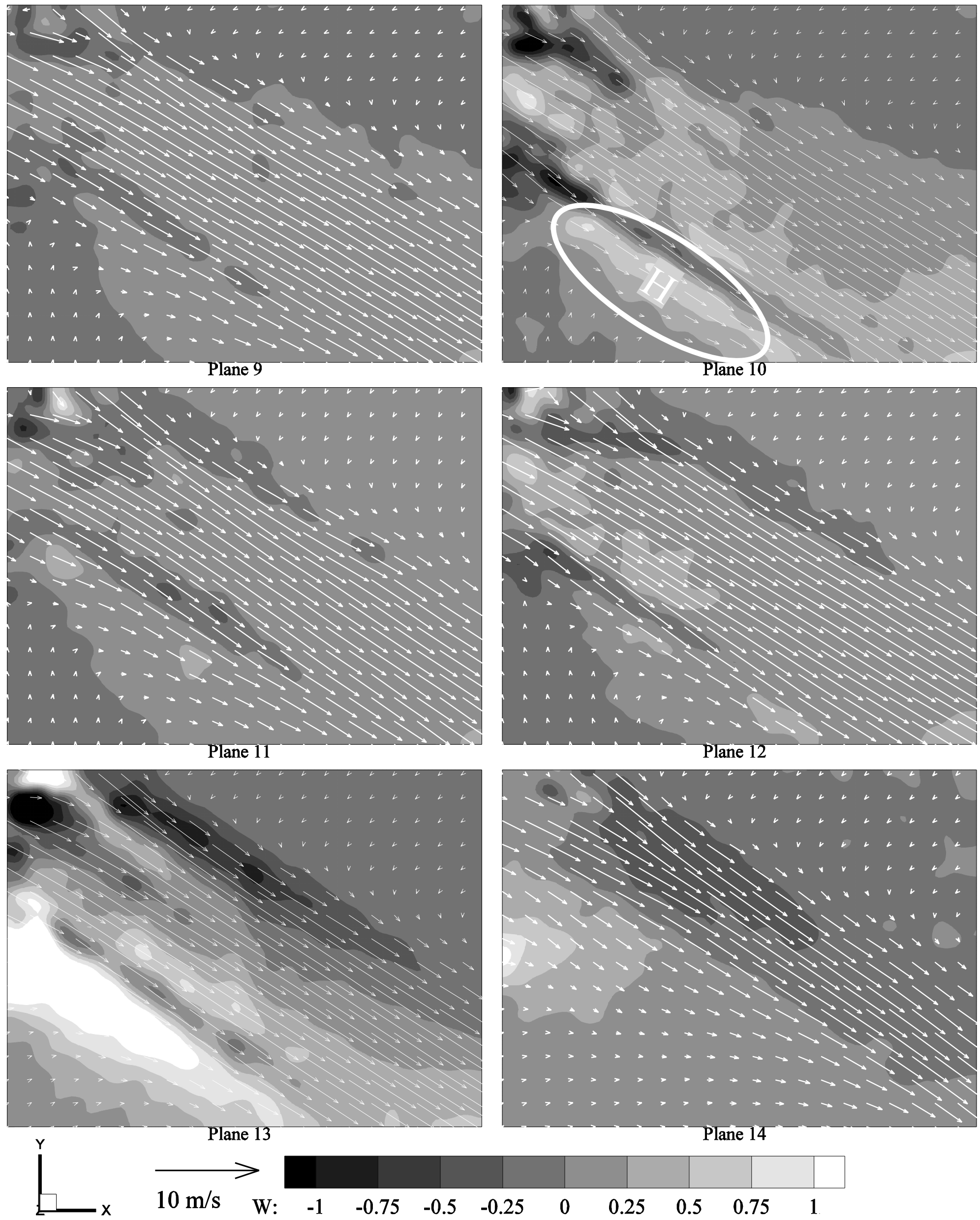

Figure 4.13 Velocity distributions for the planes on the different cross sections (Plane 9-14) at the outlet of Model 2

The transverse flow is effective until Plane 8 as the investigation planes moves towards the center of the device. However, there is almost no flow in the out-of-plane direction for the Plane 9. Plane 10 is situated at the middle of the device, although it is not the middle of the outflow section. Therefore, the out-of-plane component of the flow at Plane 10 is very complex because of the mixing of two transverse flows coming from opposite directions. Region H which is situated just under the planar jet flow is the first signal of the transverse flow coming from the left side of the device. Although it is not seen so clear in Planes 11 and 12, it reappears in Plane 13 very strongly and places at the same position as the Region F in Figure 4.13 at Plane 14, having a positive out-of-plane component.

The velocity vector fields obtained by the SPIV measurements were reconstructed to visualize the 3D flow structures of the outflow of Model 2. The iso-surface of the velocity magnitude of 5 m/s is given in Figure 4.14. Similar to the Model 1, the core of the planar jet flow is divided into two parts; however, the division can be visualized for the velocity magnitude of 5 m/s (it was 4 for Model 1) and the division point is at the Plane 11 for the Model 2. Moreover, iso-surface of the velocity magnitude 4 m/s is given in Figure 4.15 together with the iso-surfaces of the transverse flow W= −1 m/s, and transverse flow W= 1 m/s for the flow at the outlet of the Model 2.

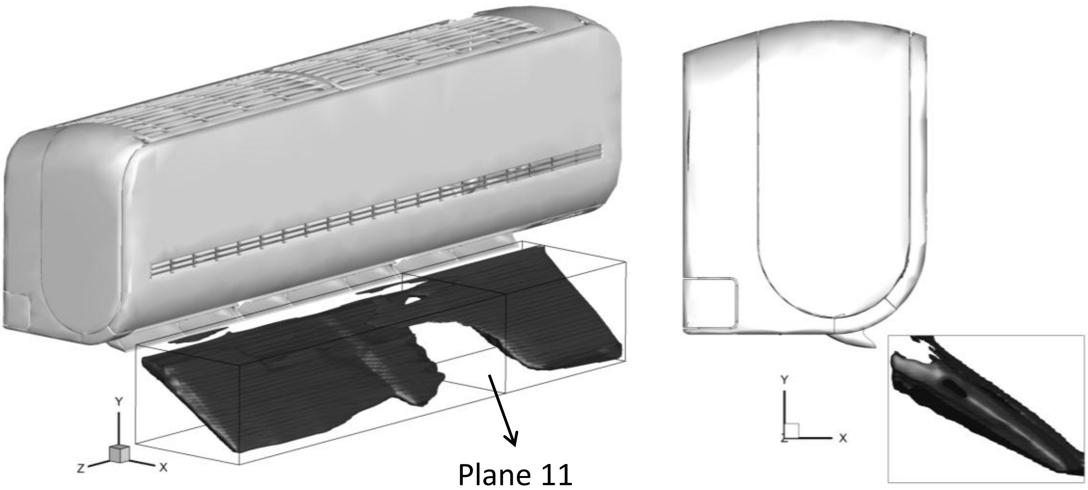

Figure 4.14 Iso-surface of the velocity magnitude 5 m/s for the flow at the outlet of Model 2

360° rotation of the results about the y axis for visualizing the important flow structures of the outflow of Model 2 is given in Figure 4.16. Iso-surface for the velocity magnitude equal to 4 m/s was drawn to visualize the planar jet flow and the following criteria (obtained by trial and error) were determined to visualize the transverse flow with vectors:

- The W component of the flow should be between -1.1 – -0.3 and 0.3 – 1.1 m/s,
- The U component of the flow should be less than 0.7 m/s,
- The V component of the flow should be greater than -0.3 m/s.

The group of the vectors which obey these criteria gathered under the planar jet flow and they show the secondary flow structures at the investigated domain. It is seen from the results that, Model 2 has a better design than Model 1, which resulted to a better performance and a smoother outflow (bigger CFF diameter, optimized CFF, rear wall, and vortex wall dimensions, bigger outlet height might be the factors for a better outflow).

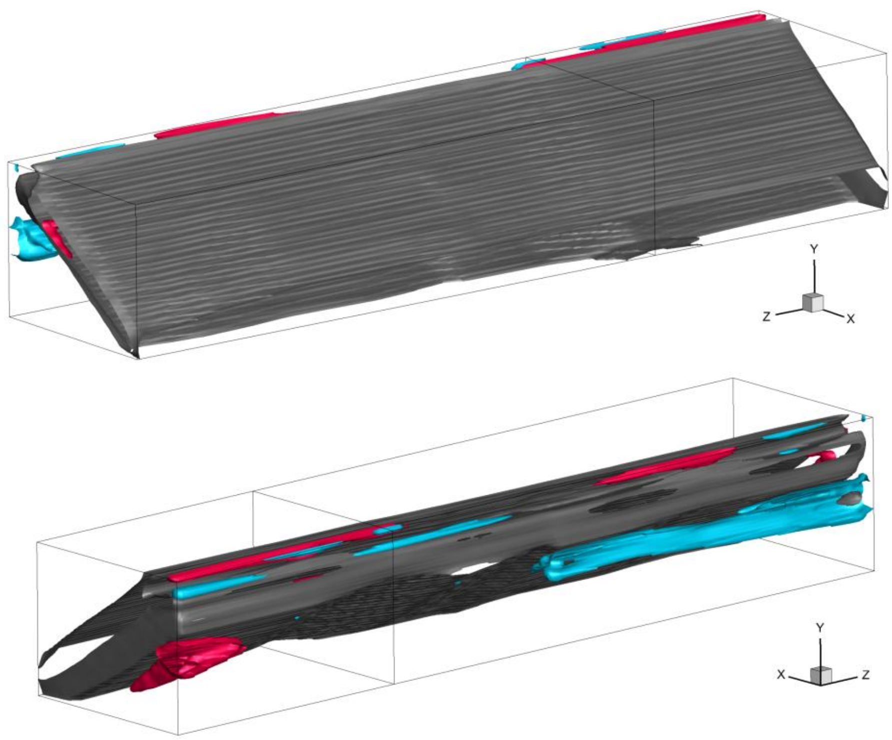

Figure 4.15 Iso-surfaces of the velocity magnitude 4 m/s (dark gray), transverse flow W= −1 m/s (blue), and transverse flow W= 1 m/s (red) for the flow at the outlet of the Model 2

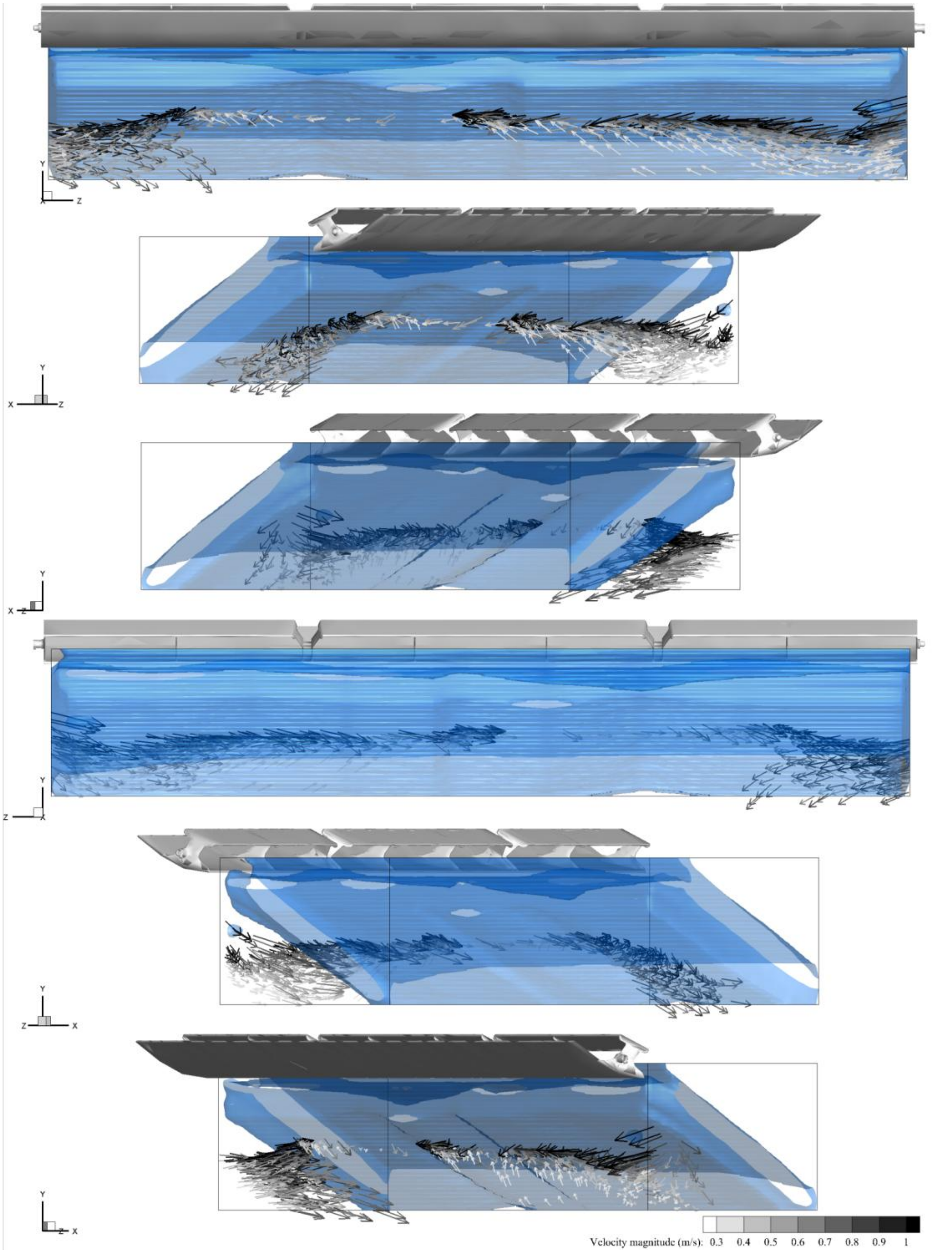

Figure 4.16 Rotation of the results about the y axis for visualizing the important flow structures of the outflow of Model 2

4.2.3 Outflow of the Model 3

The velocity vector fields obtained by the SPIV measurements at 14 different planes were reconstructed to visualize the 3D flow structures of the outflow of Model 3. The iso-surface of the velocity magnitude of 5.5 m/s is given in Figure 4.17. Different than the Model 1 and 2 the, the core of the planar jet flow is divided into three parts; however, the division can be visualized for the velocity magnitude of 5.5 m/s and the division points are at the Plane 5 and 9 for the Model 3. Moreover, iso-surface of the velocity magnitude 4 m/s is given in Figure 4.18 together with the iso-surfaces of the transverse flow W= –0.8 m/s, and transverse flow W= 0.8 m/s for the flow at the outlet of the Model 3.

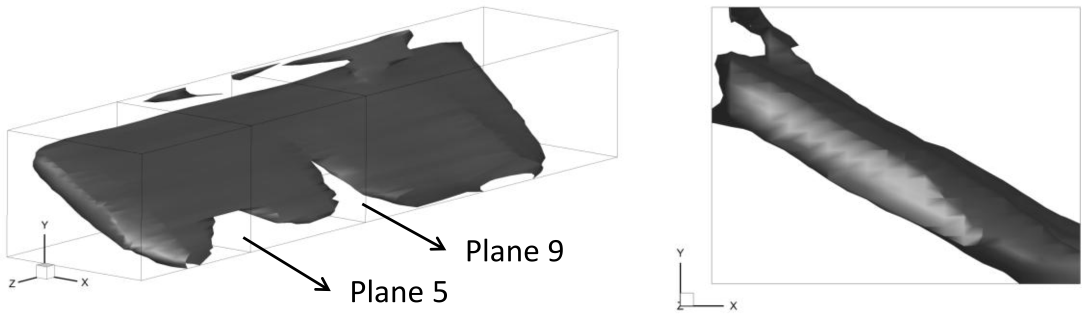

Figure 4.17 Iso-surface of the velocity magnitude 5.5 m/s for the flow at the outlet of Model 3

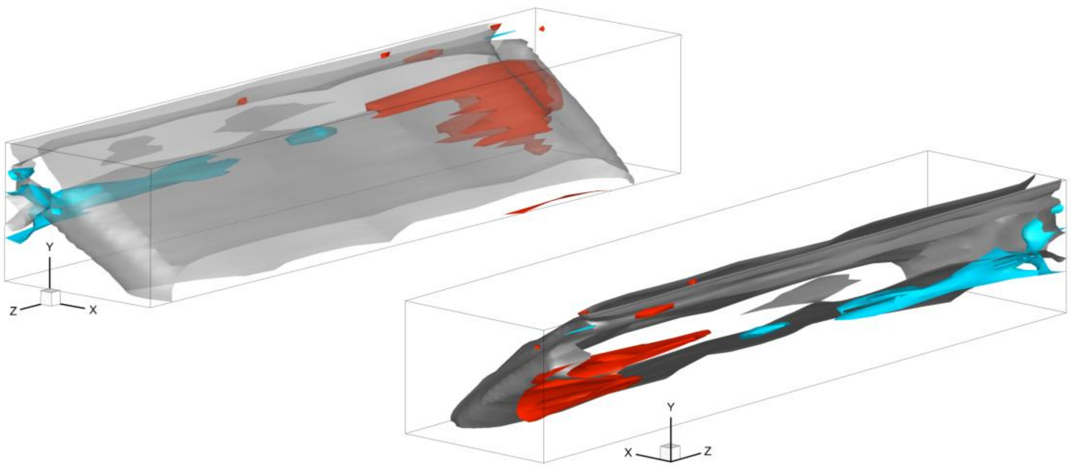

Figure 4.18 Iso-surfaces of the velocity magnitude 4 m/s (gray), transverse flow W= –0.8 m/s (blue), and transverse flow W= 0.8 m/s (red) for the flow at the outlet of the Model 3

The important flow structures of the outflow of Model 3 are given in Figure 4.19. Iso-surface for the velocity magnitude equal to 4 m/s was drawn to visualize the planar jet flow and the following criteria (obtained by trial and error) were determined to visualize the transverse flow with vectors:

- The W component of the flow should be between -1.1 – -0.3 and 0.3 – 1.1 m/s,
- The U component of the flow should be less than 0.7 m/s,
- The V component of the flow should be greater than -0.7 m/s.

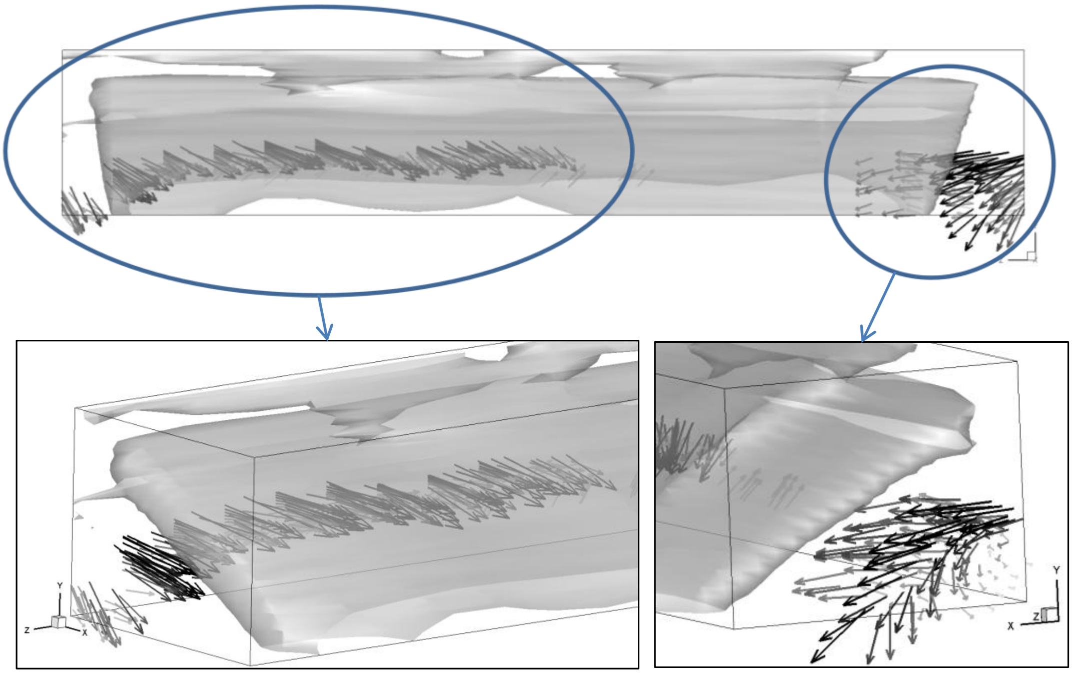

Figure 4.19 The important flow structures of the outflow of Model 3

The group of the vectors which obey these criteria gathered under the planar jet flow and they show the secondary flow structures at the investigated domain. It is seen from the results that, the outflow of the Model 3 is similar to that of Model 2, but the velocities at the outflow are higher for the Model 3.

CHAPTER FİVE
CASE STUDIES

In this part of the thesis; the effects of the different parameters on the outflow characteristics are investigated. Firstly, the effect of the skewed CFF on the outflow characteristics of Model 1 is discussed, then the results of the velocity measurements at the outlet section is given and the effect of the angular position of the directing airfoil on the outflow characteristics are given, and then the effect of the fan rotational speed on the outflow characteristics is investigated.

5.1 Outflow of the Model 1 with a Skewed CFF

Two different CFFs were used inside Model 1 which are given in Figure 5.1. Skewed rotor was made by twisting the rotor's outer shroud circumferences until the reference displacement at two ends of blade along axial direction is about one blade pitch relative to original straight case. These CFFs are placed into the same SAC indoor unit for the measurements, so that all other parameters as geometry, heat exchanger, operating speed etc. remained the same. Therefore, only the effects of different CFFs on the flow were seen.

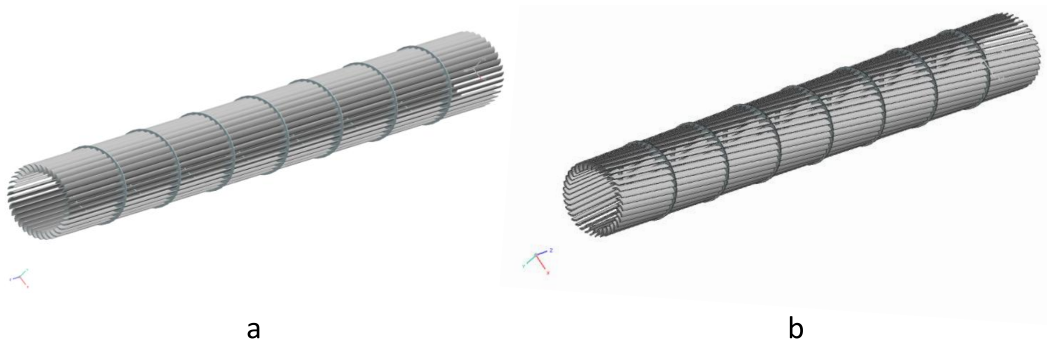

Figure 5.1 Two different CFFs used in the measurements; a) Straight CFF, b) One pitch skewed CFF

The results of the SPIV measurements at the outlet of the Model 1 with a skewed CFF are given in Figure 5.2 and Figure 5.3 for the Planes 0-7 and 8-15 respectively. Similar to the outflow of the Model 1 with straight CFF, the in-plane movement of the air is very slow at Plane 0 whereas the out-of-plane movement is dominant at the left side of the investigated area. The axis of the planar jet flow is along the diagonal of the investigated area for the Plane 1 and the in-plane velocity of the air at the core of the jet flow is as high as 1.5 m/s. On the upper side of the jet flow, the surrounding air moves into the main stream (B) whereas at the lower part a reversed flow occurs on the left side of the investigated area (C). The axis of the planar jet flow does not change for the Planes 2 and 3 but the maximum values of the in-plane velocities are slightly higher (2 and 2.5 m/s for the Planes 2 and 3, respectively). The reversed flow at the Region B also exists for the Planes 2 and 3.

The out-of-plane velocity component has positive values for the main stream, which means that the flow is directed to the right side of the device for Planes 1, 2 and 3. This result is consistent with the expectation of the spreading of the planar jet flow. However, different than the Model 1 with a straight CFF, the in-plane and out-of-plane components of the jet flow has higher velocity magnitudes (-1/-1.5 m/s for the out-of-plane component) at the right edge of the device.

From Plane 4 to Plane 6, the major axis of the planar jet flow ascents and the in-plane velocity at the core increases to 5 m/s. The movement of the surrounding air at the upper and lower parts of the jet flow is clear at the Planes 4 - 6. The thickness of the jet increases at the Plane 6 and the reversed flow vanishes. However, the out-of-plane velocity is still in the negative direction and is dominant for the reversed flow region. Two darker zones (negative out-of-plane component) starting from the upper and lower sides of the jet core region along the axis of the jet flow are apparent for Planes 4-6. The reason for this flow structure might be the transition from the edge effect to the main flow part. The in-plane thickness of the planar jet seems bigger for the skewed CFF than the straight CFF at Plane 6; however, this is a result of the stronger transverse flow under the planar jet.

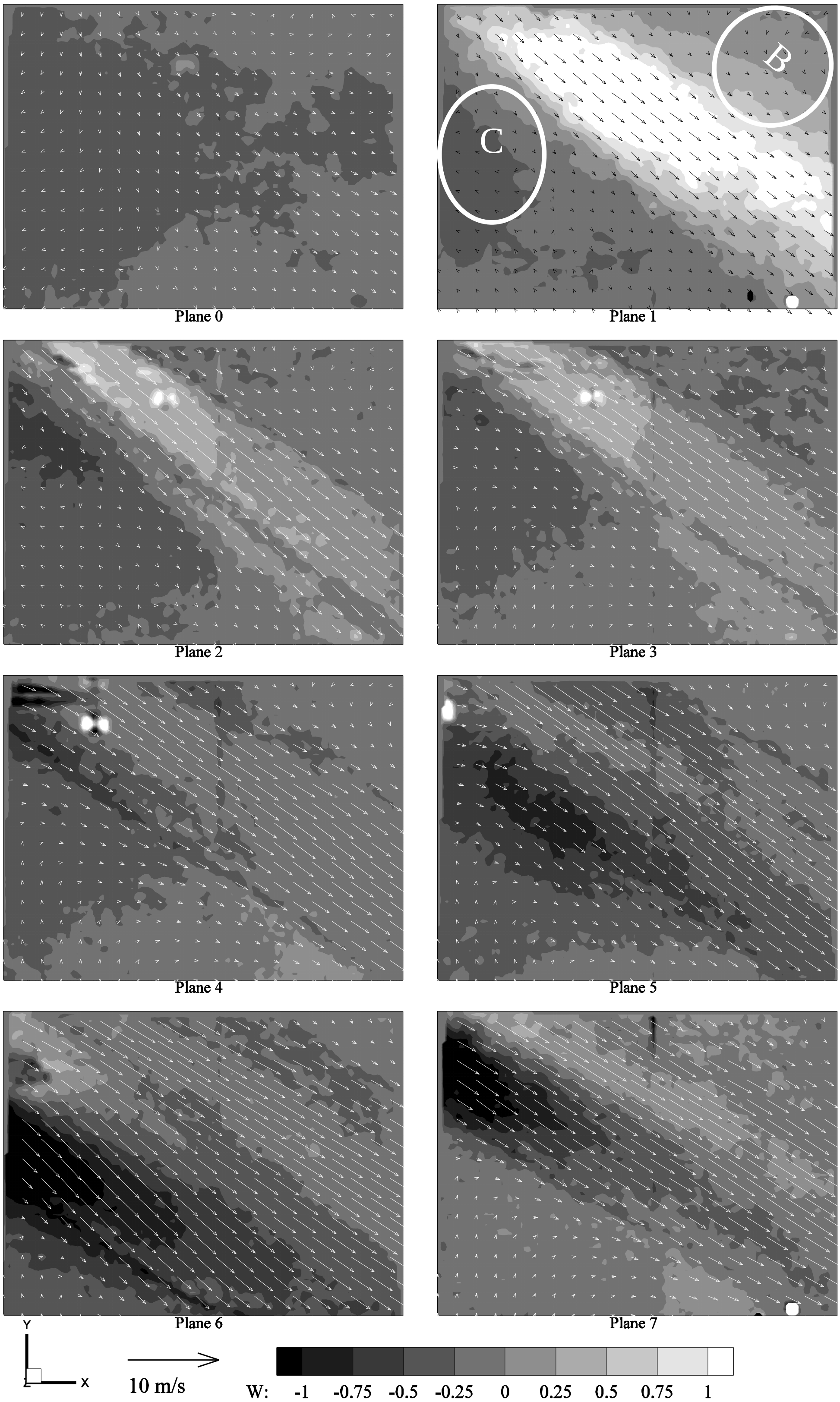

Figure 5.2 Velocity distributions for the planes on the different cross sections (Plane 0-7) at the outlet of Model 1 with a skewed CFF

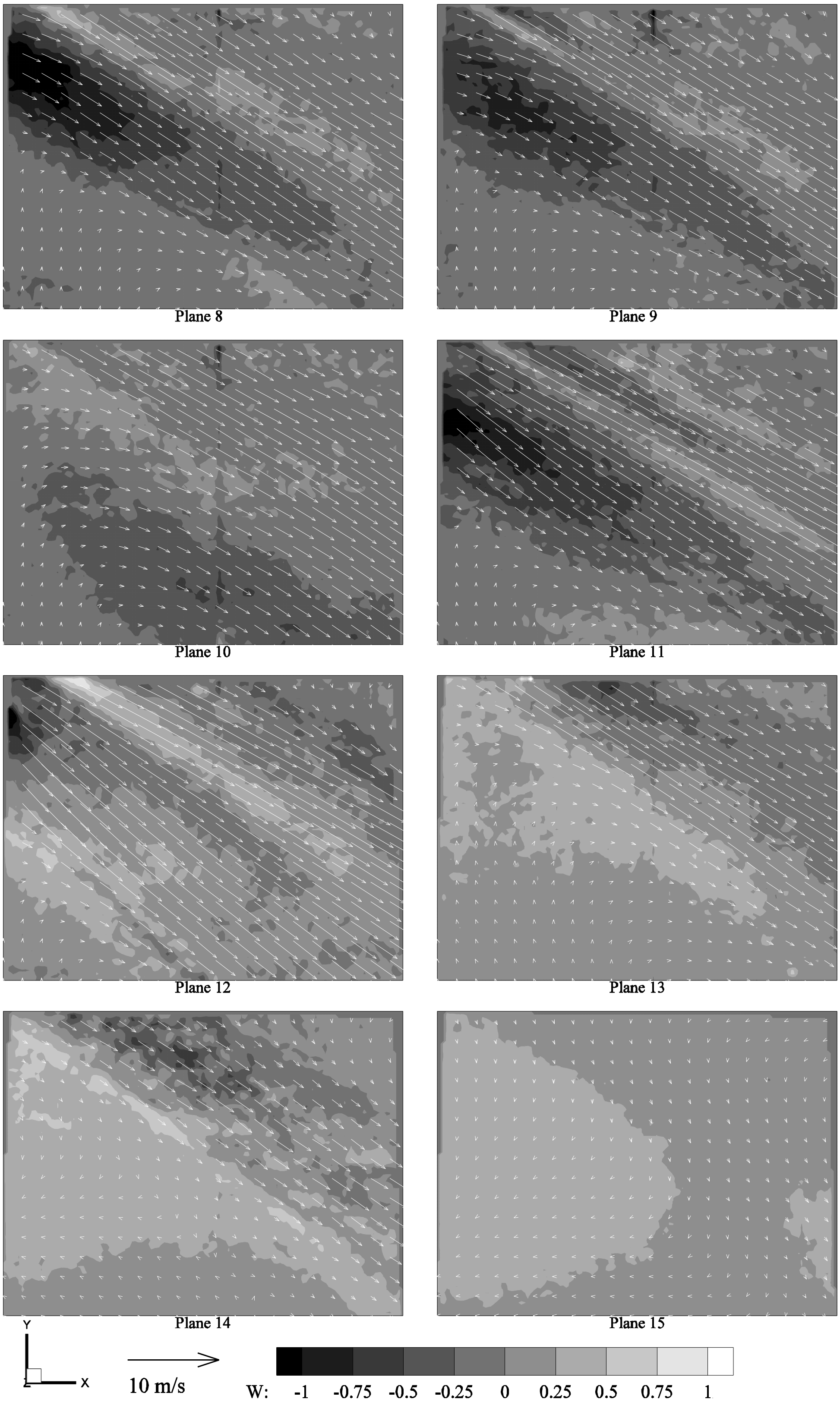

Figure 5.3 Velocity distributions for the planes on the different cross sections (Plane 8-15) at the outlet of Model 1 with a skewed CFF

The results showed that the flow structure for the Planes 7 - 9 are similar such that; the velocity magnitudes, direction and the thickness of the planar jet flow obtained from these planes are concordant, the velocity of the transverse flow region under the jet flow reduces, the in-plane movement of the surrounding air does not change whereas the out-of-plane velocity component of the main stream starts to change from positive to negative direction. The transverse flow for the Model 1 with a straight CFF at the Planes 7-9 were almost disappeared, however it is very dominant for the Model 1 with a skewed CFF at these planes.

The thickness of the planar jet flow reduced and the in-plane velocities below the jet decreased for the Plane 10 similar to the flow structure at Plane 10 for the Model 1 with straight CFF. This may be a result of the merging of the transverse flow under the device into the planar jet flow. In addition, the direction of the expansion of the jet flow on its axis is changed from positive to negative as in the case of straight CFF. Although the flow at Plane 11 is much more like the flow structure at Planes 7-9 with a transverse flow along the negative Z direction, the transverse flows coming from the both sides of the device are seen at Plane 12, where a big, negative out-of-plane velocity region and a positive out-of-plane velocity region are positioned one above the other, under the main stream. The thickness of the planar jet flow increased compared with the Plane 10 and 11. The negative and positive out-of-plane components of the flow are also seen at Plane 13. However, the flow through the positive side is dominant whereas the flow along the negative side is weaker compared with Plane 12. Plane 13 is situated at the edge of the CFF; however it is not at the edge of the directing airfoil and the device. Therefore, the flow structure suddenly changes at Plane 13 compared with Plane 12. The planar jet flow is thinner and the transverse flow’s direction totally changed from negative to positive.

Although there is not any flow after the Plane 13 for the Model 1 with a straight CFF, the jet flow and its co-structures are observed for the Model 1 with a skewed CFF. The transverse flow along the positive Z direction exists and has a wider area than that of Plane 13 for the Plane 14. Furthermore, spreading of the planar jet flow through the negative Z direction is apparent. Finally, the in-plane component of the flow vanishes for the Plane 15, but the transverse flow is still visible.

The in-plane 3D data obtained from SPIV measurements for a SAC indoor unit with a skewed CFF were also interpolated to a 3D prismatic region to have a better visualization and understanding of the flow structures. The 3D reconstruction of the flow at the outlet of the device and 360° rotation of the results about the y axis for visualizing the important flow structures of the outflow of the SAC indoor unit with a straight CFF is given in Figure 5.4. Iso-surface for the velocity magnitude equal to 2.5 m/s was drawn to visualize the planar jet flow and the following criteria were determined to visualize the transverse flow with vectors:

- The W component of the flow should be between -0.7 – -0.4 and 0.3 – 0.7 m/s,
- The U component of the flow should be less than 0.8 m/s,
- The V component of the flow should be greater than -0.4 m/s.

The core of the planar jet flow is more dominant at the left side of the device (around Plane 12), which is apparent from the velocity iso-surfaces given in Figure 5.4. This part of the iso-surface is also has a bigger structure for the straight CFF, but this effect is wider for the skewed CFF. Under ideal conditions the flow should be symmetric; however the inexistence of the planar jet flow at the control unit part of the device and the twisting effect of the skewed angle rotor changes both the transverse and planar jet flow characteristics. A similar result was obtained by the study of Tsai et al. (2006), in which they showed that the outflow of the CFF deviates from the normal direction of the rotor-axis for the skewed rotors and this deviation increases for the larger rotor skew angles.

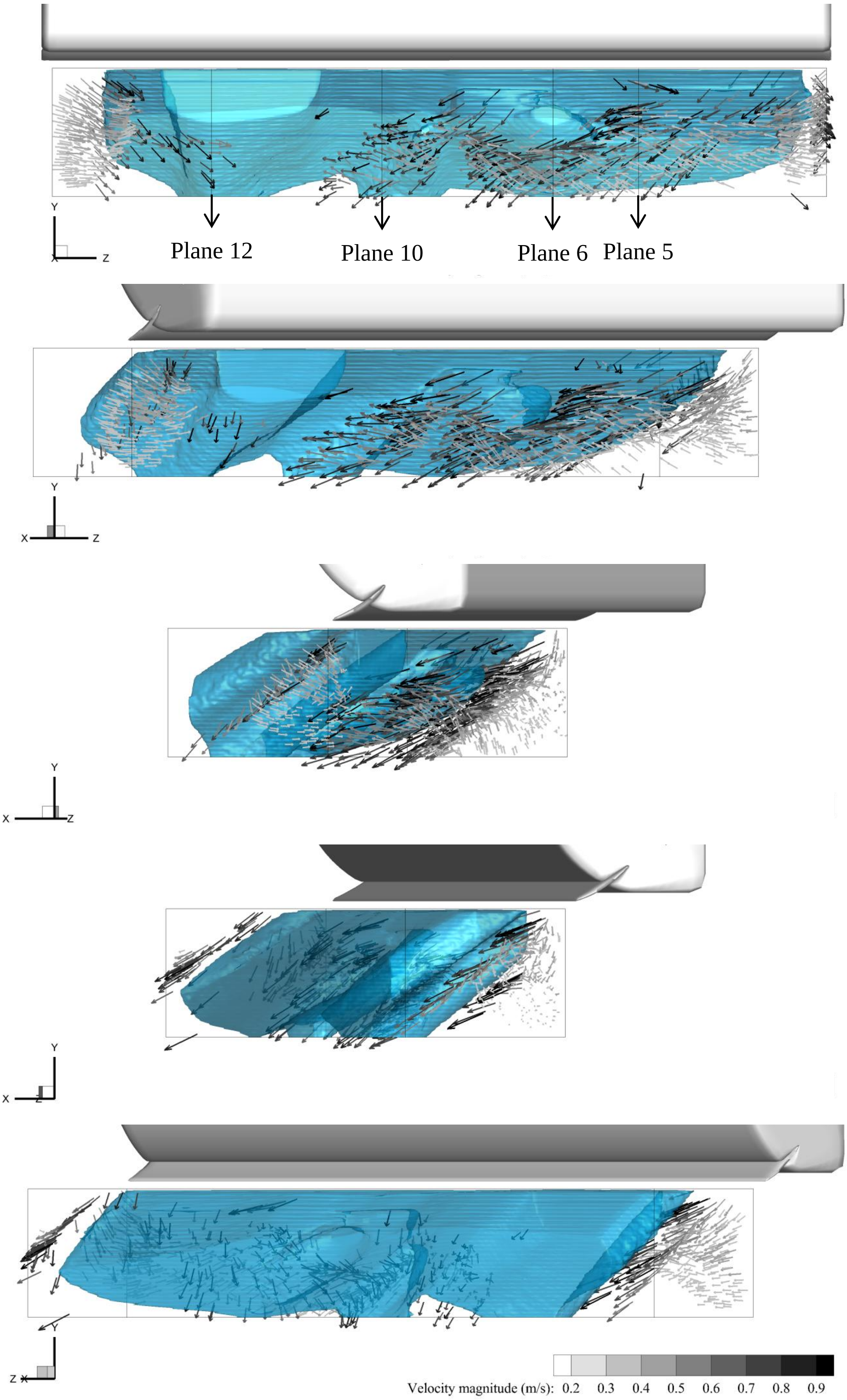

Figure 5.4 Rotation of the results about the y axis for visualizing the important flow structures of the outflow of the SAC indoor unit with a skewed CFF

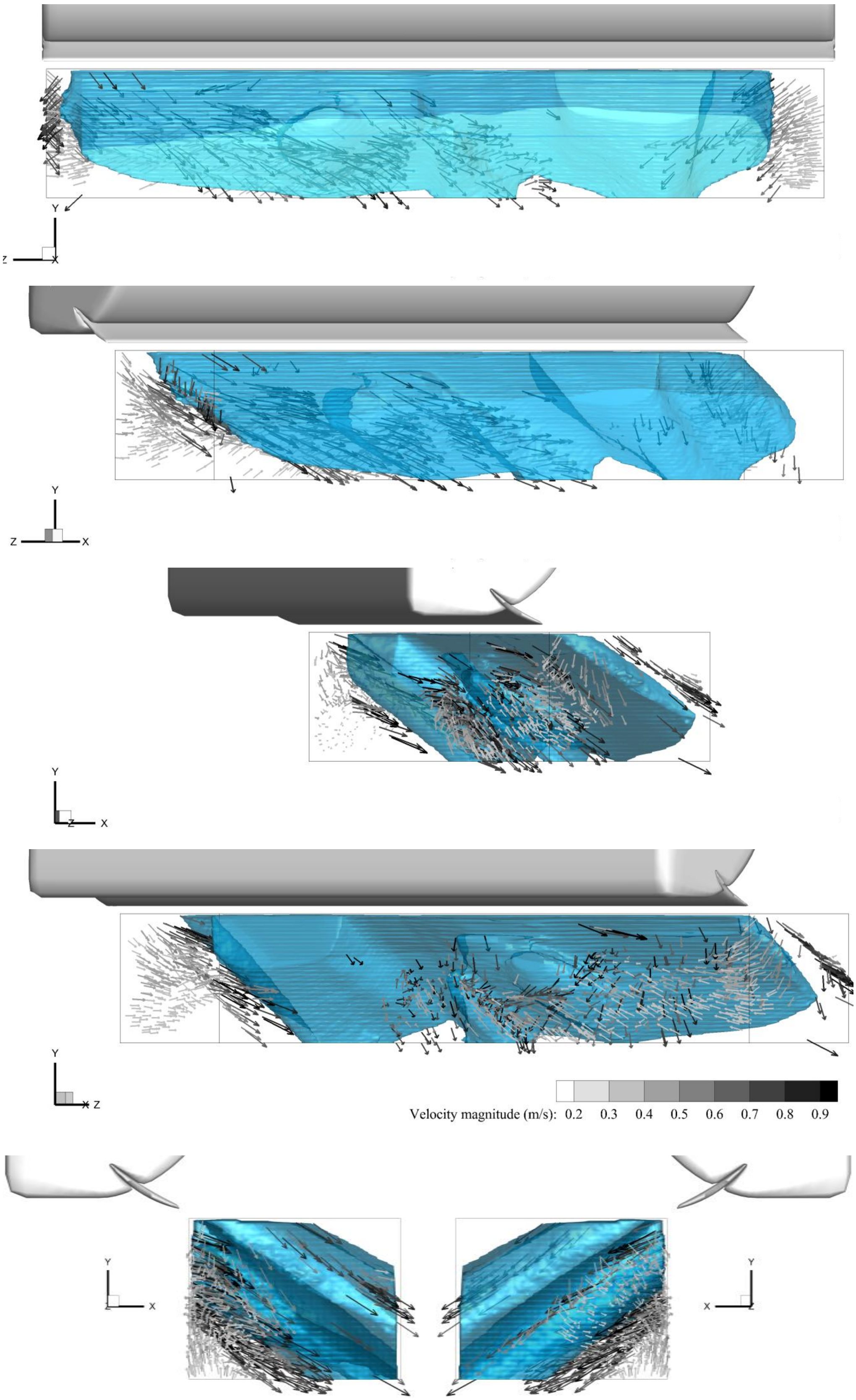

Figure 5.4 (continued) Rotation of the results about the y axis for visualizing the important flow structures of the outflow of the SAC indoor unit with a skewed CFF

5.2 Results of the Flow Measurements at the Outflow Section of the Device

The form and characteristics of this flow depend on the CFF parameters, the outlet section geometry and the directing airfoil's geometric parameters. Therefore these parameters should be well designed to control the outflow of the SACs, however except the outlet section geometry of the body, they depend on the different demands of the end user. Angular position of the airfoil may change automatically for different operating conditions of the device (heating and cooling) or be adjusted by the users for their personal demands. In addition, new SAC designs have some complex algorithms to control the airflow inside the room for which the angular position of the directing airfoil continuously changes.

Flow around an airfoil is a well-known phenomenon because of the airfoils' large usage for aviation industry and there are numerous experimental and numerical studies on this subject. However, in most cases investigations are made under certain boundary conditions such as wind tunnel experiments. Distinctively in this case, flow formed by the CFF meets the airfoil and their interaction plays an important role on the outflow of the RACs. Although the producers might have been interested on this interaction to optimize the outflow, there are almost no studies on this subject in the literature. Both the numerical and the experimental studies mentioned above in the introduction chapter have some results on the outlet section of the CFF, but none of them modeled or included the directing airfoil. As in the case of SACs, directing airfoil may be in a close position to the CFF and the orientation of it may affect the CFF flow, resulting to a change in the performance. Therefore in this part of the thesis, effect of the angular position of the flow directing airfoil of a SAC on the outflow characteristics was investigated by PIV.

200 image pairs from both cameras were taken for investigation. The raw data was processed for obtaining the instantaneous vector fields, and the results are given for the average of these 200 instantaneous velocity distributions.

5.2.1 Validation of the Panoramic PIV Method

To verify the results of the panoramic PIV measurements, a path was defined at the outlet section of the device and the velocity profiles on the defined path were compared with the results of the SPIV measurements. As seen in Figure 5.5, the position and shape of the jet flow at the outlet of the device is similar on both measurements. The peak value and the position of the velocity is concordant, however there is a slight change on the right side of the velocity profile. The average velocity through the path is found as 3.56 m/s and 3.51 m/s for the SPIV and PIV measurements, respectively.

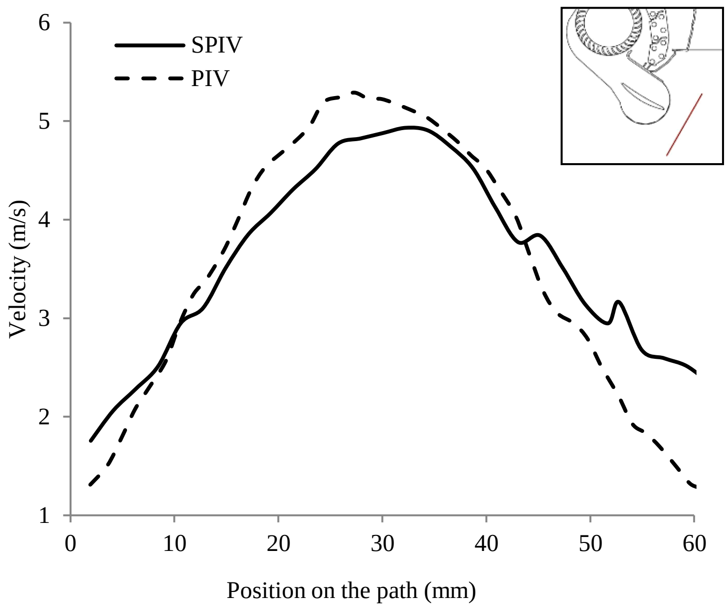

Figure 5.5 Verification of the panoramic PIV results

5.2.2 Effect of the Angular Position of the Directing Airfoil on the Outflow

The angular position of the directing airfoil was defined by the angle between the chord and horizontal (β), and changed between 15 to 60 degrees with 15 degree increments. Higher values for β correspond to higher angles of attack for the airfoil considering the form of the CFF flow without any obstacles. The different angular positions of the airfoil is given in Figure 5.6

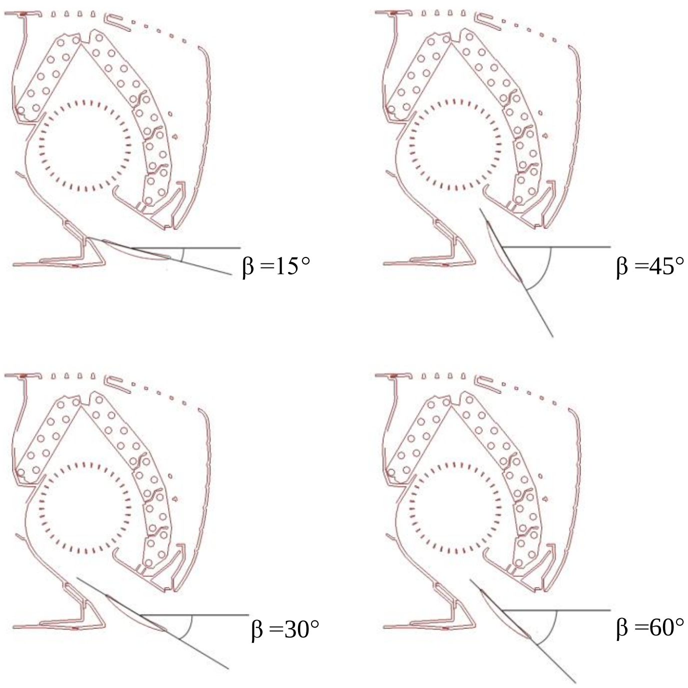

Figure 5.6 Different angular positions of the airfoil

A close look to the flow at the outlet section of the device for β=60° is given, and the body of the device, directing airfoil and its shadow is shown in Figure 5.7. Velocity vectors are directed upwards towards the fan's rotating direction on the left side of the Figure 5.7 above the shadow (Region A). A part of the eccentric vortex which is the most important characteristic structure of a CFF flow is expected to be seen on this region. Eccentric vortex is the main source of the CFF flow because of the low pressure region on it, which provides the air suction from the upstream and behaves like a seal against the reversing flow of the air from the downstream. The vortex is situated above the airfoil (Region B) and Regions C and D in Figure 5.7 represent the movement of the steady air by the effect of the high velocity jet flow.

The effect of the angular position of the directing airfoil on the flow is given in Figures 5-8. For the β=15° (Figure 5.8), the leading edge of the airfoil is nearly touching on the surface of the rear wall, therefore the air hits on the airfoil and cannot pass to the underside. As a result, the flow is redirected by the airfoil and the jet flow coming out of the device is clearly seen. Because of the difficulties in illuminating and visualizing, the eccentric vortex could not be seen on Figure 5.8.

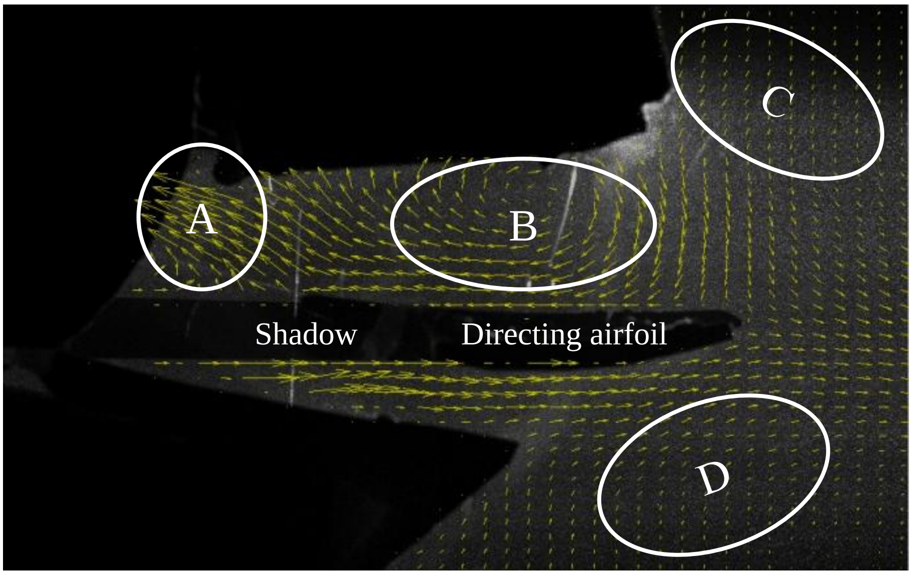

Figure 5.7 Vector field at the outlet section

For the β=30° (Figure 5.8), which is the predefined position, flow passes around the airfoil without facing any obstacles. Flow directed by the CFF is nearly parallel to the chord of the airfoil which corresponds to the 0° angle of attack. Only a small shift is seen on the flow while passing around the airfoil. Therefore velocity distribution on both sides of the airfoil is homogeneous and no separation is seen on the faces. The velocities of the jet flow at the outlet section is smaller than for the case of β=15°. In addition, a region (E) is seen on Figure 6 which might be a part of the eccentric vortex.

Flow is separated by the airfoil for the β=45° (Figure 5.8). The lower part of the flow passes parallel to the lower side of the airfoil and get out of the device without facing any obstacles. A big vortex is observed on the upper concave face of the airfoil, which narrows the outflow section resulting to the lowest velocities at the outlet section for the investigated flow conditions. A reversed flow occurs on Region F that may be a part of the eccentric vortex and which means that the position of the eccentric vortex might be changing with the angular position of the airfoil.

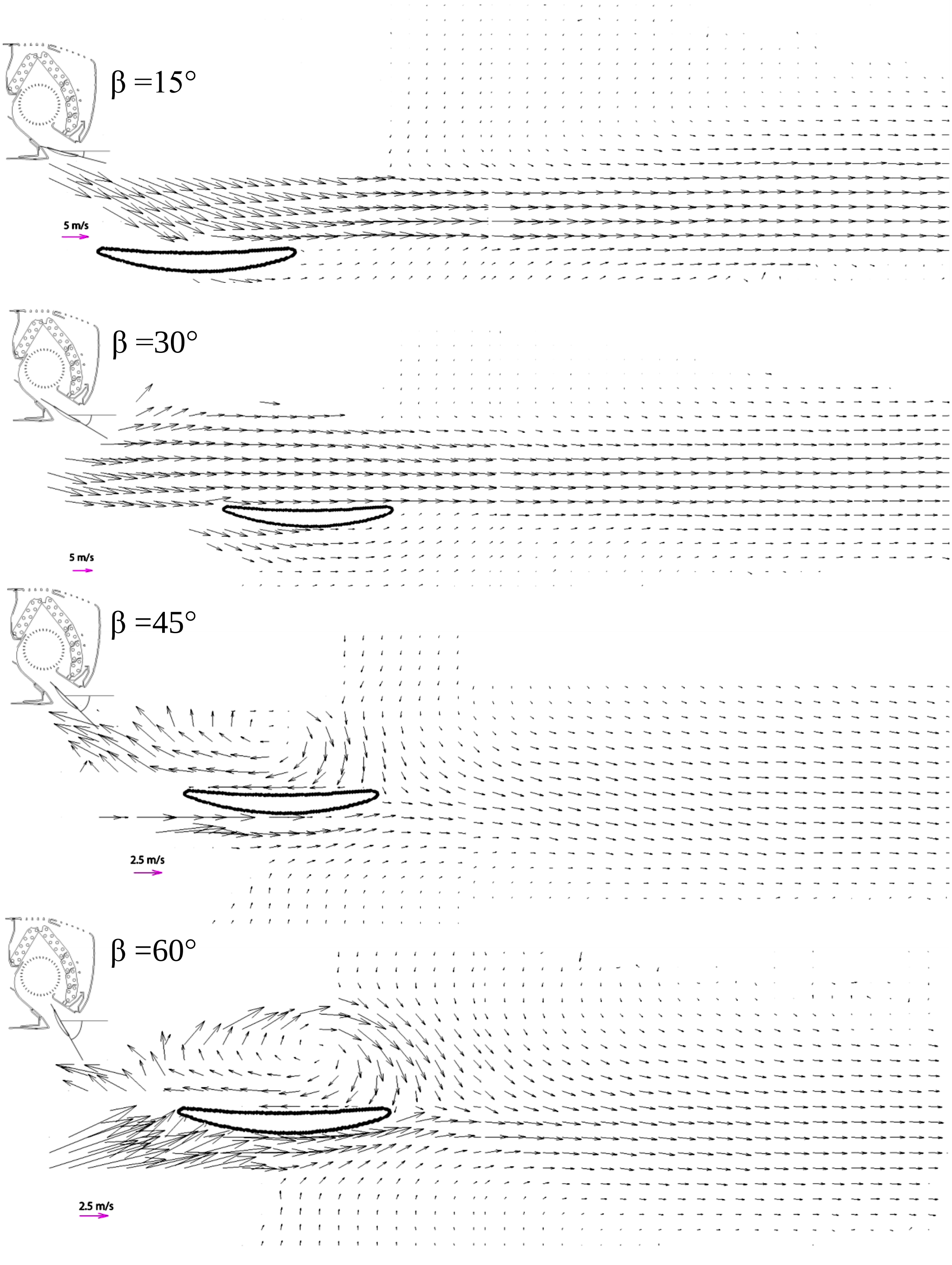

Figure 5.8 Velocity distribution at the outlet of the device for β =15°, 30°, 45°, and 60°

For the β=60° (Figure 5.8), results are similar to β=45° except the velocities at the lover side of the airfoil and at the outflow section are higher for this case.

Results of this study show that flow is directed by the airfoil and a circulating region is observed above the airfoil for different angular positions. Flow at the investigated section of the device includes a part of the eccentric vortex, which is the most important structure of a CFF flow, although a deeper investigation is needed for revealing this effect. The angular position of the airfoil affects the form and characteristics of the jet flow at the outlet section both on the shape and the velocity.

Critical angular position of the directing airfoil is between 30°-45° for which a transition from a smooth flow to a vortex above the airfoil occurs. For β=45° and 60°, the vortex above the airfoil behaves like a seal against the flow and forces the air to pass below the airfoil. Depending on the airfoil geometry, the distances between the leading edge of the airfoil, CFF and vortex wall may be the important parameters to control the flow.

5.3 Effect of the CFF Rotational Speed on the Outflow Characteristics

The rotational speed of the CFF is an important parameter on the outflow characteristics and performance of the SAC indoor unit. Three different rotational speeds were investigated for determining the differences of the flow structures, which are 950, 1100, and 1200 rpm and they are represented in the figures by FAN1, FAN2, and FAN3, respectively. These rotational speeds are the pre-defined levels for the investigated commercial SAC devices (Model 1). In addition, a skewed angle CFF (SK) and a straight CFF (ST) mounted on the same model (Model 1) for investigating the effect of the CFF type on the outflow characteristics at different rotational speeds.

The outflow of the SAC indoor unit was visualized as iso-surfaces at the velocity magnitudes (V) of 5.5,5, 4, 3, 2, and 1 m/s in Figures 3.24 – 3.29, respectively. Model 1 with a straight CFF has higher velocities at a wider area for all fan speeds. The discrete peak structures are apparent for the investigated region of the flow for the velocity magnitudes higher than 3 m/s at all fan speeds. In addition, fan speed does not affect the primary flow structures and it only changes the velocities inside the jet flow.

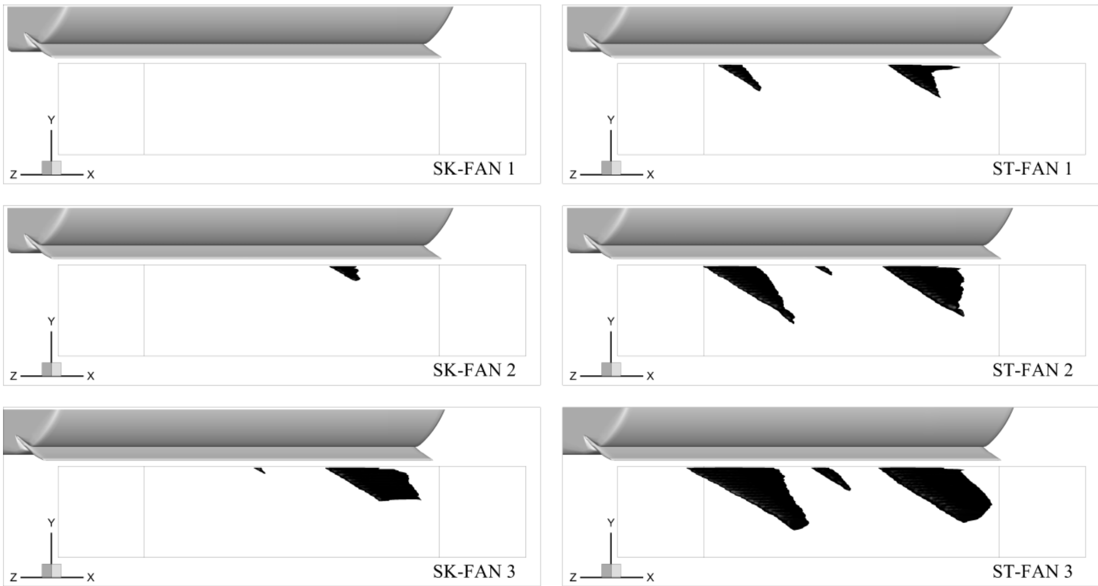

Figure 5.9 Visualization of the flow structures at the outlet section of the SAC indoor unit for different CFF rotational speeds, and for different CFF types; iso-surfaces at V= 5.5 m/s

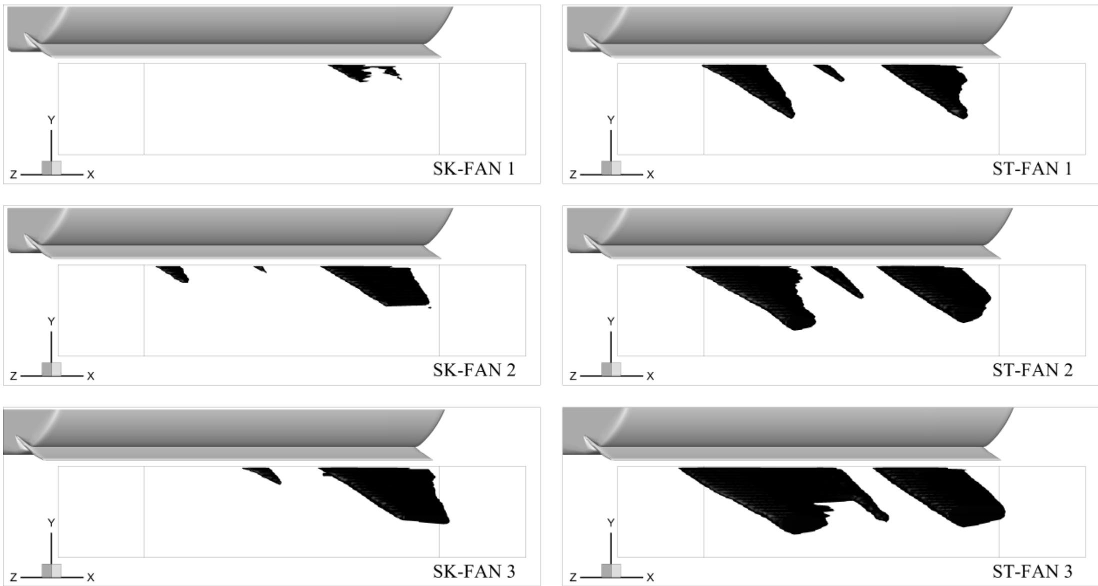

Figure 5.10 Visualization of the flow structures at the outlet section of the SAC indoor unit for different CFF rotational speeds, and for different CFF types; iso-surfaces at V= 5 m/s

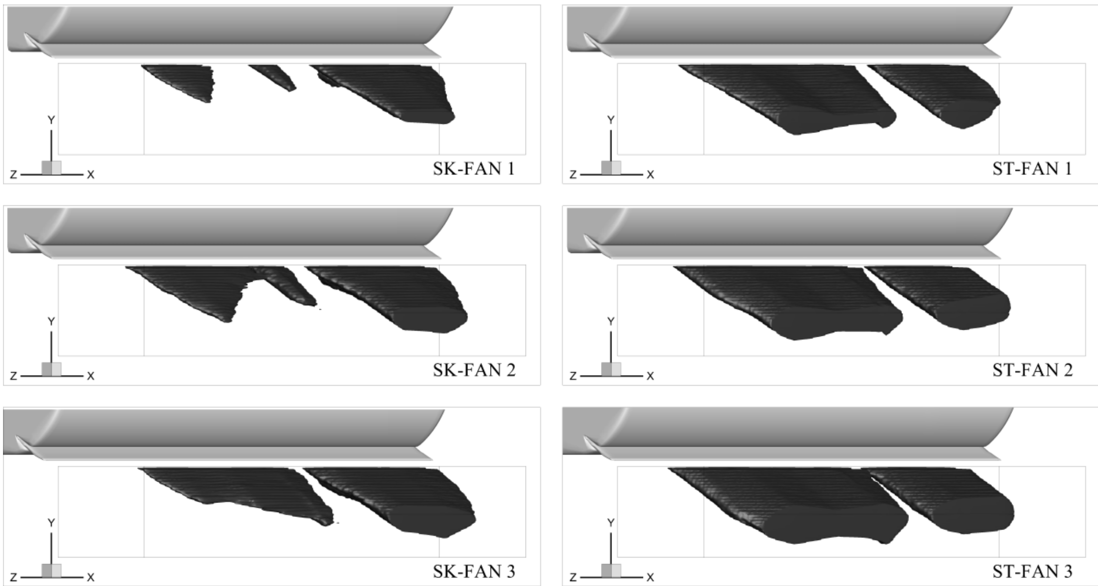

Figure 5.11 Visualization of the flow structures at the outlet section of the SAC indoor unit for different CFF rotational speeds, and for different CFF types; iso-surfaces at V= 4 m/s

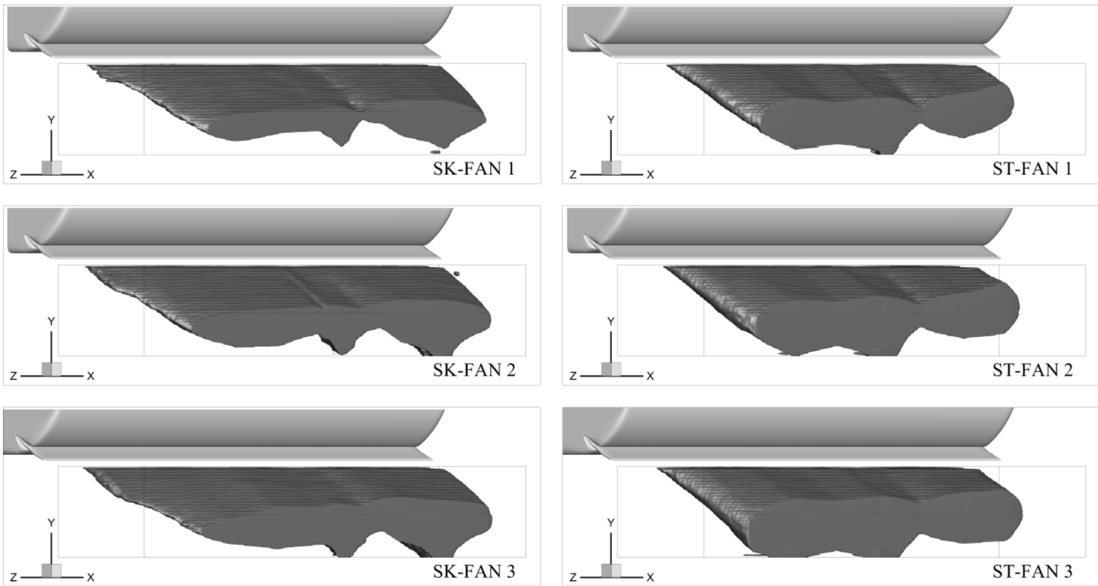

Figure 5.12 Visualization of the flow structures at the outlet section of the SAC indoor unit for different CFF rotational speeds, and for different CFF types; iso-surfaces at V= 3 m/s

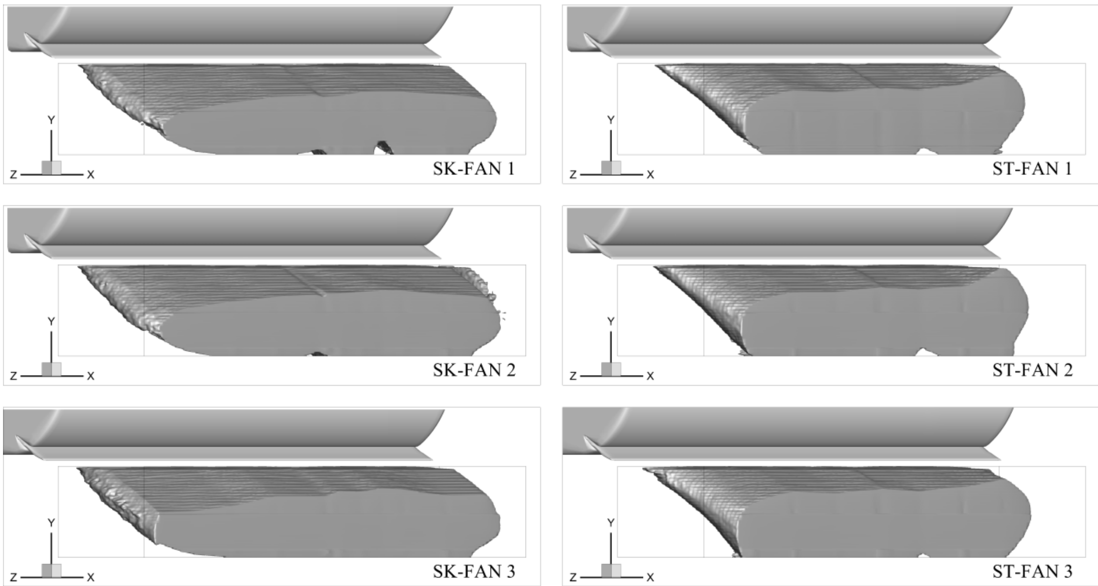

Figure 5.13 Visualization of the flow structures at the outlet section of the SAC indoor unit for different CFF rotational speeds, and for different CFF types; iso-surfaces at V= 2 m/s

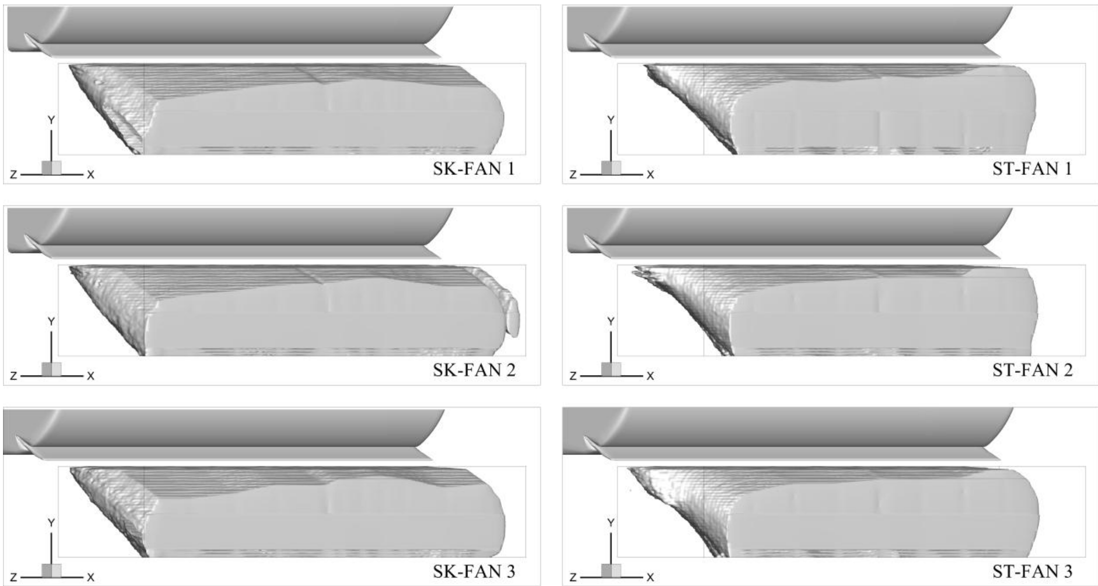

Figure 5.14 Visualization of the flow structures at the outlet section of the SAC indoor unit for different CFF rotational speeds, and for different CFF types; iso-surfaces at V= 1 m/s

CHAPTER SİX
TEMPERATURE MEASUREMENTS

6.1 Results of the Temperature Measurements at the Outlet of the Model 1

Temperature measurements were made at 12 different planes at the outlet of the Model 1 with a skewed CFF. The measurement planes are given in Figure 6.1. The measurement mesh was put inside the measurement planes and infrared images of the measurement mesh were taken. A total of 19 infrared images were captured at every measurement plane during 180 seconds. Therefore, the waiting time at every measurement plane was enough for the measurement mesh to reach the steady temperature distribution at that plane.

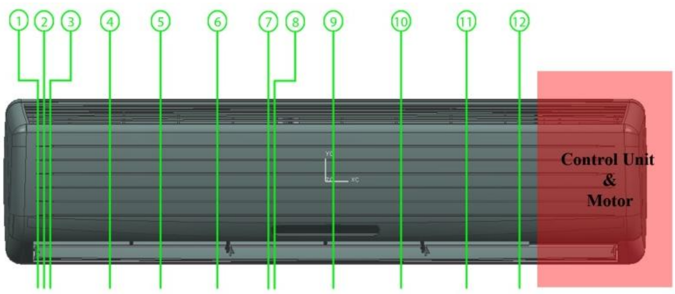

Figure 6.1 Temperature measurement planes

The SAC indoor unit was mounted on one of the walls of a room with the dimensions 4 m × 4 m × 4.5 m. Measurements were started 15 minutes after the SAC device had been turned on, and the temperature distribution inside the room was controlled during the measurements by 10 thermo-couples positioned at different points inside the room. The positions of the thermo-couples are given in Figure 6.2 and the change of temperature at different points inside the room is given in Figure 6.3.

As seen from Figure 6.3, the temperatures of the points suddenly increase in the first 10 minutes and the rate of increase of temperature decreases with the time. The increase of the temperatures at different points, after the measurements at the outlet of the SAC indoor unit started, is limited to 2 °C which is very low compared with the temperatures at the outflow of the device.

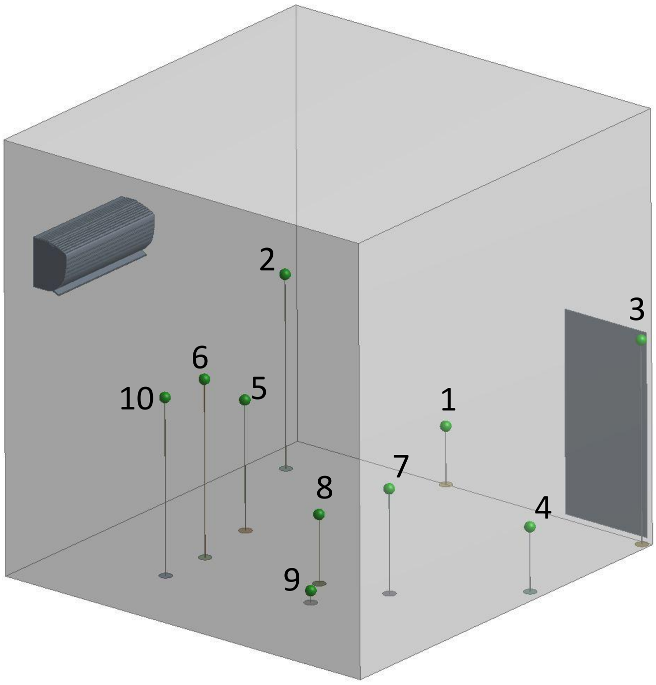

Figure 6.2 The positions of the thermo-couples inside the room during the temperature measurements

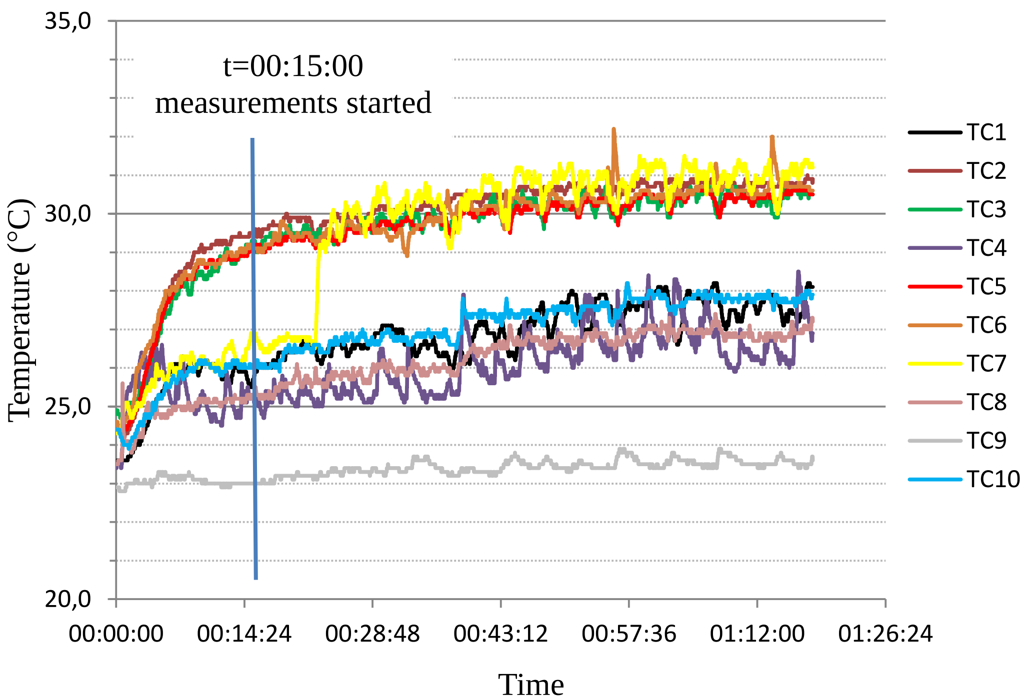

Figure 6.3 The change of temperature at different points inside the room

The results of the MIT measurements for the investigated planes are given in Figure 6.4. The high temperature region created by the high temperature planar jet flow can be seen at Plane 1. However, because of the low velocities and edge effects the temperatures are lower than the other planes at Plane 1. As the investigation area moves towards the left side, the temperatures at the core region increases, but the shape of it does not change at the edge planes (Planes 1-3). The core shape of the jet flow is thinner and the maximum temperature at the core increases up to 42 °C at Plane 4. The axis of the jet is shifted upwards at Plane 4 compared with the Planes 1-3 and this movement of the jet flow is also observed at Plane 5 and 6. This result is concordant with the velocity measurements. After Plane 6 the axis of the jet flow maintains the same until Plane 8. A very small shift occurs at Plane 9, but the core region remains inside the investigation area. Core temperatures rise up to 46 °C at Plane 6 and remain the same between Planes 6-12.

The 3D reconstruction of the temperature distribution at the investigated prismatic region also shows that the high temperature core of the jet flow is directed to the left side (Figure 6.5 a, b). The edge of this high temperature core cannot be seen at the left side of the device.

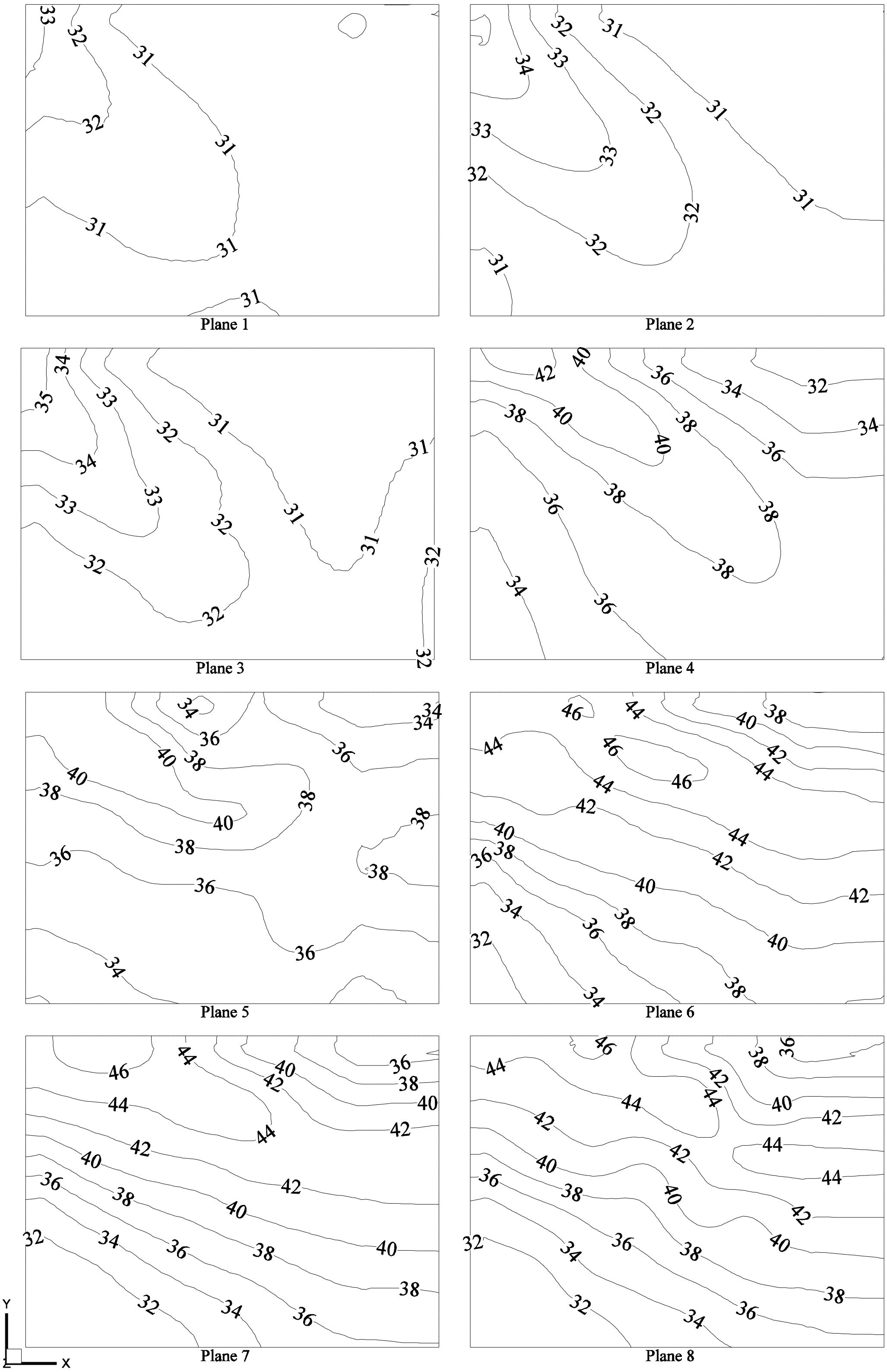

Figure 6.4 Temperature distributions for the planes on the different cross sections at the outlet of SAC indoor unit

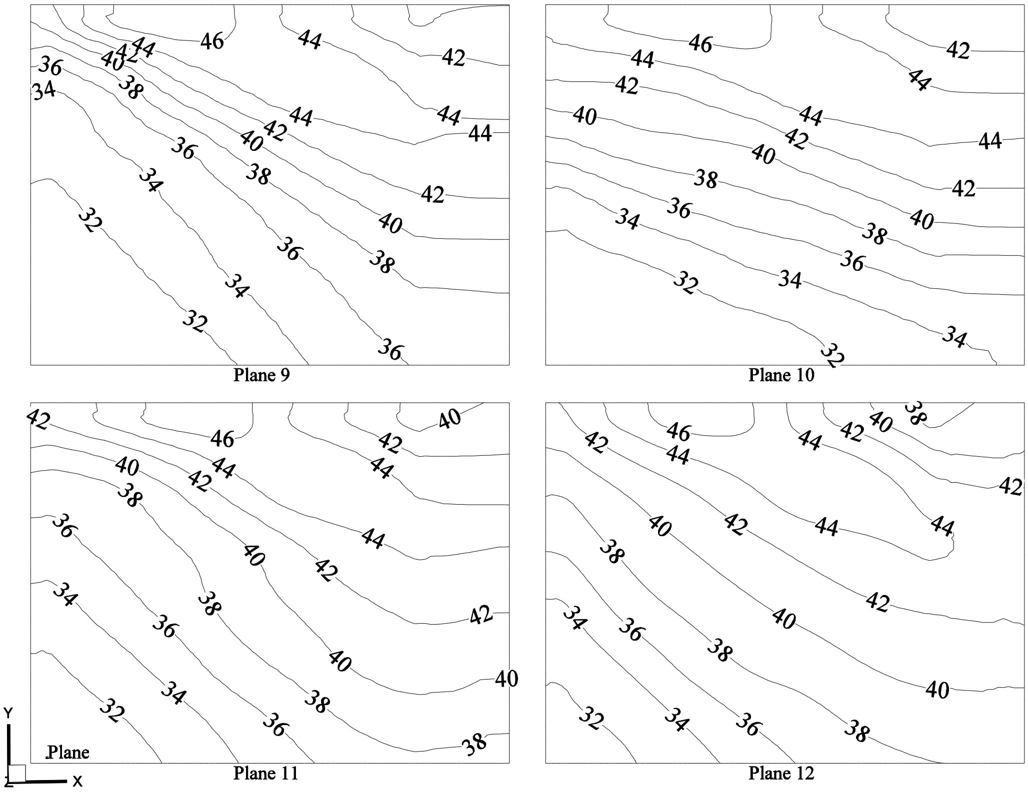

Figure 6.4 (continued) Temperature distributions for the planes on the different cross sections at the outlet of SAC indoor unit.

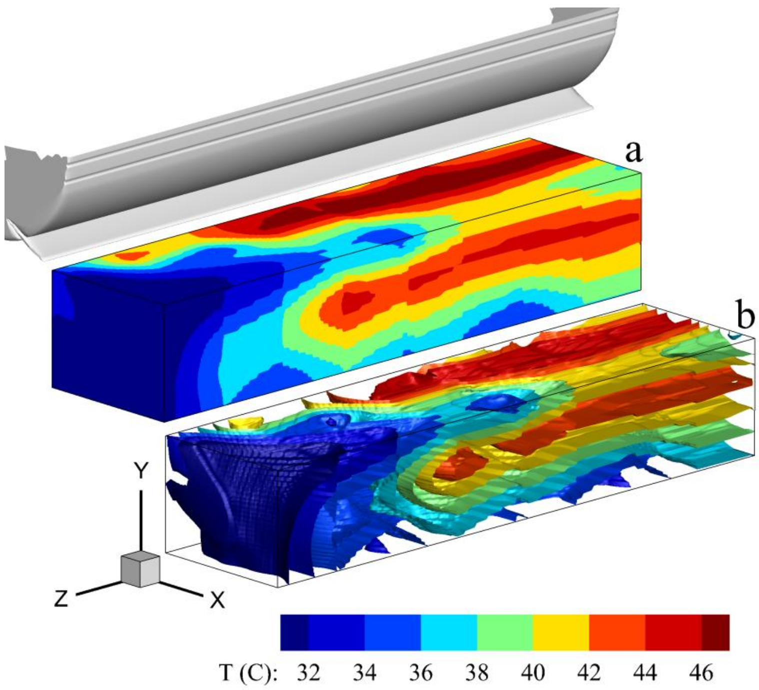

Figure 6.5 3D reconstruction of the temperature distribution at the outlet of the device: (a) contour plot, (b) iso-surfaces.

CHAPTER SEVEN
CONCLUSIONS

Design and optimization of the SAC indoor units have a great importance because of the demand for thermal and acoustic comfort, and reducing the energy consumption, as well as the strict standards and regulations ruled by the governments. Furthermore, producer companies need better designs together with the low cost for keeping or even improving their place in the market. Although simple and low cost solutions are needed for the design problems, the systems are so complex that very deep investigations are needed even for a small improvement of the devices because of the design point reached by today's technology.

Due to the lack of studies dealing with the outflow characterization of the SAC indoor units both for the temperature distribution and flow structure, in this thesis, velocity profile inside and outside a SAC indoor unit is visualized experimentally by Stereo Particle Image Velocimetry (SPIV) method. In addition, a novel method called Meshed Infrared Thermography (MIT) for determining and visualizing the temperature profile in an air flow field was introduced and used to investigate the temperature distribution at the outflow of the SAC indoor unit.

The MIT method is based on positioning an agent mesh inside a flow filed in which the temperature distribution is wanted to be known and imaging the infrared radiation emitted from the mesh. Different than the similar other infrared thermography techniques which are used for determining the temperature distribution inside gaseous flows, the disturbances on the flow and temperature distribution are minimized by using a discrete structure. For a certain extent, the temperature of the measurement point can be assumed as equal to the air temperature at that point. Therefore, the discrete temperature data can be combined to obtain the temperature distribution on a plane inside the flow. The success of the MIT method was investigated by using it for the determination of the temperature distribution inside a cylindrical jet. Thermocouples were positioned on the neighborhoods of ten measurement points and the consecutive measurements showed that the absolute difference between the averages of these instantaneous temperature values on individual points and the averages of the corresponding thermocouple data is between 0.24 and 2.73 °C. The average and the standard deviation of the absolute differences for all the points are 1.4 °C and 0.64 °C, respectively. The overall reliability of the MIT method was also verified by a linear regression analysis, which implies that there is an acceptable correlation between the MIT and thermocouple data (R^2=0.9481) and the MIT method is adequate for visualizing the temperature distribution at different flow sections.

The outflow characteristics of a SAC indoor unit is described by the examples of different models with a straight CFF, then the effect of the skewed CFF on the outflow characteristics was discussed on the same SAC indoor unit with a straight and a skewed CFF mounted on it, then the temperature distribution measurements were made for further investigation of the outflow of the device. Additionally the effect of the angular position of the directing airfoil at the outlet section of the SAC indoor unit, and the effect of the CFF rotational speed on the outflow characteristics was examined, and finally the inner flow of the device was visualized for the part between the rear wall and rear part of the FTHE, and the roof region (the region between the CFF and the FTHE).

The outflow and some parts of the inner flow of the SAC indoor unit were experimentally investigated for the first time in the literature, and the complex flow structures were visualized. The primary flow structure at the outflow of the device is a planar jet, and a transverse flow is shown under the planar jet which exists independently from the device type, CFF type, and CFF rotational speed; although the transverse flow’s behavior may change with these parameters. In addition, the effects of the device edges on the planar jet is shown, which should be further investigated for reducing the noise and vibration problems while increasing the flow rate. Furthermore, the core of the planar jet is divided into two parts again independently from the device type, CFF type, and CFF rotational speed. The two peak flow structure is thought to be result of the interaction between the transverse flows coming from the both sides of the device and the planar jet.

Temperature distribution inside the outflow of the SAC indoor unit, agrees well with the flow visualization studies. Because of the low velocities and edge effects the temperatures are lower than the other planes at the right side. As the investigation area moves towards the left side, the temperatures at the core region increases up to 46 °C, the core shape of the jet flow gets thinner, and the axis of the jet is shifted upwards. This result is concordant with the velocity measurements. However, more information can be got by using a bigger measurement mesh and investigating a larger area at the outflow of the SAC indoor unit.

As a design improvement case study, the effect of the angular position of the directing airfoil on the outflow characteristics was investigated. Results of this study show that flow is directed by the airfoil and a circulating region is observed above the airfoil for different angular positions. Flow at the investigated section of the device includes a part of the eccentric vortex, which is the most important structure of a CFF flow, although a deeper investigation is needed for revealing this effect. The angular position of the airfoil affects the form and characteristics of the jet flow at the outlet section both on the shape and the velocity.

Critical angular position of the directing airfoil is between 30°-45° for which a transition from a smooth flow to a vortex above the airfoil occurs. For β=45° and 60°, the vortex above the airfoil behaves like a seal against the flow and forces the air to pass below the airfoil. Depending on the airfoil geometry, the distances between the leading edge of the airfoil, CFF and vortex wall may be the important parameters to control the flow.

It is known from the literature that the designs of the casing of the CFF, and the CFF parameters (the number of the blades, blade shape, fan diameter, the distances between the CFF and the rear wall and the vortex wall etc.) are important for a steady outflow and high performance operation. This research showed that, Model 2 and Model 3 which have better design than Model 1 also have a better outflow. However, the parameters that directly affect the outflow characteristics are not discussed in this thesis. It should be further investigated in special experimental setups by changing the CFF parameters systematically.

The CFF alone has a complex flow structure and its interaction with the surrounding device parts makes the flow of the SAC indoor unit more complex. Although some flow structures and temperature distribution is visualized in this thesis, deeper investigations are needed for totally understanding the interaction between the device parameters and the flow conditions of the SAC indoor units.

REFERENCES

Anderson, R., Hassani, V., & Kirkpatrick, A. (1991). Visualizing the air flow from cold air ceiling jets. *ASHRAE Journal, 33*, 30-35.

Astarita, T., Cardone, G., & Carlomagno, G. M. (2006). Infrared thermography: An optical method in heat transfer and fluid flow visualisation. *Optics and Lasers in Engineering, 44*, 261-281.

Astarita, T., Cardone, G., Carlomagno, G. M., & Meola, C. (2000). A survey on infrared thermography for convective heat transfer measurements. *Optics & Laser Technology, 32*, 593-610.

Burch, S. D., Hassani, V., & Penney, T. R. (1992). *Use of infrared thermography for automotive climate control analysis.* Warrendale: National Renewable Energy Laboratory.

Casarsa, L., & Giannattasio, P. (2011). Experimental study of the three-dimensional flow field in cross-flow fans. *Experimental Thermal and Fluid Science, 35*, 948-959.

Cehlin, M., Moshfegh, B., & Sandberg, M. (2002). Measurements of air temperatures close to a low-velocity diffuser in displacement ventilation using an infrared camera. *Energy and Building, 34*, 687-698.

Chen, A., Li, S., & Huang, D. (2008). Numerical analysis of aerodynamic noise radiated from cross flow fan. *Front. Energy Power Eng. China, 2*(4), 443-447.

Cho, Y., & Moon, Y. J. (2003). Discrete noise prediction of variable pitch cross-flow fans by unsteady navier stokes predictions. *Journal of Fluids Engineering, 125*, 534-550.

Dabiri, D. (2009). Digital particle image thermometry/velocimetry: a review. *Experiments in Fluids, 46*, 191-241.

Dang, T. Q., & Bushnell, P. R. (2009). Aerodynamics of cross-flow fans and their application to aircraft propulsion and flow control. *Progress in Aerospace Sciences, 45*, 1-29.

Eck, B. (1973). *Design and operation of centrifugal, axial flow and cross flow fans.* Oxford: Pergamon Press.

Elvsén, P., & Sandberg, M. (2009). Buoyant jet in a ventilated room: Velocity field, temperature field andair flow patterns analysed with three different whole-field methods. *Building and Environment, 44*, 137-145.

Funaki, J., Kimata, N., Hisada, M., & Hirata, K. (2006). Aspect-ratio and Reynolds-Number effects on short-span cross-flow impellers without casings. *JSME International Journal Series B, 49*(4), 1196-1205.

Gabi, M., & Klemm, T. (2004). Numerical and experimental investigations of cross-flow fans. *Journal of Computational and Applied Mechanics, 5*(2), 251-261.

Gallo, M., Kunsch, J. P., & Rösgen, T. (2010). A novel infrared thermography (IRT) based experimental technique for distributed temperature measurements in hot gas flows. *10th International Conference on Quantitative Infrared Thermography.* Quebec (Canada).

Gan, J., Liu, F., Liu, M., & Wu, K. (2008). The unsteady fluctiating pressure and velocity in a cross flow fan. *Journal of Thermal Science, 17*(4), 349-355.

Gebrehiwot, M. G., Baerdemaeker, J. D., & Baelmans, M. (2010). Numerical and experimental study of a cross-flow fan for combine cleaning shoes. *Biosystems Engineering*, *106*, 448-457.

Govardhan, M., & Sampat, D. L. (2005). Computational studies of flow through cross flow fans - effect of blade geometry. *Journal of Thermal Science, 14*(3), 220-229.

Govardhan, M., & Venkateswarlu , G. (2003). Effect of impeller geometry and tongue shape on the flow field of cross flow fans. *Journal of Thermal Science, 12*(2), 118-125.

Hirata, K., Iida, Y., Takushima, A., & Funaki, J. (2008). Instantaneous pressure measurement on a rotating blade of a cross-flow impeller. *Jornal of Environment and Engineering, 3*(2), 261-271.

Incropera , F. P., & DeWitt, D. P. (1996). *Fundamentals of heat and mass transfer* (Fourth Edition b.). New York: John Wiley & Sons.

Kim, J. W., & Oh, H. W. (2004). Mean stream line analysis for performance prediction of cross-flow fans. *KSME International Journal*, *18*(8), 1428-1434.

Kim, T. A., Kim, D. W., Park, S. K., & Kim, Y. J. (2008). Performance of a cross-flow fan with various shapes of a rearguiderand an exit duct. *Journal of Mechanical Sicence and Technology, 22*, 1876-1882.

Lazzaretto, A. (2003). A criterion to define cross-flow fan design parameters. *Journal of Fluids Engineering, 125*, 680-683.

Lazzaretto, A., Toffolo, A., & Martegani, A. D. (2003). A systematic experimental approach to cross-flow fan design. *Journal of Fluids Engineering, 125*, 684-693.

Lazzarotto, L., Lazzaretto, A., Martegani, A. D., & Macor, A. (2001). On cross-flow fan similarity: Effects of casing shape. *ASME Journal of Fluids Engineering, 123*, 523-531.

Lee, S. H., Na, S. U., Kang, G., & Ko, H. S. (2011). Study on flow distribution for room air consitioner using visualization technique. *Journal of Visualization, 14*, 193-200.

Meola, C., & Carlomagno, G. M. (2004). Recent advances in the use of infrared thermography. *Measurement Science and Technology, 15*, 27-58.

Moon, Y. J., Cho, Y., & Nam, H. (2003). Computation of unsteady viscous flow and aeroacoustic noise of cross flow fans. *Computers & Fluids, 32,* 995-1015.

Murata, S., & Nishihara , K. (1976b). An experimental study of cross flow fan (2nd report, movement of eccentric vortex inside impeller). *Bulletin of the JSME, 19*(129), 322-329.

Murata, S., & Nishihara, K. (1976a). An experimental study of cross flow fan (1st report, effects of housing geometry on the fan performance). *Bulletin of the JSME, 19*(129), 314-321.

Murata, S., Ogawa, T., Shimizu, I., Nishihara, K., & Kinoshita, K. (1978). A study of cross flow fan with inner guide aparatus. *Bulletin of the JSME, 21*(154), 681-688.

Narayanan, V., Page, R. H., & Seyed-Yagoobi, J. (2003). Visualization of air flow using infrared thermography. *Experiments in Fluids, 34*, 275-284.

Neely, A. J. (2008). Mapping temperature distributions in flows using radiating high-porosity meshes. *Experiments in Fluids*, *45*, 423-433.

Neto, L. P., Gamerio Silva, M. C., & Costa, J. J. (2006). On the use of infrared thermography in studies with air curtain devices. *Energy and Buildings*, *38*, 1194-1199.

Noël, J. Y., Farall, M., & Casarsa, L. (2007). Aero-acoustics in a tangential blower: Validation of the CFD flow distribution using advanced PIV techniques. *International Journal of Multiphysics, 1*(4), 377-392.

Seo, H. S., Kim, J. B., & Kim, Y. J. (2009). The effect of blade angle on the flow and pressure distributions in the vicinity of the diffuser blades of a room air conditioner. *Journal of Mechanical Sicence and Technology, 23*, 1840-1845.

Shih, Y. C., Hou, H. C., & Chiang, H. (2008). On similitude of the cross flow fan in a split type air conditioner. *Applied Thermal Engineering, 28*, 1853-1864.

Tanaka, S., & Murata, S. (1994). Scale effects in cross-flow fans (Effects of fan dimensions on performance curves). *JSME International Journal Series B, 37*(4), 844-852.

Tanaka, S., & Murata, S. (1995). Scale effects in cross-flow fans (Effects of fan dimensions on flow details and the universal representation of performance). *JSME International Journal Series B, 38*(3), 388-396.

Toffolo, A. (2004). On cros-flow fan theoretical performance and efficiency curves: An energy loss analysis on experimental data. *Journal of Fluids Engineering*, *126*, 743-751.

Toffolo, A. (2005). On the theoretical link between design parameters and performance in cross-flow fans: a numerical and experimental study. *Computers & Fluids, 34*, 49-66.

Toffolo, A., Lazaretto, A., & Martegani, A. D. (2004). An experimental investigation of the flow field pattern within the impeller of a cross-flow fan. *Experimental Thermal and Fluid Science, 29*, 53-64.

Tsai, G. L., Tu, T. H., Li, T. C., & Wang, K. H. (2006). Flow style investigation and noise reduction of a cross-flow fan with varied rotor-skew-angle rotor. *JSME International Journal Series B, 49*(3), 695-704.

Tsurusaki, H., Shimizu, H., Tsujimoto, Y., Yoshida, Y., & Kitagawa, K. (1996). Study of cross-flow-fan internal flow by flow visualization. *JSME International Journal Series B, 39*(3), 540-545.

Tsurusaki, H., Tsujimoto, Y., Yoshida, Y., & Kitagawa, K. (1997). Visualization measurement and numerical analysis of internal flow in cross-flow fan. *Journal of Fluids Engineering, 119*, 633-638.

Uskaner, Y. A., & Göksel, Ö. T. (1999a). Effects of rear casing on cross flow fan performance. *Proceedings of MMO Denizli Division Science Meeting (in Turkish)* (pp. 44-50). Denizli: MMO.

Uskaner, Y. A., & Göksel, Ö. T. (1999b). Effects of rotor parameters on cross flow fan performance. *IV. Proceedings of National HVAC and Sanitary Convention and Exhibition (in Turkish). 2*, pp. 579-597. İzmir: MMO.

Xue, Y., Gan, J., Wang, J., & Wu, K. (2010). Internal flow numerical simulation of a cross-flow fan in refrigerant operating condition using user-defined functions. *International Journal for Numerical Methods in Fluids, 65*, 1039-1049.

Yamafuji, K. (1975a). Studies on the flow of cross-flow impellers (1st report, experimental study). *Bulletin of the JSME, 18*(123), 1018-1025.

Yamfuji, K. (1975b). Studies on the cross-flow impellers (2nd report, analytical study). *Bulletin of the JSME, 18*(126), 1425-1431.